Design of the LED Driver for the Precision Optical CAlibration Module

Master Thesis

Antonio Becerra Esteban

Technische Universität München

Physics Department

Chair for Experimental Physics with Cosmic Particles

December 4, 2017

Supervisor: Prof. Dr. Elisa Resconi

Abstract

A study of the circuit designed by J.S.Kapustinsky et Al. in 1985 as a cheap fast flasher for the Precision Optical CAlibration Module (POCAM) is carried out. Its characteristics make it a perfect candidate as short light pulses generator in order to simulate neutrino double-bang-like events in the framework of the next IceCube upgrade, IceCube-Gen2. The response of diverse LEDs with different features was studied by varying the available charge, the bias voltage and the inductance of the Kapustinsky circuit. The pulses were measured with a PIN-Diode and a SiPM. The amplification of the signal was accomplished by a couple of charge sensitive preamplifiers and afterwards monitored and stored in the oscilloscope for further analysis. To produce an isotropic pulse, the LED flashed inside a PFTE sphere that spread the light in 4π. All the tests were carried out inside a dark metallic box with foam cladding to ensure the isolation from external photon sources. For a first test at the Gigaton Volume Detector (GVD) at Lake Baikal four different Kapustinky-like circuits were set up. This configuration allows the POCAM to produce four different light pulses: two long pulses $(15 - 25\,ns)$ and two short pulses $(5 - 10\,ns)$ in green $(525 - 527\,nm)$ and blue $(455 - 470\,nm)$. The final driver board includes the PIN-Diode and the SiPM as well as the preamplifiers that sends the information to an FPGA for its storage. This information can be retrieved remotely for its further analysis. The total amount of photons produced, assuming isotropy, varied from $\mathcal{O}(10^8)$ to $\mathcal{O}(10^9)$ photons per single flash.

Contents

Introduction

The IceCube is a 1 km^3 neutrino observatory located in the south pole. It is composed by 5160 spherical optical sensors supplied with a photomultiplier tube and data acquisition equipment. Also known as Digital Optical Modules (DOMs), these spheres are deployed in the ice across 86 strings with a depth of $1km$ from $1450m$ to $2450m$. The interaction of neutrinos with the nuclei in the ice produce particles that emit photons which are registered by the Digital Optical Modules.

The next step of the detection and reconstruction of the energy and direction of the neutrinos will be performed by the IceCube-Gen2 extension. It is designed to reduce the energy threshold of the detectors and it will detect atmospheric neutrinos with high statistics, allowing the study of the neutrino oscillation and the neutrino mass hierarchy. To accomplish this goal, a verification of the ice properties and the light response of the DOMs has to be carried out with a higher precision than it was done previously. Here is where the Precision Optical CAlibration Module (POCAM) comes into play. A self calibrating device that simulates shower-like events by producing short isotropic light pulses. The device can emit light pulses of around 5 - 20 ns with a total output of $\mathcal{O}(10^8) - \mathcal{O}(10^9)\gamma$ per pulse covering a total surface of 4π sr in different wavelengths. The goal of the POCAM is to reduce the current systematic uncertainty of IceCube from 10% to a level of a few %.

The POCAM is a pill-shaped device with a titanium housing and a glass hemisphere on each end. Inside, on each end, a multiwavelength set of LEDs in combination with a diffusing polytetrafluoroethylene (PTFE) sphere provides a very homogeneous light emission profile (See Fig.1).

The pulses are produced thanks to a circuit designed by J.S.Kapustinsky in 1985. The PTFE sphere spreads the light over 4π illuminating the whole hemisphere. The pulse is then registered *in-situ* by high precision photosensors: a 33 mm^2 PIN-Diode (PS33-6b-TO) from First Sensor and a 9 mm^2 SiPM (PM3325-EB) from KETEK.

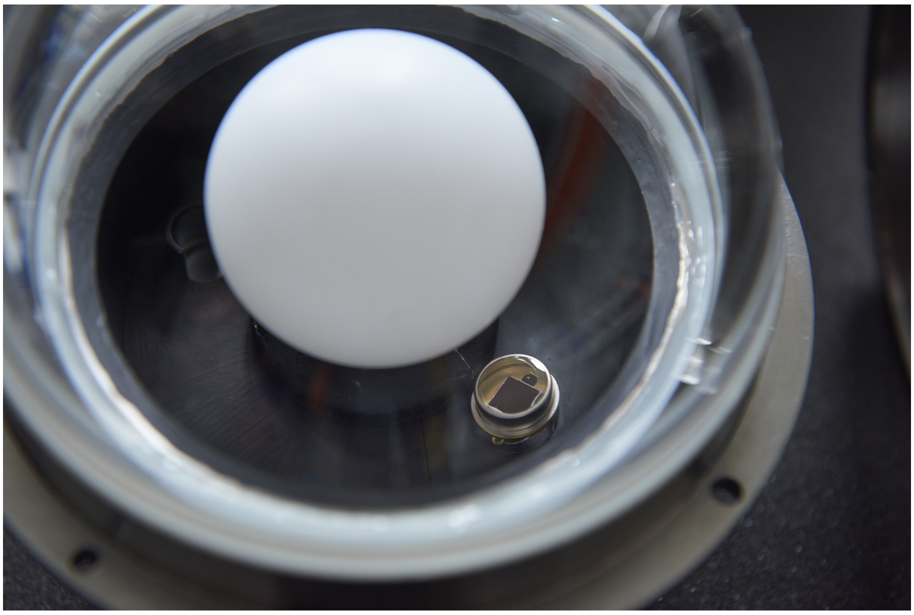

Figure 1: *Outside view of one end of the POCAM: to see is its external glass hemisphere (attached to the housing with a special glue), the light-spreading PTFE sphere and the PIN diode.*

The light emitted by the POCAM can be detected by the optical modules of IceCube-Gen2 resulting not only in a verification of the energy scale and the energy resolution but also in a study of the optical impact of refrozen drill holes on DOM sensitivity, the relative detection efficiency of each individual DOM and the anisotropic scattering strength of the bulk ice.

Chapter 1

Neutrino history and physics

1.1 Brief history of the neutrino

From Italian, *little neutron*, it is a fermionic particle that only interacts via weak force and gravity. Wolfgang Pauli postulated it in 1930, calling it neutron, to account for the energy, momentum and spin lacking from the process of beta decay. The neutrino has no charge and a very small mass, so small that at the beginning it was supposed to be zero. In 1932, James Chadwick discovered a particle with a higher mass and also called it neutron. At this point the particle involved in the conservation of energy in beta decay and the nuclear particle were consider to be the same one.
The term *neutrino* was introduced by Edoardo Amaldi to distinguish both particles. Enrico Fermi made it popular after using it at a conference in Paris in 1932 and at the Solvay Conference of 1933. According to its theory of beta decay [1], the neutron can decay to a proton, an electron and a small particle with no charge (electron antineutrino):

$$n^0 \rightarrow p^+ + e^- + \bar{v}_e \tag{1.1}$$

Its experimental detection is attribbuted to the components of the Cowan-Reines neutrino experiment [2]. According to the paper published in 1956, they used a nuclear reactor to create antineutrinos via beta decay, these reacted with protons yielding neutrons and positrons.

$$p^+ + \bar{v}_e \rightarrow n^0 + e^+ \tag{1.2}$$

This result was awarded forty years later, in 1995, with the Nobel Prize.

1.2 Neutrino flavour

Flavour makes reference to the different species of particles of the Standard Model. It is composed by three families of fermions plus five bosons that act as force carriers of the elementary interactions and the Higgs field. Each family consists of 2 leptons and 2 quarks. That makes a total of 6 quark flavours and 6 lepton flavours, as it can be seen in the following chart.

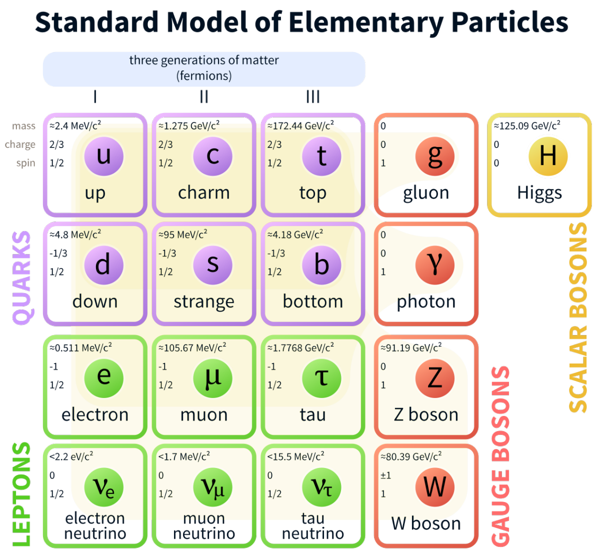

Figure 1.1: *Standard Model Elementary particles chart*[3].

In each family, one lepton is able to interact through gravity, the electromagnetic and the weak interaction (e, μ, τ) and the other carry no electromagnetic or color charge so it only responds to weak interaction and gravity. These correspond to three kinds of neutrinos. One per leptonic flavour:

$$v_e \rightarrow electron\ neutrino$$

$$v_\mu \rightarrow muon\ neutrino$$

$$v_\tau \rightarrow tau\ neutrino$$

The first electron antineutrino was discovered, as already mentioned, in 1956. Later, in 1962, Lederman, Schwartz and Steinberg detected the first muon neutrino[4]. Pions and Kaons generated by bombarding a *Be* target with protons, decay to a muon and a muon-anti-neutrino

$$\pi^- \rightarrow \mu^- + \bar{\nu_\mu} \tag{1.3}$$

To explain the CP-Violation, a 3rd family of leptons was postulated. In the 70's, the τ was discovered and so its neutrino companion was also expected to be found.

$$\tau^- \to \pi^- + \bar{\nu_\tau} \tag{1.4}$$

Finally, in 2000, the tau-neutrino was detected at the Fermilab by DONUT collaboration.

1.3 Neutrino interactions

Neutrinos can tipically go through matter without suffering any alteration or being detected. This happens because neutrinos, as leptons, don't take part in the strong interaction, the weak force is a short range interaction and gravity is so weak that can be neglected on the subatomic scale.
We focus on the weak interaction which happens via neutral current (NC) or charged current (CC). The reason why the weak force is considered of short range is that the intermediate particles of this processes, the Z^0 and the $W^\pm$ bosons, are particularly heavy ($m_{Z^0} = 91.1876(21)\,GeV/c^2$, $m_{W^\pm} = 80.385(15)\,GeV/c^2$)[5]. The W^+ and W^- have a charge of $\pm 1, e$ respectively and the Z^0 is electrically neutral. $W^\pm$ bosons are their antiparticle reciprocally and the Z^0 is its own antiparticle. While $W\pm$ possesses magnetic moment, the Z doesn't.
Both, W^+ and W^- bosons mediate in the process of neutrino absorption. Due to its own charge, they induce the emission or absorption of e^- or e^+ in nuclei. This causes the conversion of one chemical element into an isotope or into another element. The Z boson is responsible for the transfer of energy, momentum and spin during the elastic scattering of neutrinos with matter. See Fig.1.2.

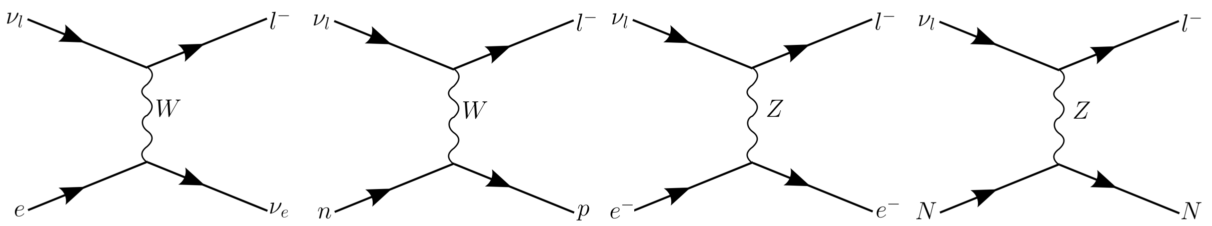

Figure 1.2: *Diagrams of CC (W as mediator) and NC (Z as mediator) interaction between atomic electrons or nucleons within the nucleus.*

CC interactions happen with left handed neutrinos or right handed antineutrinos. Interacting right handed neutrinos have never been observed[6]. As every massive particle can have both chiralities but massless particles can't, neutrinos were assumed massless and moving at c[7]. Anyway, there are evidences of neutrino mixing[8] so they must have mass.

1.4 Neutrino oscillations in vacuum

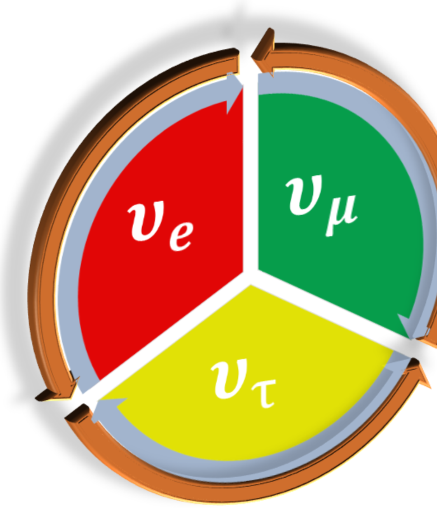

Figure 1.3: *Scheme of the neutrino oscillation between the three generations.*

Neutrinos created with a lepton flavour can undergo a change and be measured later with a different flavour. That's the quantum mechanical phenomenon known as *neutrino oscillation* (represented in Fig.1.3).

The three neutrino flavour states ν_e, ν_μ, ν_τ that interact via CC are a superposition of three neutrino states with a well definite mass. This can be expressed as

$$\begin{pmatrix} \nu_e \\ \nu_\mu \\ \nu_\tau \end{pmatrix} = \begin{pmatrix} U_{e1} & U_{e2} & U_{e3} \\ U_{\mu 1} & U_{\mu 2} & U_{\mu 3} \\ U_{\tau 1} & U_{\tau 2} & U_{\tau 3} \end{pmatrix} \begin{pmatrix} \nu_1 \\ \nu_2 \\ \nu_3 \end{pmatrix} \tag{1.5}$$

or written in a more compact way with with $l = (e, \mu, \tau)$ and $\alpha = (1, 2, 3)$:

$$|\nu_l\rangle = \sum_\alpha U_{l\alpha} |\nu_\alpha\rangle \tag{1.6}$$

The 3×3 unitary matrix U is the Pontecorvo-Maki-Nakagawa-Sakata matrix or PMNS. One can also write the mass states as a l.c. of the flavour states inverting the previous expression:

$$|\nu_\alpha\rangle = \sum_l U^*_{l\alpha} |\nu_l\rangle \tag{1.7}$$

The Schrödinger equation for the neutrino mass states can be written as:

$$i\frac{\partial}{\partial t}\left|\nu_\alpha(t)\right\rangle = H\left|\nu_\alpha(t)\right\rangle. \tag{1.8}$$

With the neutrino mass eigenstates $|\nu_\alpha\rangle$ being the eigenstates of the Hamiltonian.

$$H\left|\nu_\alpha\right\rangle = E_\alpha\left|\nu_\alpha\right\rangle \tag{1.9}$$

and the eigenenergies being

$$E_\alpha = \sqrt{\vec{p}^2 + m_\alpha^2} \tag{1.10}$$

As a consequence, neutrino mass state propagate as plane waves in the base of mass eigenstates.

$$\left|\nu_\alpha(t)\right\rangle = e^{-iE_\alpha t}\left|\nu_\alpha\right\rangle \tag{1.11}$$

Using 1.6 and 1.11 we can write down the time evolution of the flavour states as a superposition of the flavour states:

$$\left|\nu_l(t)\right\rangle = \sum_p\left(\alpha\sum_\alpha U_{l\alpha}^* e^{-iE_\alpha t}U_{p\alpha}\right)\left|\nu_p\right\rangle \tag{1.12}$$

The probability of transition between two flavour states depending on the time is the square of the coefficient of $|\nu_p\rangle$

$$P_{\nu_l\to\nu_p}(t) = \left|A_{\nu_l\to\nu_p}(t)\right|^2 = \sum_{\alpha,\beta} U_{l\alpha}^* U_{p\alpha} U_{l\beta} U_{p\beta}^* e^{-i(E_\alpha - E_\beta)t} \tag{1.13}$$

Let's consider a state at $t = 0$

$$\left|\Psi(t=0)\right\rangle = \left|\nu_\mu\right\rangle = U_{\mu 1}\left|\nu_1\right\rangle + U_{\mu 2}\left|\nu_2\right\rangle + U_{\mu 3}\left|\nu_3\right\rangle \tag{1.14}$$

taking the $z - axis$ as the propagation direction we can write the evolution of the wave function as:

$$\left|\Psi(t)\right\rangle = \left|\nu_\mu\right\rangle e^{-ip_1 x} = U_{\mu 1}\left|\nu_1\right\rangle + U_{\mu 2}\left|\nu_2\right\rangle e^{-ip_2 x} + U_{\mu 3}\left|\nu_3\right\rangle e^{-ip_3 x} \tag{1.15}$$

after propagating through a distance D, writing $\phi_i = p_i x = E_i t - |\vec{p}|\, D = E_i - \vec{p_i} D$ we obtain

$$\left|\Psi(D)\right\rangle = U_{\mu 1}\left|\nu_1\right\rangle e^{-i\phi_1} + U_{\mu 2}\left|\nu_2\right\rangle e^{-i\phi_2} + U_{\mu 3}\left|\nu_3\right\rangle e^{-i\phi_3} \tag{1.16}$$

where ϕ_i is the phase of the mass eigenstate i at $z = D$ can be approximated as $\phi_i \approx \frac{m_i^2}{2E_i}D$. Using Eq. 1.7 we write the mass eigenstates in terms of the flavour eigenstates:

$$\begin{aligned}\left|\Psi(D)\right\rangle =& U_{\mu_1}\left(U_{e_1}^*\left|\nu_e\right\rangle + U_{\mu_1}^*\left|\nu_\mu\right\rangle + U_{\tau_1}^*\left|\nu_\tau\right\rangle\right)e^{-i\phi_1} \\ &+ U_{\mu_2}\left(U_{e_2}^*\left|\nu_e\right\rangle + U_{\mu_2}^*\left|\nu_\mu\right\rangle + U_{\tau_2}^*\left|\nu_\tau\right\rangle\right)e^{-i\phi_2} \\ &+ U_{\mu_3}\left(U_{e_3}^*\left|\nu_e\right\rangle + U_{\mu_3}^*\left|\nu_\mu\right\rangle + U_{\tau_3}^*\left|\nu_\tau\right\rangle\right)e^{-i\phi_3}\end{aligned} \tag{1.17}$$

The terms can be rearranged in order to write together the coefficients that go with $|\nu_e\rangle$,$|\nu_\mu\rangle$ and $|\nu_\tau\rangle$

$$\begin{aligned}|\Psi(D)\rangle &= \left(U_{\mu 1}U^*_{e_1}e^{-i\phi_1} + U_{\mu_2}U^*_{e_2}e^{-i\phi_2} + U_{\mu_3}U^*_{e_3}e^{-i\phi_3}\right)|\nu_e\rangle \\ &+ \left(U_{\mu_1}U^*_{\mu_1}e^{-i\phi_1} + U_{\mu_2}U^*_{\mu_2}e^{-i\phi_2} + U_{\mu_3}U^*_{\mu_3}e^{-i\phi_3}\right)|\nu_\mu\rangle \\ &+ \left(U_{\mu_1}U^*_{\tau_1}e^{-i\phi_1} + U_{\mu_2}U^*_{\tau_2}e^{-i\phi_2} + U_{\mu_3}U^*_{\tau_3}e^{-i\phi_3}\right)|\nu_\tau\rangle\end{aligned} \tag{1.18}$$

So, taking into account the previous expression and Eq. 1.13 the probability of transition from one flavour to another in the case of $(\nu_\mu \to \nu_e)$ is :

$$\begin{aligned}P\left(\nu_\mu \to \nu_e\right) &= \left|\langle\nu_e|\Psi(D)\rangle\right|^2 \\ &= \left|U_{\mu 1}U^*_{e_1}e^{-i\phi_1} + U_{\mu_2}U^*_{e_2}e^{-i\phi_2} + U_{\mu_3}U^*_{e_3}e^{-i\phi_3}\right|^2\end{aligned} \tag{1.19}$$

Expanding 1.19 we can relate it with 1.13. Approximating the phase difference $E_m - E_i \approx \frac{\Delta m^2_{mi}}{2E}$ and defining the mass squared difference as $\Delta m^2_{mi} \equiv m^2_m - m^2_i \ll E^2$. This example shows that by meassuring D and E, the theory of neutrino oscillations can be proved[9].

1.4.1 The PMNS Matrix for the three flavours case

Three rotation (mixing) angles $\theta_{12}, \theta_{23}, \theta_{13}$, and a complex phase δ related with the CP-Violation are normally used to write the PMNS matrix.

$$\begin{aligned}\begin{pmatrix} U_{e1} & U_{e2} & U_{e3} \\ U_{\mu 1} & U_{\mu 2} & U_{\mu 3} \\ U_{\tau 1} & U_{\tau 2} & U_{\tau 3}\end{pmatrix} &= \begin{pmatrix} 1 & 0 & 0 \\ 0 & c_{23} & s_{23} \\ 0 & -s_{23} & c_{23}\end{pmatrix} \times \\ &\times \begin{pmatrix} c_{13} & 0 & s_{13}e^{-i\delta} \\ 0 & 1 & 0 \\ -s_{13}e^{-i\delta} & 0 & c_{13}\end{pmatrix} \times \begin{pmatrix} c_{12} & s_{12} & 0 \\ -s_{12} & c_{12} & 0 \\ 0 & 0 & 1\end{pmatrix}\end{aligned} \tag{1.20}$$

where $s_{ij} = sin\theta_{ij}$ and $c_{ij} = cos\theta_{ij}$. The first of the three matrices is the one dominating the processes that affect the atmospheric neutrinos and the third dominates the solar ones. The full unitary matrix U can be written as:

$$U = \begin{pmatrix} c_{12}c_{13} & s_{12}c_{13} & s_{13}e^{-i\delta} \\ -s_{12}c_{23} - c_{12}s_{23}s_{13}e^{-i\delta} & c_{12}c_{23} - s_{12}s_{23}s_{13}e^{-i\delta} & s_{23}c_{13} \\ s_{12}s_{23} - c_{12}c_{23}s_{13}e^{-i\delta} & -c_{12}s_{23} - s_{12}cs_{13}e^{-i\delta} & c_{23}c_{13}\end{pmatrix} \tag{1.21}$$

Unless the elements of the PMNS matrix are real, $P\left(\mu_e \to \nu_{\{}\mu\right) \neq P\left(\nu_\mu \to \nu_e\right)$. This happens because neutrino oscillations are not invariant under time reversal if any element of the PMNS matrix is complex. Nevertheless, the PMNS matrix can be multiplied by a complex phase without experiencing any change in the probability of oscillation. Time symmetry is only violated if one of the elements possesses a different complex phase than the others.

$$\begin{aligned}
\nu_e \to \nu_\mu &\xrightarrow{\hat{T}} \nu_\mu \to \nu_e \\
\nu_e \to \nu_\mu &\xrightarrow{\hat{C}\hat{P}} \bar{\nu}_e \to \bar{\nu}_\mu \\
\nu_e \to \nu_\mu &\xrightarrow{\hat{C}\hat{P}\hat{T}} \bar{\nu}_\mu \to \bar{\nu}_e
\end{aligned}$$

Table 1.1: *Scheme of how time, charge and parity symmetry act on neutrino oscillation*

If the elements of the PMNS matrix aren't real, CP symmetry is violated in neutrino oscillations. Hence, the antineutrinos PMNS matrix has to be identical to the neutrinos PMNS matrix under CPT symmetry. In the Standard Model there are six parameters that can be measured in neutrino oscillation experiments:$|\Delta m_{21}|^2, \theta_{12}, |\Delta m_{32}|^2, \theta_{23}, \theta_{13}, \delta$.

1.5 Sources of neutrinos

There are a lot of sources of neutrinos which provide a lot of evidences of the neutrino oscillation phenomenon. Neutrinos can be generated in reactors, due to the beta decays that take place during the nuclear reactions that produce energy. They can be also generated in the explosion of a nuclear bomb, or due to the nuclear reaction that take place in the earth or at supernovae. The most important sources that are being studied now are the solar neutrinos and the atmospheric neutrinos, which we proceed to introduce.

1.5.1 Accelator neutrinos

Neutrino beams can be produced at some particle accelerators. As depicted in Fig. 1.4, accelerated protons with an $E \sim GeV$ strike a fixed graphite target. As a consequence mesons are created, mostly $k^{\pm}$ and $\pi^{\pm}$. Then they are focused thanks to a magnetic field (produced by magnetic focussing horns) into a tunnel where the decay takes place. Due to the relativistic boost that kaons and pions undergo while decaying, neutrinos are emitted with the form of a beam instead of being emitted isotropically.

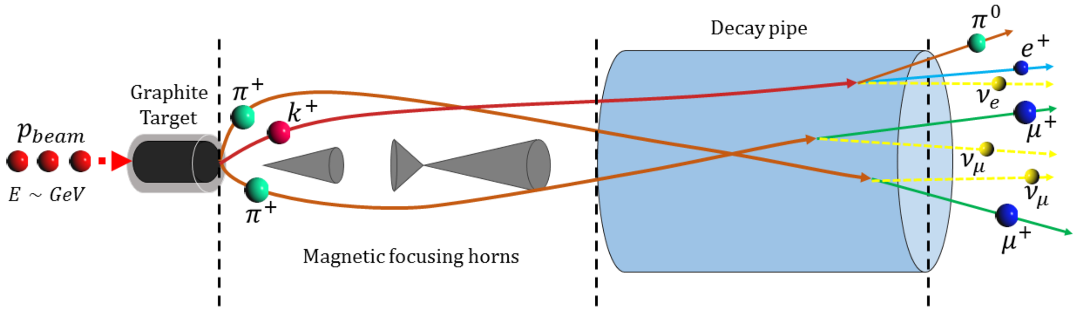

Figure 1.4: *Neutrino beam production scheme. The energy of the produced neutrinos can be tuned by changing the relative distance between the target and the focusing magneting horns.*

1.5.1.1 Solar neutrinos

The nuclear fusion that takes place in the core of the Sun is the origin of this neutrinos. The power generated by the reactions in which the weak interaction is of capital importance, produce a large flux of electron neutrinos with a complex neutrino energy spectrum. The different chain reactions involved in the creation of neutrinos are depicted in Fig. 1.5.

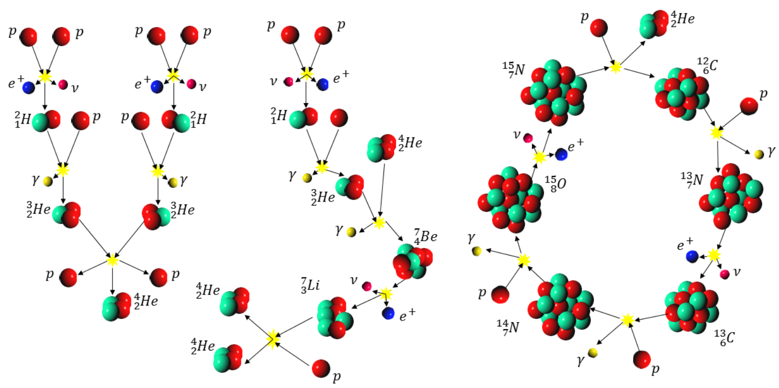

Figure 1.5: *Nuclear reactions in the core of the Sun responsible for the production of solar neutrinos. P-P Chain (left-middle), CNO Chain (right).*

The Standard Model allows to calculate the amount of neutrinos that the Sun produces in its internal reaction to produce energy. According to the Standard Model, neutrinos should have had no mass. The flavour was fix at the moment of its creation. As a consequence, the Sun should only emit electronic neutrinos from the fusion of H and He. When measured, there existed a discrepancy between the number of solar neutrinos that arrived to the Earth and the SM prediction. Only one third of the predicted neutrinos where detected. There must exist a neutrino oscillation therefore neutrinos weren't massless particles. This is known as the *solar neutrinos problem*.

1.5.1.2 Atmospheric neutrinos

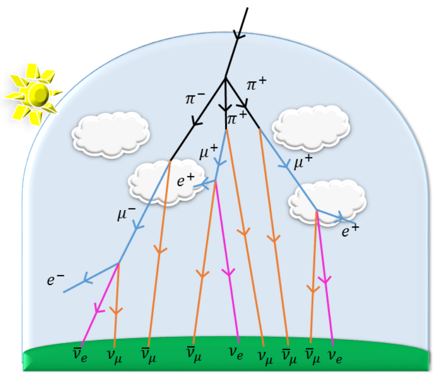

Figure 1.6: *Cosmic rays are composed mainly of protons (86%), He nuclei (11%), heavier nuclei (∼1%) and electrons (2%).*

Atmospheric neutrinos are the product from the interaction of atomic nuclei of the atmosphere with the cosmic rays (up to $10^{20}\,eV$). This interaction creates a shower of particles that ends up producing neutrinos by decay of the unstable particles created (see Fig.1.6). The cascade of particles is called Extensive Air Shower (EAS). These EASs can be detected by setting huge water tanks at ground level equipped with photomultipliers (PM). This PM detect the Cherenkov radiation that ultra relativistic particles emit by travelling in water faster than light does. Another way to detect them is by observing the scintillation light of the excited atoms during the process of the EAS. The light emitted by this atoms is in the visible and ultraviolet range.
When an EAS is generated, the only particles that reach the detectors are the muons and the neutrinos. Hadrons are extinguished and the electromagnetic radiation is absorbed by the atmosphere (almost).

Double-Bang events

Tau-neutrinos are not expected to come from extragalactic sources. It is thought that they are produced mainly as a product of the neutrino oscillation when they are on their way from the source to the detector. EAS containing taus are produce due to the CC interaction of tau-neutrinos in the atmosphere. For energies around $10^{18}\,eV$ the decay of the tau happens in a distance from the same order that the size of the EAS generating (almost always) another EAS that can also be detected. This double signature that comes from the same direction in a certain time is what is known as Double-Bang event [10].
When an neutrino enters the Earth and interacts via charged current with a nucleon of the atmosphere it generates a charged lepton and some fragments:

$$\nu_\varphi + N \longrightarrow \varphi + X \tag{1.22}$$

with $\varphi = (e, \mu, \tau)$. By interacting through a neutral current another neutrino is created instead of a charged lepton. Once the CC interaction has happened, the energy of the original neutrino is distributed between the charged lepton and the fragments that end up generating the EAS.

$$E_\nu = E_i + E_\varphi \tag{1.23}$$

E_ν is the energy of the incident neutrino, E_i is the energy that goes to the fragments and E_φ is the energy of the charged lepton.
In the case of ν_μ, when they interact via charged current, the interaction create an EAS that has the same characteristic than one created via neutral current (regardless of the flavour). This happens because the μ created after a charged current ν_μ interaction, almost doesn't interact with the atmosphere. For the typical energies, the length of the μ is bigger than its interaction length. The situation differs for CC interactions in which electrons and τ are involved. The electrons that come out as a product of the ν_e interaction, interact straightaway and generate a cascade of electromagnetic particles besides the hadrons that other fragments create. The mean lifetime of the τ created after the ν_τ interaction is way smaller than the one of the μ, despite they both propagate similarly.

$$\langle L \rangle \simeq \gamma c \tau \tag{1.24}$$

The equation above is the expression for the mean decay length of the ν_τ in the laboratory frame where γ is the Lorenzt factor and τ is the mean lifetime of the neutrino. Taking into account the typical energies, $\mathcal{O}(10^{18})eV$ or EeV, the mean propagation length in the laboratory frame is:

$$\langle L \rangle \simeq \frac{E_\tau}{[EeV]} \times \, 49\, km \tag{1.25}$$

The mean decay length is comparable to the length of the hadronic EAS created [10]. When a τ decays, it can create a second hadronic shower. This characteristic double signal only takes place in ν_τ interactions.

Chapter 2

Detection of Neutrinos

2.1 Methods of detection

As neutrinos lack of electromagnetic charge, its direct detection due to the ionisation of materials is not possible. Regardless of the method to detect (anti-)neutrinos, the particles must have a minimum energy to make the detection possible. The inexistence of a method for low energy neutrinos is due to the impossibility to distinguish its interaction from other effects.
As already pointed, neutrinos only interact via weak interaction with other particles so the size of neutrino detectors needs to be remarkably big in order to account for significant number of detected neutrinos. It is normal to isolate detectors by building them underground, this way the effect of cosmic rays and the background radiation can be partially avoided. According to the two ways in which neutrinos can interact with the detectors via weak interaction, the process can be described as :

- CC Interaction: If a neutrino has enough energy, it undergoes a change in which it is transformed into its flavour-partner lepton. If the detector can distinguish between (e, μ, τ), then it is possible to know the flavour of the incident neutrino. As already shown in Fig.1.2, the target particle, after the exchange of a charged W boson, will change its nature passing for example, from a proton to a neutron.

- NC Interaction: As the neutrino interacts with the detector, it transfers some of its momentum and energy to the particles that compose the detector. If the particle has electromagnetic charge and it is light enough, it can suffer an acceleration that makes it travel at relativistic speed. This causes the emission of Cherenkov radiation, which is possible to be detected with direct methods. This method of detection is valid for all three neutrino flavours but no information of its flavour is detectable.

2.2 The Cherenkov radiation

The Cherenkov effect is the phenomenon of emission of electromagnetic radiation. It happens when a particle with electromagnetic charge that moves through a dielectric medium surpasses the phase velocity of light in that medium.
According to electrodynamics, the phase velocity of light in the vacuum can be expressed as:

$$c = \frac{1}{\sqrt{\epsilon_0 \mu_0}} \tag{2.1}$$

where ε_0 is the electric constant and μ_0 is the magnetic constant. This is an upper limit for light that no particle can exceed. In a material, on the other hand, the speed of light depends on the refraction index, $v = \frac{c}{n}$. It is important to remark the difference between phase velocity (v_p) and group velocity (v_g). The phase velocity is the speed at which a plane wave with its peaks and valleys propagates. The group velocity is the velocity at which the envelope of the wave (pulse) propagates. They are related by the following expression:

$$v_g = v_p + k\frac{\partial v_p}{\partial k} \tag{2.2}$$

The phase velocity of light in a medium can be expressed as its celerity in vacuum times the inverse of the refraction index ($v = \frac{c}{n}$). This way, for instance, when a neutrino interacts via CC getting transformed into its partner lepton, a disruption of the electromagnetic field of the medium is produced, causing the polarisation of the medium. The perturbation can relax elastically back to the mechanical equilibrium when the particle has passed if its kinetic energy is low. In the case of high kinetic energy, the limited speed at which the medium reacts causes that the disturbance is left in the trail of the travelling particle. Its energy is radiated as a coherent shockwave. It is typical to compare it with the sonic shockwave that happens when an object reaches a supersonic velocity. The velocity of the waves is smaller than the velocity at which the object propagates so it is not possible for them to propagate forwards from the object. This way they form a shock front.

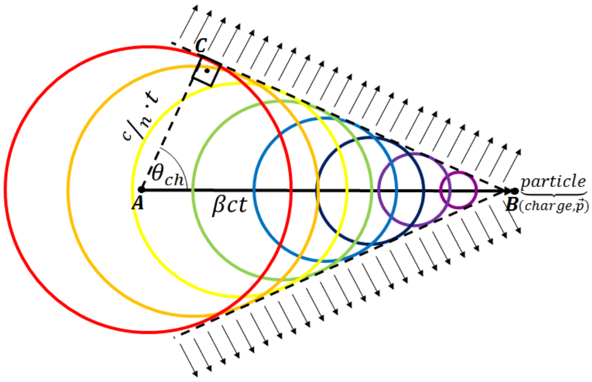

Figure 2.1: *Geometry of the Cherenkov radiation in the ideal case of a non-dispersive medium. The Cherenkov radiation is emitted isotropically along the path of the particle resulting in a ring-wave of photons with en angle θ_{ch}[11].*

The particle propagates in the medium with a speed $v_p < c$. Defining $\beta = \frac{v_p}{c}$ we can write the velocity at which the particle moves as $v_p = \beta ct$. The emitted radiation propagate at cn. The point A represents the particle at a time $t = 0$, the point B is where the particle is after a time t. During that time the particle has travelled a distance $d_p = v_p t = \beta ct$ and the emitted radiation $d_r = cnt$. This way we can express the angle in which the photons of the Cherenkov radiation are emitted with the respect to the path followed by the charged particle as:

$$cos\theta_{ch} = \frac{1}{n\beta} \tag{2.3}$$

The relationship between the number of photons (N) per unit path (dx) and wavelength (λ), also known as intensity, that a charged particle emits when the Cherenkov effect takes place:

$$\frac{d^2N}{dxd\lambda} = \frac{4\pi^2 z^2 e^2}{hc\lambda^2}\left(1 - \frac{1}{n^2\beta^2}\right) = \frac{2\pi z^2}{\lambda^2}\alpha sin^2(\theta_{ch}) \tag{2.4}$$

As $I \propto \frac{1}{\lambda^2}$, the short wavelengths dominate the emission of radiation and thus the Cherenkov spectrum is emitted mainly in the UV band with some emission in the blue visible range. The Frank-Tamm formula gives the number of photons emitted for a certain wavelength by a particle that moves in a medium at a $v_p > cn$.

$$\frac{dN_\gamma}{dx} = \int_{\lambda_{min}}^{\lambda_{max}} d\lambda \frac{2\pi\alpha z^2}{\lambda^2}\left(1 - \frac{1}{\beta^2 n^2(\lambda)}\right) \tag{2.5}$$

where α is the fine structure constant and the charge of the particle is ze.

2.3 Types of detectors

The type of neutrino and the energy it has determine the technology to use in its detection. Neutrinos from the sun have an average energy of $E_\nu \sim 1\,MeV$ while atmospheric neutrinos have $E_\nu \sim 1\,GeV$. These energies can be relatively low because a certain energy threshold has to be satisfied for an interaction to occur. In this section the main methods of detection are shown.

2.3.1 Radiochemical detectors

A tank is filled with a substance rich in an specific atom. Neutrinos interact producing a change of the atomic species and then the amount of the new atom is chemically extracted. The number of interactions is proportional to the amount of new material extracted. The substance or atom chosen to fill the tank determines the energy threshold for the neutrino interaction to happen.
For example, chlorine or a chlorine component serves as target for the neutrino interaction. The CC current can transform a Cl atom into an Ar atom by inducing the change of one neutron into a proton.

$$\nu_e + {}^{37}_{17}Cl \rightarrow e^- + {}^{37}_{18}Ar \tag{2.6}$$

This reaction has a neutrino energy threshold of $E_\nu \sim 0.814\,MeV$. The ${}^{37}_{18}Ar$ is periodically removed with He gas, which is afterwards cooled down to separate both substances. The amount of Ar atoms is accounted based on the number of electron capture decay. A similar method is carried out with Ga, which transforms into Ge.

$$\nu_e + {}^{71}_{31}Ga \rightarrow e^- + {}^{71}_{32}Ge \tag{2.7}$$

The threshold for this interaction is way lower, $E_\nu \sim 0.233\,MeV$.

2.3.2 Scintillators

Antineutrinos with a certain energy threshold interact with the protons in water in a reaction called inverse beta decay:

$$\bar{\nu}_e + p \rightarrow n + e^+ \tag{2.8}$$

The outcome of this reaction is a neutron and a positron. The positron annihilates with the electrons of the detector creating two photons with $E_T = 0.511\,MeV$ which excite the scintillators. The neutron is later captured by the cadmium atoms that are dissolved in water causing the emission of gamma rays $E \approx 8\,Mev$. The gamma photons end up interacting with the scintillators with an average delay of $\sim 100\,\mu s$. This double signature with space and time correlation allows to reduce the radioactive background.

2.3.3 Iron Calorimeter

This kind of detector uses an array of alternating absorber and detector material. This scheme provides enough mass to increase the probability of interaction and also a lot of points to track the trajectory of the particles produced. The most typical material used as absorber is iron or steel because of its density, its price and its ability to be magnetised. The detector layers are whether scintillators coupled to photomultiplier tubes or ionisation chambers.
With this technology only high energy neutrinos can be detected ($E \sim GeV$). This threshold is enough to favour the interaction via NC creating a shower of hadrons that precedes CC interactions. This produces high energy charged leptons that can be tracked as they penetrate through the detection layers. The length of the track and the curvature described according to the applied magnetic field permits the identification of the lepton in terms of energy and charge.

2.3.4 Cherenkov detectors

Cherenkov detectors use the Cherenkov radiation that is produced when a charged lepton moves through a medium faster than the speed of light in that medium. It is composed by a big volume of a material like water or ice in which a lot of photomultiplier tubes (PMT) are spread. A neutrino interacts via NC with a nucleon of the liquid water or the ice generating a charged lepton that moves with enough kinetic energy. The charged lepton creates an optical shock wave (Cherenkov radiation) that is detected by the PMTs. The signal has a characteristic ring-like pattern which is used to figure out some information like energy, direction and flavour of the lepton-originating-neutrino. (See picture below).

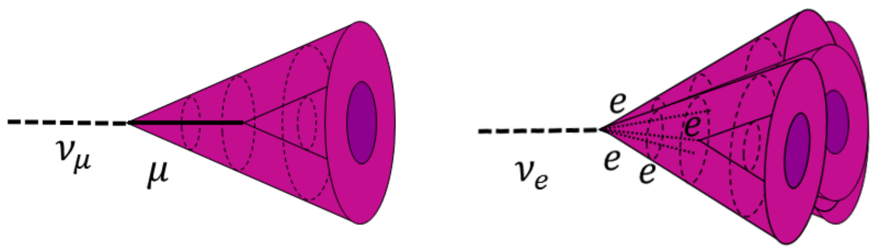

Figure 2.2: *The radiation produced by the Cherenkov effect from a muon generated by a ν_μ (left), yields a fine defined ring that photomultipliers can detect. On the other hand, when the predecessor is a ν_e (right), a shower of electrons is produced generating multiple cones that leave a diffuse ring mark in the photomultipliers array.*

Chapter 3

The IceCube Neutrino Observatory

The IceCube Neutrino Observatory is a 1 km^3 neutrino detector built in the ice that is situated in the Admundsen-Scott South Pole Station. Its main research goal is to detect high-energy neutrinos in the range from GeV to PeV. Inside this broad energy spectrum we can find the study of point sources to help explain the the origin of the highest energy cosmic rays, the study of gamma ray burst coming from the product of proton-proton or proton-photon collision, neutrino oscillation from EASs or even the indirect search for dark matter as an excess in the production of neutrinos in the sun [12] [13]. The IceCube experiment is also able to work at lower energies thanks to the Deepcore, a more densely instrumented sub-array of detectors that is able to reduce the energy threshold to $\sim 10\,GeV$ [14]. In order to improve the detection and reduce the uncertainties an upgrade will be carried out in the range of a few GeV, the IceCube Next Generation Upgrade (PINGU) [15]. PINGU is part of the IceCube-Gen2 Collaboration, which aims to expand the current detector populated volume of the IceCube experiment, from 1 km^3 to 10 km^3 [16].

The Precision Optical CAlibration Module (POCAM) is one of the fundamental parts of the upgrade: it will help studying the unitary matrix by precisely detecting ν_τ and will improve the reconstruction of EASs that give rise to Double-Bang-Events as a part of the search for astrophysical neutrino sources.

3.1 IceCube experimental setup

IceCube is composed by an "in-ice" array of Digital Optical Modules (DOM) placed under the surface (this includes also the DeepCore array which, as already mentioned, is a sub-array of more densely DOM-populated space) and an array made up of water tanks distributed all over the ice surface called IceTop.

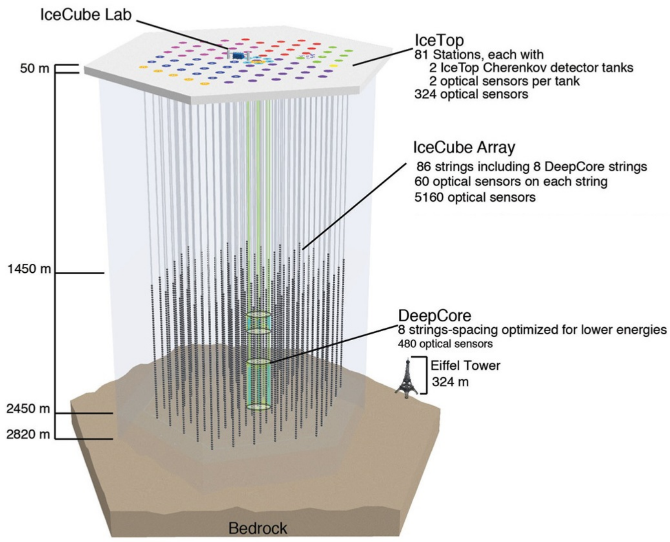

Figure 3.1: *Representation of the whole distribution of detectors of the IceCube experiment with its different parts*[17]*.*

Looking at Fig. 3.1 it is possible to distinguish the different parts of the array of detectors. The main part is inside the ice between 1450 and 2450 m deep (in total, 1 km^3 of ice full of instruments): 86 strings, each string containing 60 Digital Optical Modules (DOMs) making 5160 DOMs all together. These DOMs are spherical optical sensors, with 25,4 cm of diameter, provided with a photomultiplier tube (PMT) and a data acquisition board.

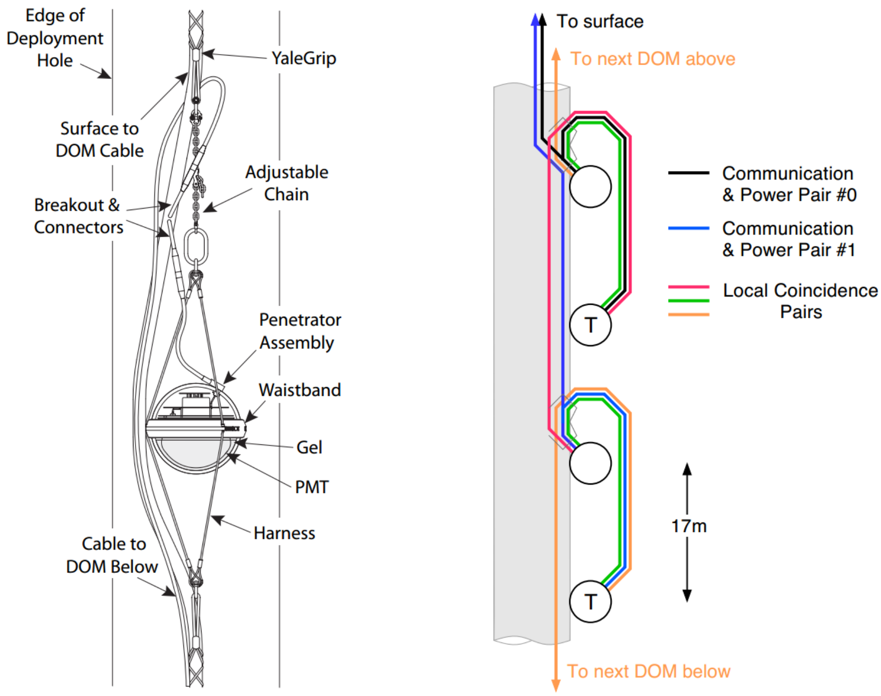

Figure 3.2: *Scheme of how the DOMs are fixed to the line and the different communication/power connections*[18]*.*

The strings are homogeneously distributed with a horizontal distance between them of 125 m. As shown in Fig 3.2, the vertical separation between optical modules in every string is 17 m.
The flux of atmospheric neutrinos reaching IceCube comes from all directions. While the Earth filters most of the muons produced by EASs coming from the northern hemisphere, atmospheric neutrinos coming from the same direction remain unfiltered and reach the detector (approx. 10^5 events per year). As the IceCube is placed in the South Pole, incoming neutrinos and muons from the southern hemisphere are not filtered and approximately 10^{11}events are detected per year [19]. These detected particles coming from the southern hemisphere are what is called, the veto of IceCube.
For this reason the photomultiplier tubes are oriented pointing to the geographical north of the Earth, in order to detect the Cherenkov light produced by the neutrinos that traverse the Earth in the southward direction. The energy threshold of the set-up to detect neutrinos is around 100 GeV.

DeepCore

The sub-array called DeepCore is a set of DOMs deployed deeper than 1750 m, densely instrumented, so the threshold energy is lower. Along with the 7 central standard IceCube strings, 8 closely-spaced strings full of sensors were deployed. The mean horizontal distance between strings is 72 m, varying from 41 m to 105 m. The vertical separation between the 50 DOMs at the bottom of the array (deployed between 2100 m and 2450 m of depth) is 7 m [18]. The remaining 10 DOMs are installed less deeper than 2000 m, with a separation of 10 m to form a veto cap that improve the capacity of rejecting the atmospheric muons coming from the south hemisphere . Between 2000 m and 2100 m of depth, the lines have no instrumentation due to the increased absorption and optical scattering of the region. Six of the DeepCore line's DOM use PMTs with a higher quantum efficiency (QE) than the standard modules. The other two lines have a mixture of improved and standard QE PMTs. The energy threshold for neutrino detection of this layout is 10 times lower than for the standard set-up (10 GeV) [14].

IceTop

This array is located on the surface of the ice (which is at 2835 m above sea level) and is composed by 162 tanks filled with ice and instrumented with PMTs spread over 81 stations [20]. In correspondence with the dense spacing of the DeepCore, sixteen tanks are situated along eight stations in the centre of IceTop. Every tank is separated 10 m from its station partner and is equipped with two standard DOMs, one with high-gain PMT ($5 \cdot 10^6$) and a second one with a low-gain PMT (10^5)[18]. The gain difference increases the dynamic range of detection for the EASs. The IceTop is able to work in a energy range between PeV and EeV. The denser array of IceTop has an energy threshold of 100TeV. It acts as a veto for in-ice events when combined with the muon bundles that are produced by EASs, permitting an improved understanding of the μ-background.

3.2 The Digital Optical Module

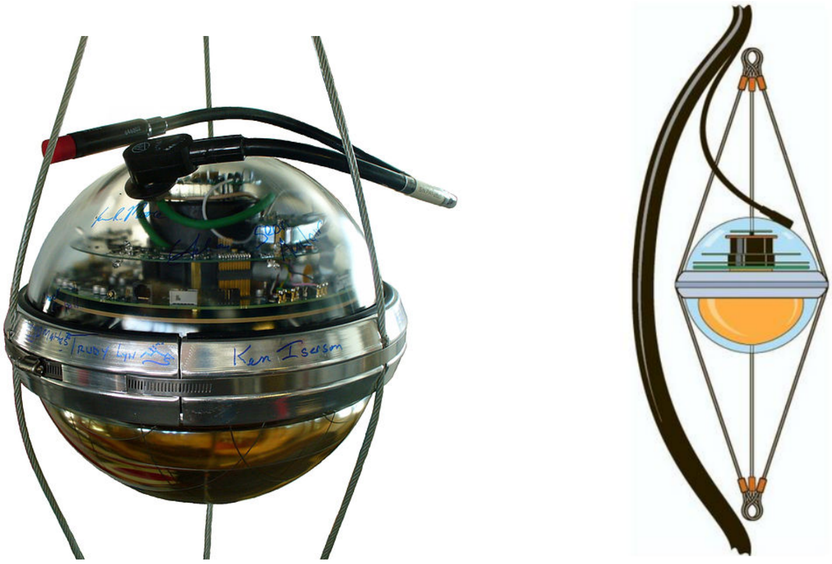

Figure 3.3: *DOM with the whole electronic inside and the fixing system attached to the central belt. Real picture (left), scheme (right)*[21].

The Digital Optical Module or DOM is the main detector of the IceCube Neutrino Observatory. As it can be seen in the picture, it consists of a glass sphere housing of $\varnothing_{out} \sim 33\,cm$ (10") and 1.25 cm of thickness that contains the PMT, the data acquisition board, the control board, the calibration circuit with the UV LEDs ($\lambda \in [340 - 505]\,nm$), the communication board and a high/low-voltage power converter. It also has a penetrator to introduce all the necessary cables for communication and powering purposes. The glass sphere is made out of two semi-spheres treated so that the amount of radioactive isotopes present in it is minimum, in order to reduce the background signal that it could provide. They are attached to the main string thanks to an aluminium waistband of $\varnothing_{out} \sim 18.5\,cm$ that acts as a harness.

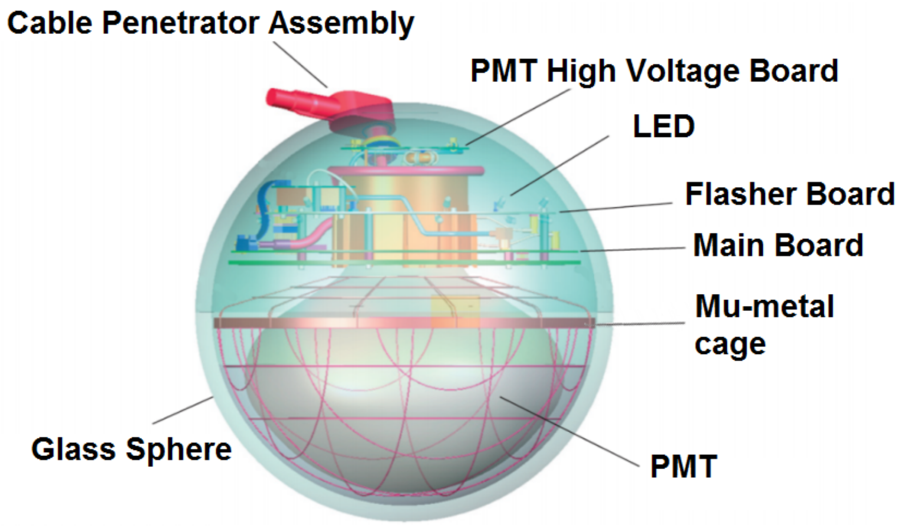

Figure 3.4: *Sketch of all the parts forming the DOM[22].*

Inside every DOM is the fundamental light sensor, a downward facing ø $\sim 25.4\,cm$ PMT. Two different kinds of PMT are used, Hamamatsu R7081-02 PMT with a quantum efficiency of 25% for the standard strings and Hamamatsu R7081-02MOD with a quantum eficciency of 34% for the DeepCore strings[14]. If the PMT signal surpasses the trigger threshold of 0.25 *photoelectrons*, it is digitalised whether by the Analogue Transient Waveform Digitaliser (ATWD), which can digitalise waveforms up to 422 ns, or by the Fast Analog-to-Digital-Converter (FADC), that can digitalise waveforms up to 6.4 μs. The Mu-metal cage is a metallic grid that covers the PMT and acts as a shield to protect it from the magnetic field of the Earth (See Fig. 3.4). The sphere is filled with a cured silicone gel that helps providing good optical coupling as well as mechanical support for the whole electronics inside.

3.2.1 The LED Flasher Board of the DOM

Every DOM is provided with a ring shaped LED Flasher Board that generates light pulses in-situ, in order to verify the timing response all through the analysis software chain, verify how the shower reconstruction algorithms perform in measuring position and energy, measure the optical properties of ice and measure the position of the DOMs once deployed in ice[23].

Besides the two types of DOM according to the quantum efficiency of the PMTs, there are also two kind of DOMs regarding the flasher board: There are 16 color DOMs or cDOMs equipped with multi-wavelength Flasher boards, 8 deployed on string 79, in the center of the grid, and 8 on string 14 on the edge. The LEDs have a nominal wavelength of 340 nm (UVTOP335-FW-TO39), 370 nm (NS370L_5RFS), 450 nm (LED450-01) and 505 nm (B5-433-B505) and are arranged in six pairs pointing outward horizontally.

The standard DOMs is provided with 12 LEDs (ETG-5UV405-30) with a wavelength peak of 405 nm also arranged in six pairs with a 60° of separation between adjacent pairs[1]. In each couple, one LED points downwards at an angle of 10.7° (with the respect to the plane defined by the board) emitting light horizontally after coming out of the DOM and the other one is pointing upwards at an angle of 51.6° emitting light at an angle of 48° after coming out of the DOM[18] (close to $\theta_{Ch}^{ice} = 41°$[23]).
An individual high-speed MOSFET is in charge of controlling the LEDs, this allows to turn them on and off individually and thus using any combination of all of them. The duration and photon output of the LED pulses can be modulated by varying the width and amplitude of the current pulse that drives the flasher board. Thanks to this each DOM can generate flashes from 10^6 to 1.4×10^{11} photons simulating the amount of light produced by showers between 7 GeV and 1 PeV. The ATWD gathers and records the LED current waveform in order to provides a rising time edge that allows to establish the onset of the optical pulse once known the turn-on delay. The LED can flash up to 610 times per second with a programmable rate. A detailed scheme of the electronic components of the flasher board included in a DOM is to be seen in Fig. 3.5.

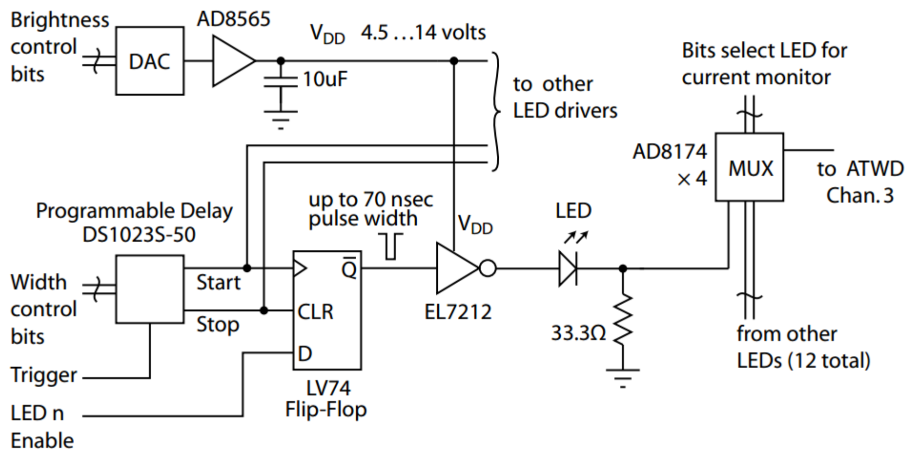

Figure 3.5: *Simplified scheme of a single LED flasher board included in each DOM[1].*

3.3 Neutrino detection in IceCube

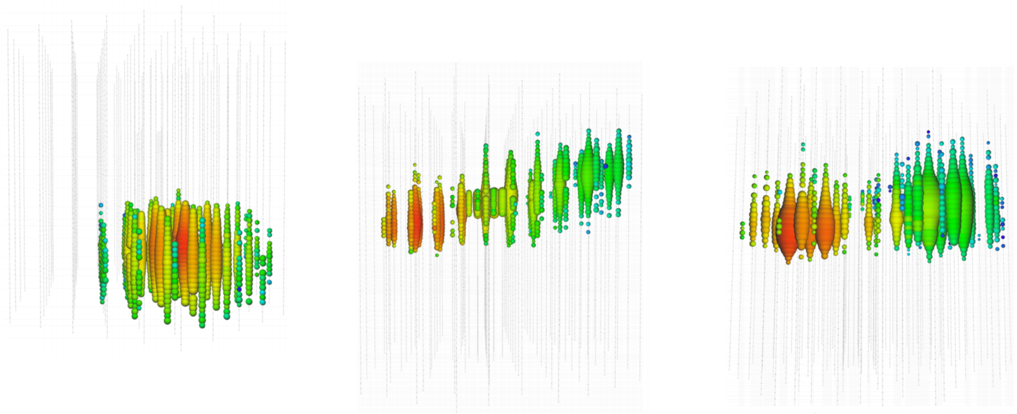

Figure 3.6: *Energy signature left by an electron neutrino (left), a muon neutrino (middle) and a tau neutrino (right) in the detector array of the IceCube*[24] [25].

The three families of charged leptons produce a characteristic "footprint" in the detector (see Fig. 3.6): this is how the flavour of the detected particle is determined.
The electron looses its energy very fast by causing electromagnetic and hadronic cascades . Due to the way it emits the energy, the direction of its father-neutrino can only be deduced with a resolution of $10°$ [26]. Normally the cascades are totally contained in the detector: this is a key factor for the task of energy reconstruction.
The signature of the muons consists of an hadronic cascade followed by Cherenkov radiation. Due to its relatively long lifetime $\tau_\mu = 2.197 \mu s$. This helps to improve the resolution when figuring out the direction of the ν_μ up to $1°$. The ν_τ produces the already mentioned "double-bang" event that makes it a good astrophysical neutrino candidate. Anyway, a ν_τ is yet to be detected by the IceCube.
In order to reconstruct the measured neutrino events with enough accuracy, it is necessary to understand ice properly. That's why ice models are needed. Different models and methods can be used but the most common consists into slicing the ice in multiple sheets and describing their properties according to a range of wavelengths.
The IceCube Observatory is located at the South Pole where the ice, accumulated from more than 45,5 million years, is excepcionally transparent to the UV radiation [27] [28]. This is important if we take into account that the radiation measured is the one produced by the Cherenkov effect.

3.3.1 The ice in IceCube

The layer of ice in which the detectors are located is not homogeneous. Two types of ice can be distinguished in the detector: the bulk ice and the refrozen ice of the holes where the strings are deployed.
The bulk ice is the ice that formed over millions of years accumulating different concentrations of dust by layers. This ice captured the conditions of the earth through the years of its formation. The refrozen ice of the holes contains gas bubbles due to the fast process of refreezing the water (it took around 3h). These bubbles of gas cause a difference in the absorption and scattering lengths of the ice from the surroundings of the DOMs. The absorption and scattering lengths are very important factors in order to understand the inhomogeneities of ice. They are connected to the density, dust concentration and structure of the ice. The more it is known about them, the easier it is to reconstruct the detected events. In order to determine both, the absorption and the scattering length, IceCube detectors must carry out the proper measurements. For this purpose, the LEDs that the DOMs are provided with, emit photons that are detected by the PMTs of other DOMs[23] (as represented in Fig. 3.7) .

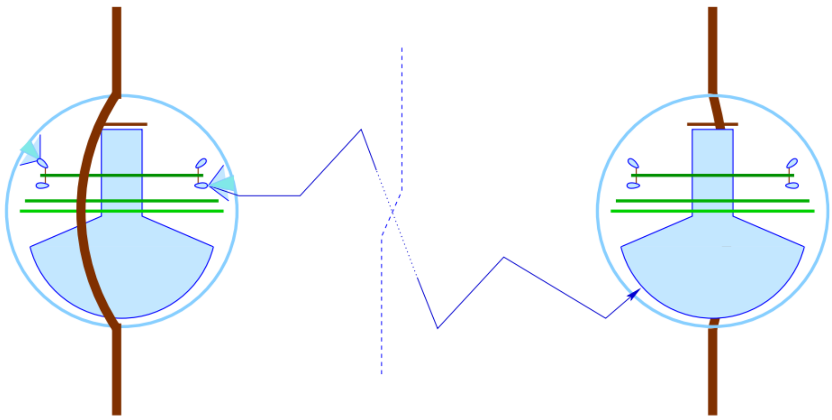

Figure 3.7: *Simplified schematics of the experimental setup: the flashing sensor on the left emits photons, which propagate through ice and are detected by a receiving sensor on the right*[23].

3.4 The Ice in IceCube

In order to rightly reconstruct the neutrino events, understanding and modelling the ice and its properties is a capital task. One method to properly describe the ice consists into dividing it in a series of sheets. Then the properties of every ice sheet for a set of wavelengths are defined. According to[23], the ice is described with a table of scattering and absorption depth-dependent parameters for $\lambda = 400\,nm$, $b_e(400)$ and $a_{dust}(400)$, the depth-dependent relative temperature $\delta\tau$ and six global parameters (α, κ, A, B, D and E'). The geometrical scattering coefficient, b_e, it can be written for every λ as:

$$b_e(\lambda) = b_e(400)\left(\frac{\lambda}{400}\right)^{\alpha} \tag{3.1}$$

The absorption coefficient, a_{dust}, is related to the dust that ice contains.

$$a_{dust}(\lambda) = a_{dust}(400)\left(\frac{\lambda}{400}\right)^{\kappa} \tag{3.2}$$

The total absorption coefficient is the sum of the dust contribution plus a time-dependent temperature component for pure ice,

$$a(\lambda) = a_{dust}(\lambda) + Ae^{-B/\lambda}(1 + 0,001\delta\tau) \tag{3.3}$$

$\delta\tau$ is the temperature difference in reference to a depth of 1730 m. This value comes from the predecessor of IceCube, AMANDA.

$$\delta\tau(d) = T(d) - T(1730\,m) \tag{3.4}$$

Scattering and absorption coefficients are related by the remaining parameters D and E,

$$a_{dust}(400) \cdot 400^{\kappa} \approx D \cdot b_e(400) + E \tag{3.5}$$

To determine the values of $b_e(400)$ and $a_{dust}(400)$, the information obtained by the DOMs during the flashing of the instrumented ice is fitted.
Ice models have improved since the first SPICE (South Pole Ice) came out for AMANDA[28]. The last models are the SPICE-LEA, which including an anisotropy detected in scattering length around the zenith angle, and SPICE3[29], which carries out the fit on 7 strings instead of one like the preceding models. It also includes an improvement in the dust-profile based extrapolation and the ice tilt from the dust logger[30].

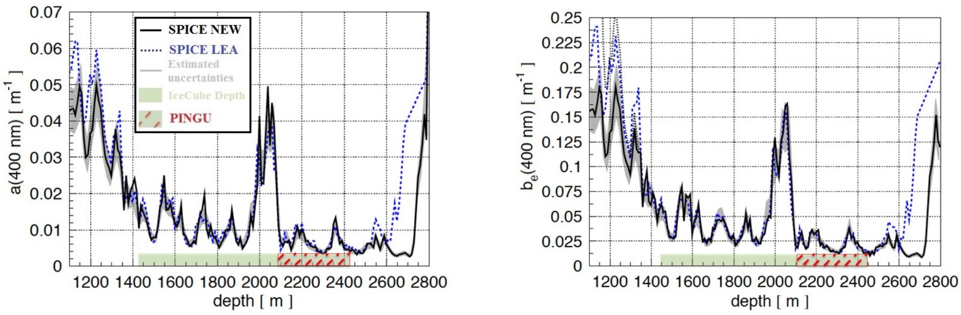

Figure 3.8: *Study of the LED calibration results of ice scattering.(Up) Effective absorption coefficient $a(400\,nm)$ vs.depth and (Down) effective scattering length $b_e(400\,nm)$ vs. depth[29].*

3.5 The calibration

When a high energy neutrino interacts (i.e. ν_μ) it creates a charged lepton (i.e. μ) that travels through kilometers of ice generating Cherenkov radiation. This interaction creates multiple showers of secondary particles that results in an overall light yield which is proportional to the energy of the lepton that generated it [1]. The time that takes a photon since it is created until it is detected depends on the position of each DOM in reference with the lepton's path. Each PMT can detect single photons or pulses up to thousands of them. The PMT generates waveforms that are processed to build events. Each fit takes into account:

- The light amplitude pattern and timing of the events detected by the DOMs.
- The optical characteristics of the ice.
- The time that takes for every DOM to response and its own sensitivity.

After fitting all this information, the direction and energy of the charged lepton can be reconstructed and hence, the parent neutrino. An example of the signature left in the volume of detectors by a cascade can be seen in Fig. 3.9.

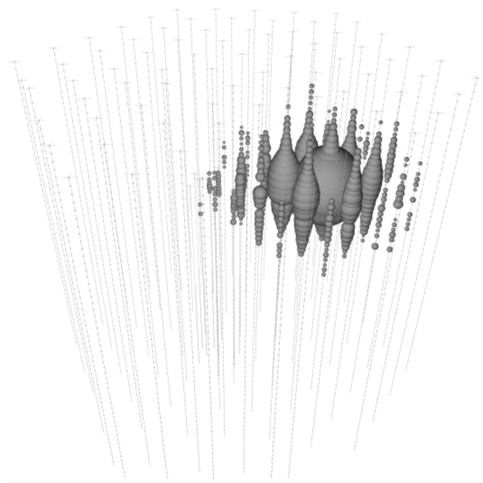

Figure 3.9: *A cascade that deposited 1070 TeV in the detector. Its energy can be determined directly since the cascade is completely contained in the instrumented volume [26].*

Therefore, the precise calibration of these elements plus the ice model is decisive for an accurate event reconstruction. To calibrate the detectors in IceCube, LED flashers located on the boards of the DOMs were used as well as calibration in-ice lasers and low energy muons (muon tomography). Any uncertainty coming from this calibration methods would compromise the systematic uncertainties of the detectors.

3.5.1 Energy calibrations

Almost the whole responsibility of the reconstruction of the events relies on the calibration of the PMT sensitivity, on the propagation of the Cherenkov radiation through the ice, the poissonian fluctuation of the collected charge and on the energy scale calibration.

Energy Resolution

In order to specify the precision to which de detector can reconstruct the deposited energy it is necessary to determine the energy resolution.

$$E.R. = \frac{E_{reconst.} - E_{true}}{E_{true}} \tag{3.6}$$

It defines the precision with which the deposited energy by the particles inside the detector can be determined. By working with simulations and experimental data, the energy resolution extracted for IceCube is of approxymately 15%. The fluctuations in the light yield and the amount of charged particles in the hadronic showers increase the uncertainty in the energy measurement. Moreover, the methods and models used to describe the development of showers introduce uncertainties. The first kind of uncertainties can't be easily improved. The second can be significantly improved by using a self-calibrated,isotropic photon source. Here is where the POCAM comes into play.

Energy Scale

The calibration of the energy scale is based in two methods:

- The detection and simulation of minimum-ionizing muons sets the standard brightness candle.
- The data from the calibration of laser pulses establishes the linearity of the DOM's response and the photon-counting procedure.

This combination sets the offset between the detected and the real charge detected by the PMTs[26].

- Minimum-ionizing Muons

Minimum-ionizing muons are a very good source of Cherenkov radiation with a constant known light emission: they leave a well-defined track in the detectors array and are very abundant. Low energy single muons are selected because they deposit little light in the outer strings and their track stops in the detector fiducial volume. The track usually has an inclination of 45°-70° in the zenith direction. This maximises the probability that the Cherenkov cone interacts on the active side of the down-facing PMTs. The observed PMT charge is then compared with the expected value, for this purpose the quality of the event reconstruction fit needs to be high. To carry out the calibration, only a subset of DOMs are used. They are located in the deep part of the detector volume where the ice's absorption length is $\sim 200\,m$. For each of these DOMs, the muon track is reconstructed but the information of the DOM in question is excluded . Thanks to simulations it is possible to know that this method reconstructs the muon direction within $\sim 2°$ direction and the track-DOM distance within $\sim 10\,m$[26]. After comparing the detected and the expected charge, an excess of 5% was found. At certain distances, the deviation goes up to 9%. See Fig. 3.10.

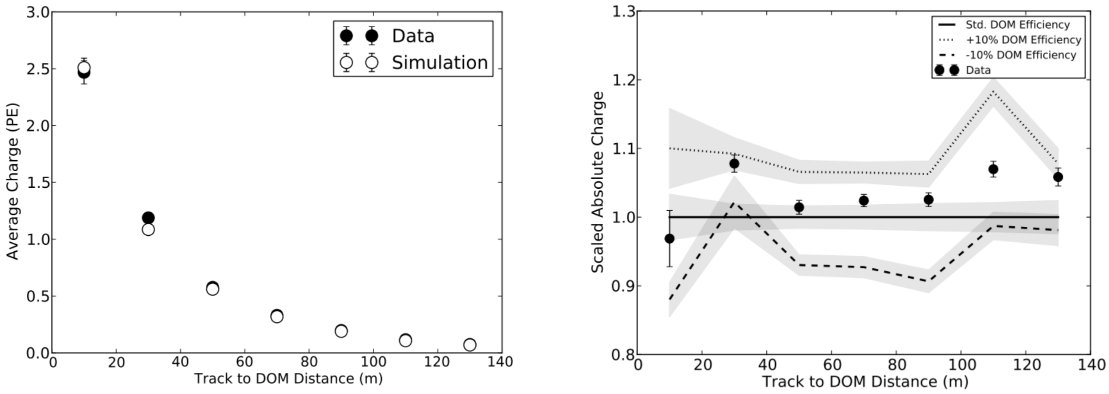

Figure 3.10: *Absolute charge measurements with minimum ionizing muons.(Left) Average observed charge against distance between the DOM and the minimum-ionizing muon reconstructed track for the gathered data and the simulation. (Right) Average charge against distance between the DOM and the minimum-ionizing muon reconstructed track normalised to the expected charge from simulation[26].*

Monte Carlo simulations points that the sample that satisfies the above mentioned requirements is composed of over 95% of single muons with $\bar{E} = 82GeV$[26]. The observations are therefore dominated by single photoelectrons.

- High-enery Linearity Calibration

With the help of two $337\,nm$ pulsed nitrogen lasers it is possible to verify the energy scale that IceCube detectors work in[26]. They emit light pulses that only differ on the amount of emitted photons and correspond with the light emission of the electromagnetic showers in the range of $1 - 100\,PeV$. The variation of the amplitude of the laser pulses generates waveforms in the surrounding PMTs that are scaled copies of each other. It implies that the extrapolation of the energy scale can be done. Any possible non-linearity would appear as a distortion in the shapes of the waveforms for different amplitudes. See Fig. 3.11.

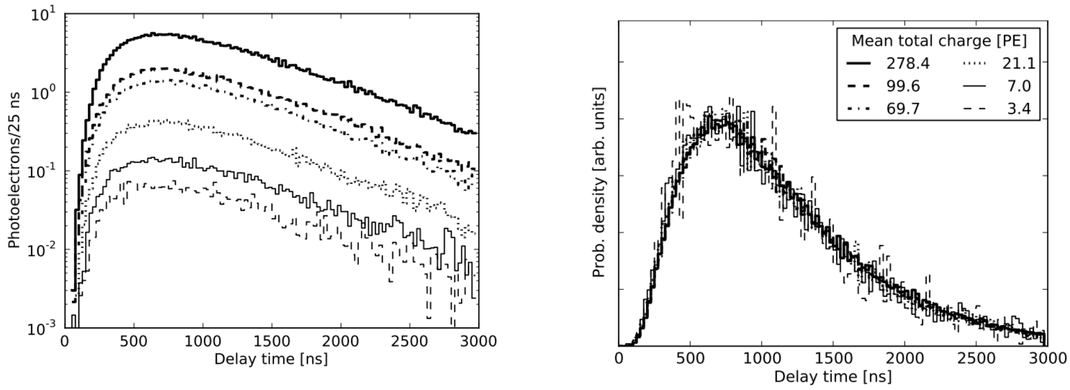

Figure 3.11: *(Left) Charge collected vs time from the calibration laser flashes with 6 different intensities for a distance of* 246m. *(Right) Same distribution normalised to each transmittance setting*[26].

3.5.2 Timing Calibration

To perform the time calibration of the DOMs, a procedure called "Reciprocal Active Pulsing" was developed. It consists of the comparison of the phase and frequency of two fast bipolar pulses coming from the DOM and from a master GPS-controlled oscillator located on the surface. The DOM has a free running local oscillator (20 MHz) installed and a GPS controlled oscillator located in the surface provides the second signal. At known intervals, the surface device sends a pulse to the DOM which the DOM "reciprocates" by answering with an identical pulse after a determined delay. The resulting waveform is digitised and read out. It allows for the verification of reciprocity between both pulses. As it is to suppose, the time of the whole GPS-DOM-GPS travel depends on the length of the cable connecting both devices. How this time variates from calibration to calibration gives the measurement of the precision of the time calibration method. This results in a time resolution of at least 2 ns as shown in Fig. 3.12.

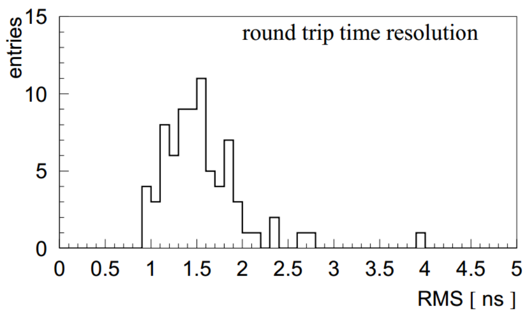

Figure 3.12: *RMS variation of the GPS-DOM-GPS time for all the DOMs*[31].

3.5.3 Geometry Calibration

The goal of carry out a geometry calibration is to determine the relative position of all DOMs. This is done in three steps and gives rise to an estimation of the positions with 1 m of precision[32].

Step 1: Generating the 3D coordinates for all DOMs.

The first stage employs data obtained during the processes of drilling and deployment of the strings. The monitoring of the precise position of the drill tower and the x-y drift versus depth allows to determine the first (x,y) set of coordinates for every DOM (See Fig. 3.13). The z coordinate is obtained by pressure measurements of the bottom DOM (#60) on a string. Then the vertical DOM spacings are subtracted from the total depth of the string until the top DOM (#1) is reached. The depth of every DOM is converted to z coordinates by normalization of the surveyed floor elevation to the origin of the coordinate system. This way the three coordinates x,y,z of every DOM are obtained.

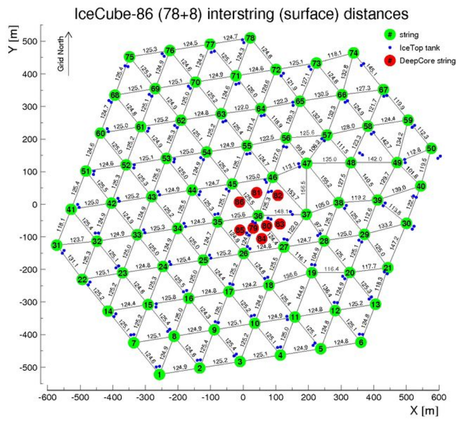

Figure 3.13: *Distances between strings at the begining of 2011*[32].

Step 2: Relative depth offsets between strings

In this step the interstring flasher data is used in order to determine the relative depth offsets between strings. For a certain flasher, six horizontal LEDs are flashed and up to six adjacent strings read out the pulses. The result is a travel time distribution. A partial Gaussian is fitted to the leading edge of the time distribution. The result is an estimate of the shortest travel time recorded, this is the prompt time and corresponds theoretically to an unscattered, straight-line propagation: $t_0 = \mu - \alpha \cdot \sigma$. The mean and sigma of the Gaussian are μ and σ, and α is a factor that corresponds with the 1% of the peak value of the Gaussian. The fitted prompt times are then converted to distances to figure out the distance between DOMs ($d = c_{ice} \cdot t_0$). By plotting this distance versus the vertical distance between flasher and receiver ($z' = z'_{receiver} - z_{flasher}$) for every triggered DOM, a hyperbola is obtained. This hyperbola can be fitted with the hyperbola equation: $d = \sqrt{D^2 + (z' - \Delta z)^2}$ (See Fig. 3.14). Where D is the horizontal distance between the emitting and the receiving string and Δz is the offset of the relative depths of the two strings.

The iteration of this process results in a relative offset (Δz) for every string that provides a correction to the z coordinate obtained in step 1.

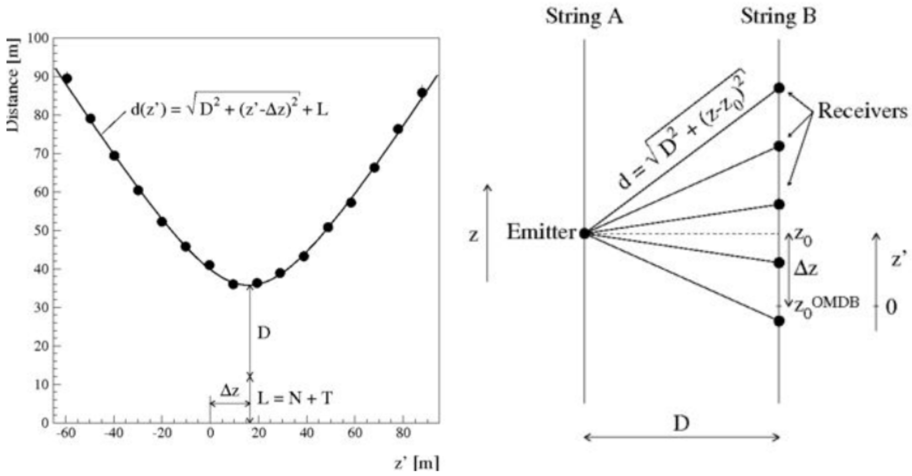

Figure 3.14: *Scheme of the fitted hyperbola obtained with the inter-string flasher measurements*[32] *(Left). Illustration of the method used to fit a hyperbola to receiver distance vs relative depth*[32] *(Right).*

Step 3: Tracking deformations due to ice shear

This step uses muon tomography in order to keep track of the deformations that the ice shear causes on the DOM array over time. Muon tomography allows to calibrate the position of each DOM individually without assuming the string position. On the other hand, it relies on the precision of the track reconstruction. This can cause that any uncertainty in the reconstruction method will propagate to the uncertainty in the calibration.

The different ice sheets move at different velocity. For example, the surface moves at 10 $m/year$ whereas the bedrock velocity is zero. As the deep ice in which the DOMs are placed is subject to shear, the deepest DOMs could move around 1 m with respect to the others that are closer to the surface[33]. Muon tomography is used to track the coordinates of every DOM over time. The tracks of high quality, down going muons that implicate a certain DOM are selected. The calibration of the DOMs is carried out by excluding the data of the specific DOM from the likelihood function of the track. The resulting likelihood of the track can be converted into a three dimensional map of the DOM position. The point corresponding to the highest likelihood is the best fit position of the DOM.

3.6 IceCube-Gen2 Upgrade

Due to the high effectivity of IceCube, the necessity of an extension to improve the quality of the detections and reduce the energy threshold was clear.The high energy extension of IceCube, IceCube-Gen2 attempts to improve the sensitivity of the measurements of the patterns created by the three families of neutrinos. This task will be achieved by increasing the detector volume in a factor of 10. This makes a total volume of 10 km^3 of antarctic ice[25]. The extension of the detector volume is possible without a huge effort because the antartic ice is clearer as previously thought. This fact was known after the drilling and study of the properties of the bulk ice. All in all, it would be possible to increase the distance between strings in order to build a bigger detector. As the detector mass is increased, the possibility of measuring higher energy neutrinos ($PeV \sim EeV$) is to be taken into account. Also, by increasing the population of DOMs in a certain zone of the detector, the energy threshold can be reduced and therefore, the problem of the Neutrino Mass Hierarchy can be studied in more detail with better data.

3.6.1 Precision IceCube Next Generation Upgrade (PINGU)

PINGU is the low energy extension of IceCube in the frame of IceCube-Gen2. The following picture shows an scheme of the future deployment of PINGU.

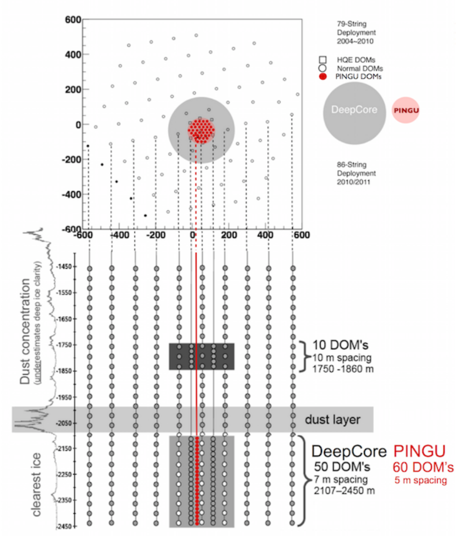

Figure 3.15: *The Precision IceCube Next Generation Upgrade Upgrade. (Up) Birdseye view of PINGU and size comparison with DeepCore. (Down) Side view of how PINGU is planned to be deployed between 2150 m and 2450 m*[13].

It will lower the energy threshold to a few GeV by populating a volume of the DeepCore with more DOMs. This will make PINGU the largest effective volume for neutrinos at the energy threshold of a few GeV. As in IceCube, the ice will be used as calorimeter. That's why, as discussed in Section 3.4, knowing the characteristics of the bulk ice is of main importance. By using low energy muon tomography and in-situ calibrated sources of light, the absorption and scattering in IceCube was determined with a 10% of precision. Thanks to PINGU, the precision of the ice properties in the volume in which PINGU is located can be increased to a 2-3%. To detect neutrinos with an energy threshold of a few GeV, the dominating process is called Quasielastic scattering (QE). In this kind of interaction a lepton is produced via CC[7].

$$\nu_l + n+ \rightarrow p + l^- \tag{3.7}$$

$$\bar{\nu}_l + n+ \rightarrow n + l^+ \tag{3.8}$$

This leptons produce Cherenkov radiation that can be detected by PINGU. Although the event signatures that characterise this interactions are the same for IceCube than for PINGU, at this energy scale, the volume of the detector will contain most of the particles created in the shower induced by the neutrino interaction. This isn't normally the case in IceCube, where the majority of this particles are only partially contained. In addition, under $E_{threshold} \approx 100\,GeV$, the hadronic shower produced by the neutrino interaction makes an important contribution to the fraction of the Cherenkov radiation. This fact can not be overlooked so the event reconstruction strategies may differ from those of IceCube[15].

3.6.2 Goals of PINGU

The motivation for PINGU is to distinguish between the normal and the inverted NMH at 3σ in an interval of less than 4 years of data gathering[15]. It is possible to expand the search for dark matter as well as use neutrino tomography to carry away the first-ever direct measurement of the composition of the core of the Earth[34][13]. Besides this, it will also be possible to study the ν_μ disappearance[35], measure the appearance of ν_τ with high precision[15] or distinguish the correct θ_{23} octant with more than 5σ if the NMH is finally normal.

3.6.3 Calibrations systems of PINGU

PINGU uses the amount of measured Cherenkov radiation, timing and location to reconstruct the track of the neutrino that induced the detected lepton. As in the case of IceCube, the accuracy of the event reconstruction depends on the proper calibration of the detector systems.

Calibration systems/devices

- **Cameras** By deploying a camera in at least one of the strings, the effectiveness of the degassing of the hole ice will be verified. If several cameras were to be deployed, it could increase the precision of the measurements of the bulk ice as well as help with the geometry calibration. This would enable the determination of the azimuthal orientation of the DOMs[15].

- **LED flashers** Every DOM of IceCube contains a LED flasher board to help measuring the ice properties, timing and PMT sensitivity together with its location and orientation. The DOMs used in PINGU, called PDOMs, will be equipped with an LED flasher board according to the necessities of the project.

- **Precision Optical CAlibration Module (POCAM)** A lab-calibrated light source in the core of PINGU will help to increase the energy resolution of the whole IceCube experiment. The monitoring of the LED light pulses will increase the confidence in measurements of the ice characteristics. By using different wavelengths and different brightness settings, the precision of wavelength dependent studies of ice properties could be increased. The characteristics of the POCAM, its components and its utility are discussed in Chapter 4.

Chapter 4

Precision Optical CAlibration Module (POCAM)

The Precision Optical CAlibration Module (POCAM) is a device developed in order to help reduce the primary experimental systematic uncertainties. These uncertainties are caused by the partial understanding of the optical properties of the antartic ice[23]. Its goal is going from the current systematic uncertainty of 10% to a level of a few %. Furthermore, the POCAM can work in parallel with other calibration devices from IceCube-Gen2 like the LEDs flasher boards. In this chapter, the overall characteristics, as well as its intention and composition will be described.

4.1 Characteristics

Figure 4.1: *POCAM assembly with an X-ray side view of all its components.*

The POCAM is an isotropic, multi-wavelength source of light pulses [36] [37]. It can be divided in three sub-systems: a pressure housing, the digital and the analogue circuit boards and the light diffuser elements. As it can be noticed in Fig 4.1, the external part is composed by two glass hemispheres that are connected to a cylindrical housing made out of titanium in order to resist pressure and temperature changes. A Kapustinsky-like circuit [38] drives a multi-wavelength array of LEDs that is able to generate light pulses of $\sim\ 10\,ns$ and $\mathcal{O}(10^8) - \mathcal{O}(10^9)\gamma$. A PTFE sphere in each hemisphere is responsible for the diffusion of the light pulses so as to produce isotropic, homogeneous illumination of the ice. It aims for the light every hemisphere to reach and isotropy of within 2% and the total light output to be determined within a 2% thanks to the built-in photosensors. A simulation of the final structure of the POCAM can be seen in Fig. 4.1.

4.2 Components

4.2.1 The pressure housing

The design of the POCAM has suffer a process of evolution through iteration in order to solve the different problems that arose from the different components and the goals that it was meant to achieve. See picture below:

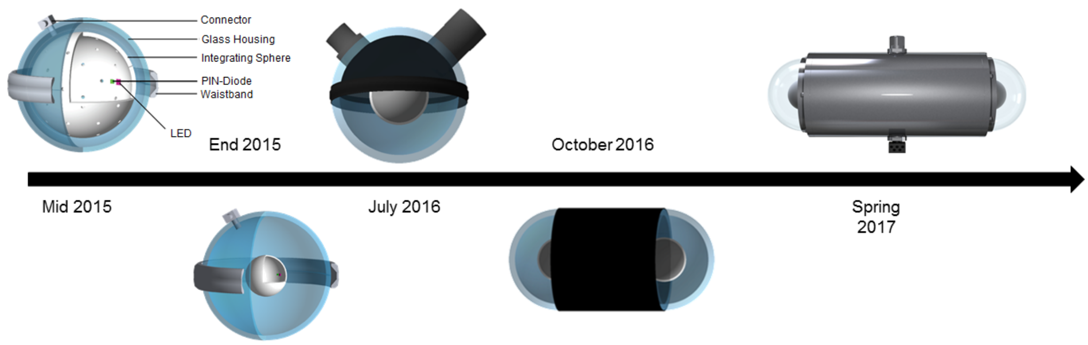

Figure 4.2: *Evolution in time of the design of the POCAM* [1].

Since the first theoretical prototype, some design-related issues appeared, the spheric-shaped POCAMs left very little room for the electronics. The waistbands produced shadows that lowered the light output. After several iterations and in collaboration with Nautilus Marine GmbH, the pill shape for the housing was adopted. This design allows to emit light pulses in 4π minimising the shadowing of the fixing system and leaving enough space for the electronics.

[1]Image rendered by Kilian Holzapfel.

The housing of the first-ever completed and deployed prototype of the POCAM is composed by a 15 mm thick titanium cylinder with two open ends. The outer and inner diameter are 130 mm and 100 mm respectively. On both ends, two glass hemispheres made of BK-7 with a thickness of 7mm and a diameter of 11,43 cm (4,5 $inches$) are attached.

Figure 4.3: *Housing and fixing system of the POCAM* [2].

The housing is able to resist the pressure corresponding to a 15km water column, it is to say, at least 1500 bar. Thus, the almost 10-fold pressure that the POCAM should resist at is destination in Antarctica and Lake Baikal will suppose no problem (Notice Fig. 4.3). Although the glass hemispheres are finally made of BK-7, other materials were studied. The decisive criteria is the transmissivity. Due to the characteristics of the IceCube-Gen2 and the Antarctic ice, the glass needs to have a good transmissivity for $\lambda = 350\, nm$ [39]. As shown in Fig 4.4, three different materials were taken into account: UV Silica/Quartz, BK-7 and Borosilicate. All of them were suitable in terms of transparency and refractive index but the BK-7 was the one that showed the desired behaviour in terms of transmissivity.

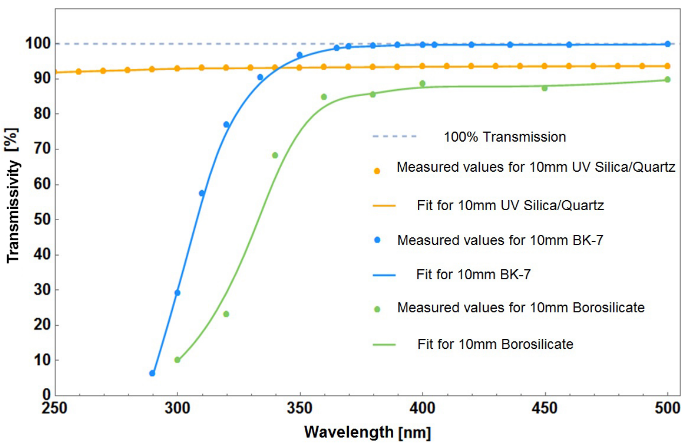

Figure 4.4: *Transmissivity spectrum for the wavelength interval between 250 and 500 nm. The materials are shown, Quartz (yellow), BK-7 (blue), and borosilicate (green) for a glass thickness of 10 mm* [40] [41] [42].

[2]Image rendered by Kilian Holzapfel.

4.2.2 The electronics

Inside the pressure vessel and fixed to the titanium flange, two circuit boards can be found. A digital and an analogue circuit board. Together they form a unit that communicate, emit light and register it. The POCAM counts with two of this functional units sharing a common voltage supply board. The POCAM communicates with the exterior through a port situated on one side of the cylinder. It is opposite to the vacuum port installed to remove any trace of humidity that could damage the circuits when deployed and under operation.

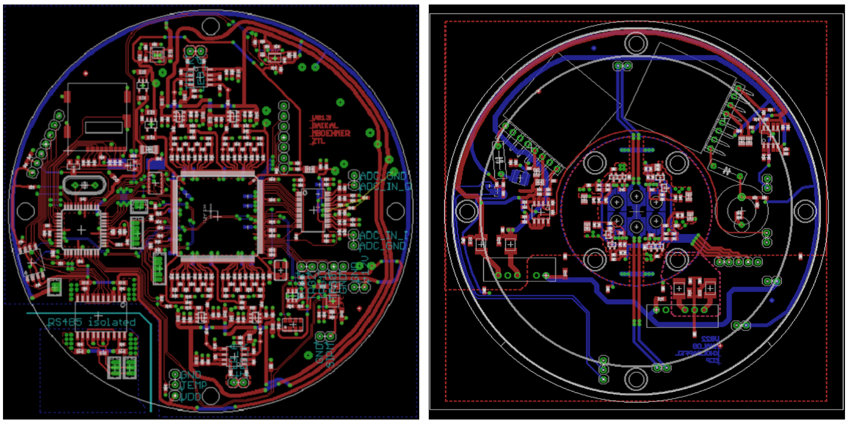

Figure 4.5: *Digital circuit board including a micro-controller, an FPGA, memory chips, an ADC, and a FPGA based LED controller (left). The analogue circuit board includes 6 LEDs, two charge sensitive amplifiers connected to a PIN Diode and a SiPM, also included in the board (right).*

- **Digital Circuit Board:** The Digital circuit board is composed by an FPGA, an analogue-to-digital converter (ADC), a micro-controller, memory chips and a LED. The FPGA is in charge of every timing sensitive task like the reading and buffering of the data of the ADC, operating the signals to control the analogue board and controlling the two FPGA-drived LEDs. The micro controller manages the communication between boards, the communication with the exterior and also drives the writing and reading of the information in the memory chips. Thanks to the two channel ADC, the signals of the two light sensors are digitised.

- **Analogue Circuit Board:** The analogue board contains the light emitting sub-circuit, which is triggered by the FPGA, and the light measuring part. A Kapustinsky-based circuit is responsible for the emission of light with four LEDs (two green and two blue LEDs). The light pulses are measured by two different light sensors, a SiPM and a PIN Diode, also contained in the analogue circuit board. The information that both sensors provide is read out via the ADC thanks to two Crema charge sensitive amplifiers. The characteristics, evolution and study of this circuit board will be extended in detail in the next chapter.

4.2.3 Light diffusing elements

Figure 4.6: *Principle components of the POCAM including the PTFE sphere, the plastic protector ring and the circuit shielding.*[3]

On the top of the LED array there is the diffusing PTFE sphere. Its goal is to transform the anisotropic emission of light from the LEDs into an isotropic, diffuse emission. The CNC-milled hollow PTFE sphere has a wall thickness of 1 mm and a diameter of 50 mm. It has been designed and developed at the TUM (See Fig. 4.6). A 0.5 mm thickness PTFE "plug" connects the bottom of the diffusing sphere and the LED array. The coupling is protected with a plastic ring that works as shield to avoid part of the light to leave through the plug (this could cause wrong lectures on the light sensors). The pulse is turn from anisotropic into isotropic by reflecting itself inside the PTFE sphere. After an average of 7 reflections, the light emitted is highly isotropic[43]. A scheme of the lambertian reflection produced inside the PTFE sphere is shown in the following picture:

[3]Image rendered by Kilian Holzapfel.

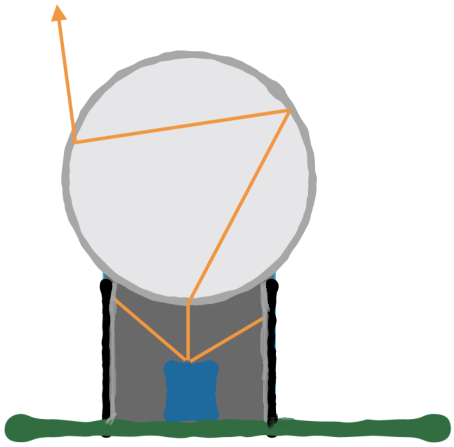

Figure 4.7: *The light comes into the sphere and, because of the spherical symmetry and the lambertian reflection of the material, abandons it isotropically* [4].

The selection of the material, as well as the thickness of the sphere was of main importance. Due to its characteristics (transmissivity and reflectivity), the sphere was chosen to be made out of optic Teflon (PTFE). The following figure shows the variation of the transmissivity and reflectivity of PTFE depending on the thickness of the material.

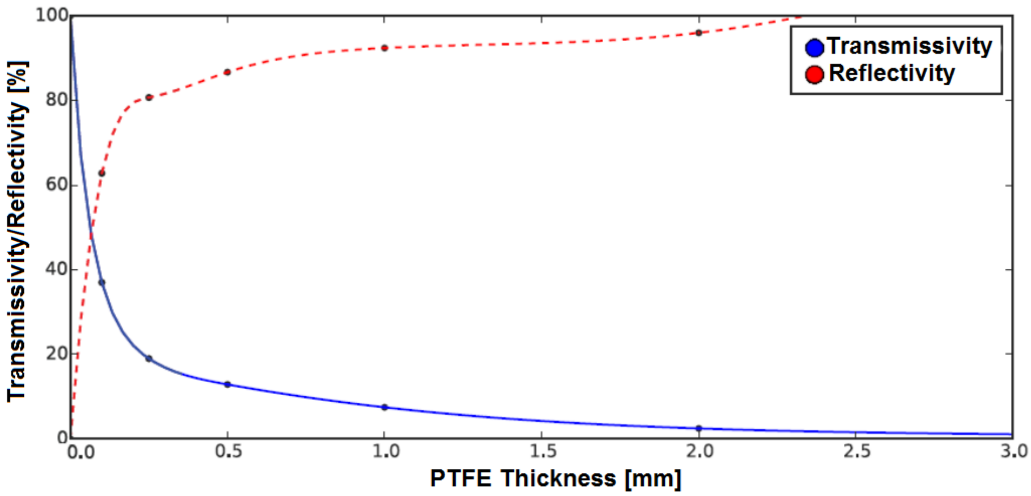

Figure 4.8: *Transmissivity and reflectivity of PTFE vs PTFE Thickness*[43].

In order to choose the better ratio between the size of the sphere and the thickness of the walls, several simulation with GEANT4 where run. Also, the technical issues concerning its manufacture were taken into account (Fig. 4.9).

[4]Image rendered by Kilian Holzapfel.

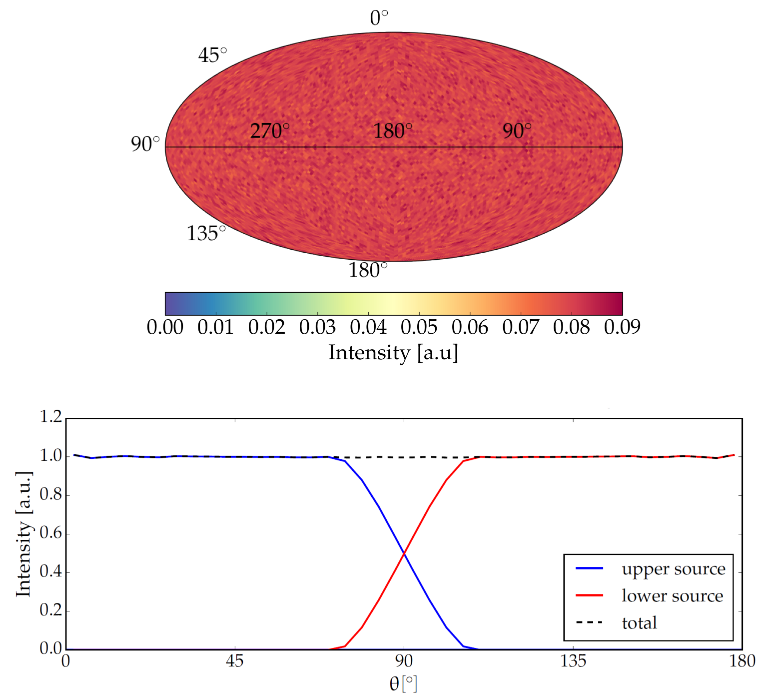

Figure 4.9: *(Up) Skyplot of the isotropy simulation for a PTFE sphere with* $= 50$*mm and 1 mm thickness at a distance of 20 m*[43]. *(Down) Angular intensity distribution.*[5]

The isotropy of two versions of the PTFE sphere where measured. The old version was a PTFE sphere with the same diameter and thickness but made out of two hemispheres that joined by the equator. The new model, currently mounted in the POCAM, is shown in Fig. 4.10 together with isotropy measurements of both models.

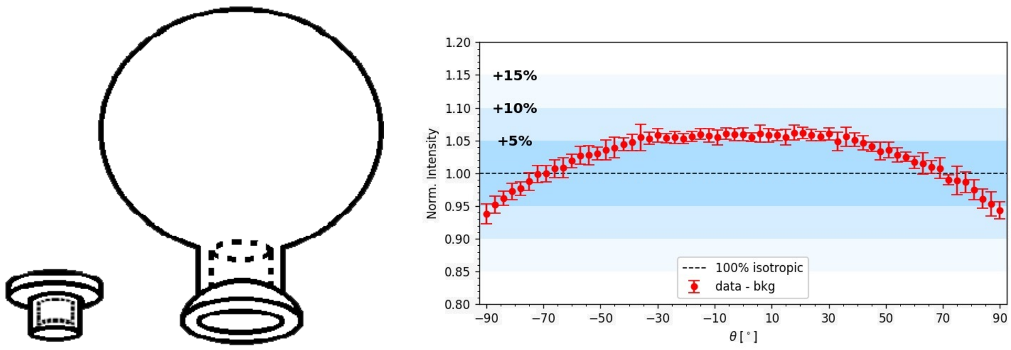

Figure 4.10: *(Left) Scheme of the shape of the new model of PTFE Sphere. (Right) POCAM integrating sphere isotropy measurements* [6].

The angular spectrum with $\theta = 90°$ corresponds with the top part of the sphere. In the plot, the mean of every measurement corresponds to an intensity of 1.0 . The measurements are done thanks to a mechanical two-axis device that is able to rotate in order to

[5]Credits for the data and the plotting to Felix Henningsen and Andreas Gärtner.
[6]Credits for the data and the plotting to Felix Henningsen and Immacolata Carmen Rea.

measure the field of view intensity for several angles. The sensor used is the same SiPM that is included in the POCAM printed circuit board (PCB). The new sphere shows an improvement in the isotropy in relation to the old model. The high sensitivity of the SiPM causes the shift in the symmetry towards 108°. All the components have to be aligned in perfection in order to obtain a symmetric spectrum. To improve the measurement setup, a new system is being developed. This will reduce the systematic uncertainties that are present in the current setup.

4.3 Application in IceCube-Gen2

The POCAM was originally thought as a calibration instrument in the frame of IceCube-Gen2. Nevertheless, its isotropic light emission pattern can help improving the measurements made with the LEDs that the DOMs are equipped with. It can be used for the following tasks:

- Study of the optical impact of refrozen drill holes on DOM sensitivity [44].
- Study of the relative detection efficiency of each individual DOM.
- Study of the reconstructed high energy cascade scale.
- Study the anisotropic scattering strength of the bulk ice [45].

Impact of refrozen drill holes When the Cherenkov radiation is produced, most of is propagation track happens in the bulk ice. However, the photons that the DOM detect have to travel through the refrozen water that filled the drill holes. The optical properties of the hole ice aren't as well understood as those of the bulk ice. This is one of the largest uncertainties concerning the neutrino oscillation measurements in IceCube [46]. How the hole ice affects the detection is being studied by modifying the DOMs angular acceptance curve. Simulations over the photon track using a POCAM with standard IceCube tools are being used to improve the *in-situ* angular acceptance curve measurement.

Relative detection efficiency of DOMs The isotropic emission pattern gives the opportunity of measuring the individual relative efficiency of each DOM. The average detection efficiency of the whole set of DOMs is well known but it is possible that individual DOMs show a deviation from that value by a 10%. This can be caused by fluctuations of the QE of the PMTs and by effects induced by the surrounding ice. This calibration is done with the method of minimum ionizing muons, which is the cause for some of the uncertainties. The optical efficiency of the individual DOMs can be determined to within 3-5%.

Reconstructed high energy cascade scale The technology of POCAM is able to imitate the light signature that high energy cascades leave in the detectors. Due to its calibrated light source the reconstructed energy scale can be tested. It's possible to imitate series of cascades very close in time, as well as the cascade vertex separation power. By testing them, the parameters for the identification of tau neutrino interactions can be improved.

Anisotropic scattering strength of the bulk ice The bulk ice of the Antarctic shows an anisotropic scattering amplitude. This anisotropy seems to be aligned with the ice flow direction. The POCAM can produce isotropic pulses that can help measure this effect. Thus, the study of the scattering can be simplified due to the fact that no initial light emission pattern has to be assumed.

Chapter 5

The analogue circuit board

The analogue circuit is in charge for the production and detection of the light pulses that the POCAM can generate. The final version for the first prototype is composed of four Kapustinsky-like sub-circuits[38] with four different setups. These sub-circuits drive four LEDs, two blue and two green. They can produce individual pulses of $\sim 10\,ns$ and $\mathcal{O}(10^8) - \mathcal{O}(10^{10})\,\gamma$. Besides, other two LEDs are included, one blue and one green. They are driven by the FPGA and can generate longer (20 - 80 ns) and more intense pulses. The board also counts with two different kinds of light detectors: a 9 mm^2 SiPM (PM3325-EB) from KETEK and a 33 mm^2 PIN-Diode from First Sensors (PS33-6b-TO). The charge generated by these two sensors is read out thanks to two charge sensitive amplifiers from CREMAT (CR-110 and CR-113), which are also included in the board. A sketch of the components can be seen in Fig.5.1. The study of the modulation of the pulses, the functioning of the Kapustinsky-like circuit, its characteristics and its evolution will be described in this chapter.

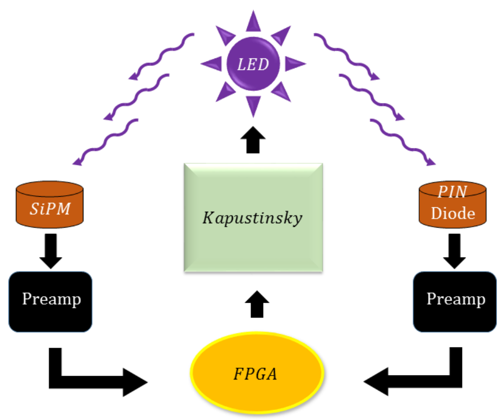

Figure 5.1: *Scheme of the components of the analogue circuit board and its communication with the FPGA.*

5.1 The Kapustinsky circuit

In 1985, J.S. Kapustinsky proposed a circuit whose purpose was being used as a fast timing light pulser for scintillation detectors[38]. The circuit can be seen in Fig. 5.2

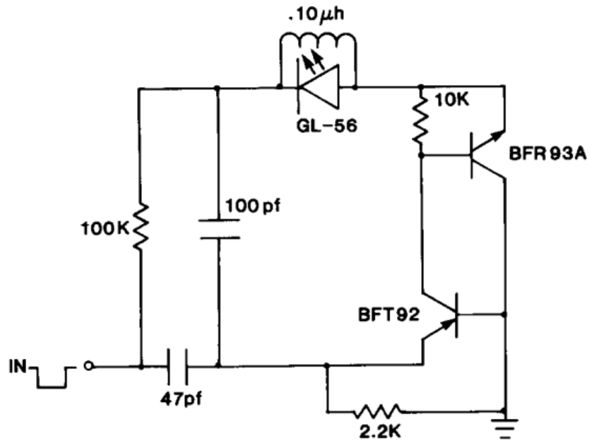

Figure 5.2: *Scheme of the original circuit described by J.S.Kapustinsky[38].*

Kapustinsky's driver has been the base for the LED drivers in the frame of astroparticle experiments since its very own creation[47] [48] [49] [50]. The existence of numerous devices that emit light pulses in the setup for calibration and timing of physics experiments, proves the important of this kind of instruments. Many of them use LEDs as a light source to accomplish their purposes, i.e. the LEDs installed in the DOMs of IceCube. A wide sort of technologies can be used in order to generate fast, bright pulses but this design stands out due to its simplicity and low cost of production. One of its advantages that it is possible to modify the duration and intensity of the light pulse. This can be made by varying the supply voltage, the inductor or by changing the value of the main capacitor and thus, changing the amount of charge available.

5.1.1 Operation

The pulser is based on the fast discharge that a small capacitor can make via a set of two RF transistors that form a thyristor-like element[51]. This construction helps to create a very fast pulse increasing the charge available for the LED to flash. There is an inductor in parallel with the LED forming an LC-circuit. It develops charge opposing himself to the discharging capacitor and thus, reducing the decay constant of the light pulse. The first prototype and its circuit scheme can be seen in the following picture:

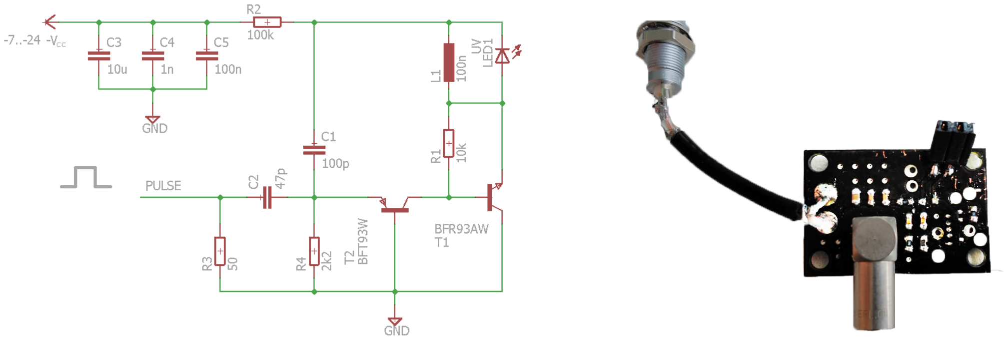

Figure 5.3: *Scheme of the circuit used for the study in the laboratory of the TUM (left). First prototype of the Kapustinsky-like circuit board (right). The connector at the left of the picture is the one used to provide the negative bias $-V_{cc}$.The other connector corresponds to the input of the trigger pulse that activates the circuit.*

An external square pulse is sent to the driver board. It rides on a negative DC bias. A capacitor is charged by the DC component of the trigger pulse. The rising edge of the trigger turns on the transistors which provide a low impedance path in order to dump the charge through the LED. The three capacitors situated after the $-V_{cc}$ input act as a buffer to protect the circuit.

5.1.2 The components

In this part, a brief review on the semiconductors physics behind the basic functioning of the components of Kapustinsky's design is carried out.

5.1.2.1 Bipolar Junction Transistors (BJT)

Transistors are semiconductor devices with the ability to amplify or switch signals and electrical power. BJTs are called bipolar because they work with both charge carriers, electrons e^- and holes h^+. They are made out of two PN-junctions and thus, there are two kinds of BJT possible, PNP and NPN (See Fig. 5.4).

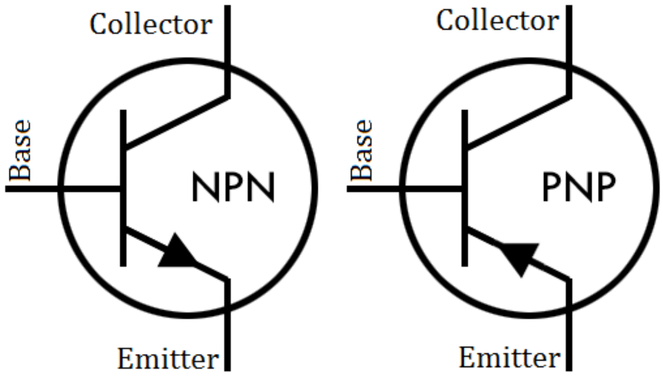

Figure 5.4: *Schematic symbols of BJT.*

The BJT isn't normally a symmetrical device. This lack of symmetry is mainly caused by the doping ratio between emitter and collector.

- **NPN** The base is P-doped, which is surrounded by two N-doped layers. When a positive potential difference is applied between base and emitter, V_{EB}, and there exists also a positive potential difference between the collector and the emitter, V_{EC}, the transistor "turns on" (Notice the scheme on Fig. 5.5). This obtained effect is that a small current coming into the base ends up amplified producing a bigger collector-emitter current. Most of the current is produced by the movement of the electrons between the emitter and the collector as minority carriers in the base. Due to the fact that electron mobility is higher than holes mobility, NPN transistors allow a greater current and operate faster than PNP transistors.

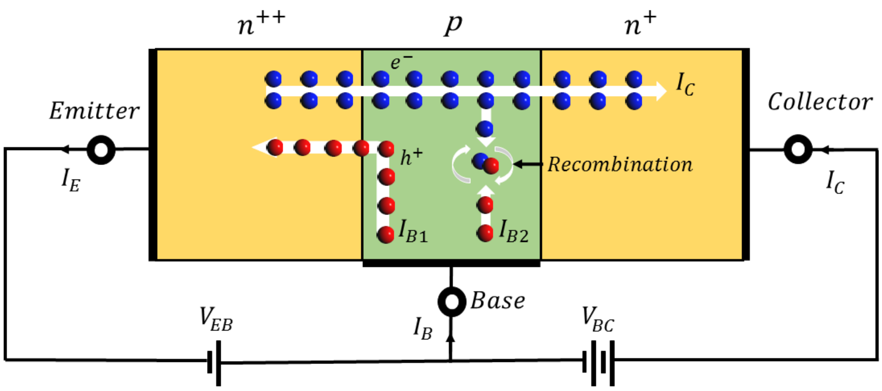

Figure 5.5: *Scheme of how the charge carriers move in a NPN transistor operating in forward active mode. Note that the arrows indicating the current flow follow the conventional current criteria.*

- **PNP** The second kind of BJT is composed by a central layer of N-doped semiconductor between two P-dope layers. The PNP transistor is turned on when $V_{EB} < 0$. The emitter-base region is forward biased, under this situation the holes are injected in the base as minority carriers. As the base layer is very thin, the majority of the holes can cross the reverse-biased base-collector junction reaching the collector region. This way, when a small current leaves the base, it's amplified through the collector output. (Notice the scheme on Fig. 5.6)

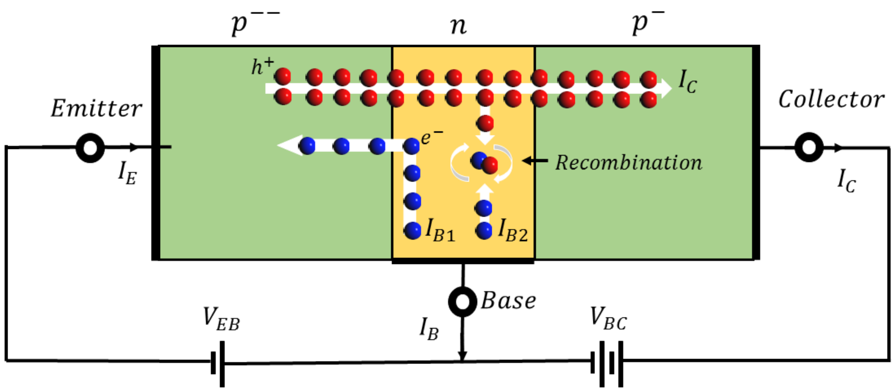

Figure 5.6: *Scheme of how the charge carriers move in a PNP transistor operating in forward active mode.*

Two parameters describe the functioning of the transistors in the different regions that it can operate (α_F and β_F). The common-base current gain (α_F). It is the emitter-collector gain of current when operating in forward-active[52] and is very close to the unit but never reaches it due to the phenomenon of the recombination between electrons and holes in the base.
The common-emitter current gain (β_F). It represent the collector-base current ratio when operating in forward-active mode. ($\beta_F \approx 200 \rightarrow$ low power transistor, $\beta_F \approx 50 \rightarrow$ high power transistor).
Both parameters are related between each other:

$$\alpha_F = \frac{I_\mathrm{C}}{I_\mathrm{E}}, \qquad \beta_F = \frac{I_\mathrm{C}}{I_\mathrm{B}}, \qquad \alpha_F = \frac{\beta_F}{1+\beta_F} \tag{5.1}$$

To be able to understand the functioning of the thyristor, it is important to know the **four modes of operation** that a BJT can have.

- **Forward-active** $I_{CE} >> I_B$ .In this case I_{CE} is almost proportional to I_B. The majority of BJT are build in order to accomplish the biggest collector-emitter current gain in forward-active mode.

- **Reverse-active** Here the emitter and the collectors have exchanged their roles. The gain is way smaller than in forward-active mode.

- **Saturation** When both PN junctions are forward-biased, the BJT enters in saturation. This makes easier the flow of higher current between the emitter and the collector. The BJT acts like a closed switch.
- **Cut-off** This mode is the opposite of saturation, this means that both PN junctions are reverse-biased. There is almost no current flowing between emitter and collector. It would correspond to a closed switch.

When operating in active mode, the behaviour of the current between the three terminals of a BJT is well described by the linear approximation of the Ebers-Moll model.

$$\begin{gathered} I_E = I_{ES}\left(e^{\frac{V_{BE}}{V_T}} - 1\right) \\ I_C = \alpha_F I_E \\ I_B = \left(1 - \alpha_F\right) I_E \end{gathered} \tag{5.2}$$

Where I_E is the emitter current, I_C is the collector current, I_B is the base current and I_{ES} is the reverse saturation base-emitter current . V_{BE} is the base-emitter voltage, V_T is the thermal voltage ($k_B T/q$) and α_F is the common-base forward current gain.

Thyristor

A thyristor consists of a semiconductor device that contains three PN-Junctions. Four layers of alternating N and P-doped material with three terminals. It operates as a bistable switch. A thyristor lets the current flow when the gate is triggered. It keeps conducting unless the device stops being forward-biased. Thyristors are not proportional like transistors, it is to say, they can only be on or off.
The control terminal (gate) corresponds to the layer of P-doped material that is closer to the cathode. It can be modelled as a pair of coupled BJT as seen in Fig. 5.7.

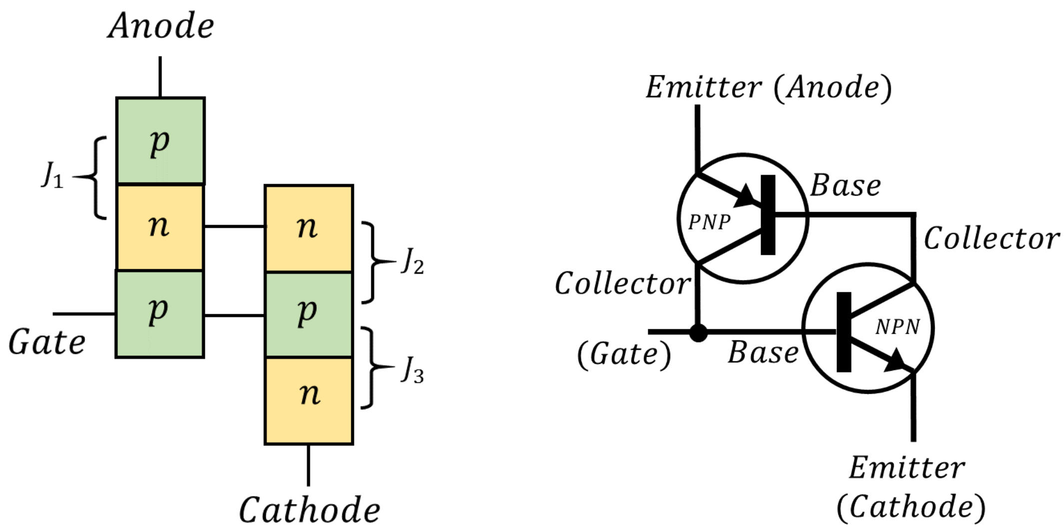

Figure 5.7: *Physical structure of the thyristor at physical level and its equivalent circuit.*

When $V_{AK} > 0$ and V_G=0, J_1 and J_3 are forward biased but J_2 is reverse biased. This situation prevents conduction and therefore, the thyristor remains "off". If V_{AK} surpasses the breakdown voltage V_{BO}, J_2 would enter in avalanche breakdown mode allowing the current to flow and thus, setting the thyristor "on". After the avalanche breakdown has taken place, the thyristor keeps conducting until V_{AK} diminishes under V_{BO} or I_{AK} becomes lower than the holding current I_H. An scheme of the current flow and its dependence on the voltage can bee seen in the following pictures:

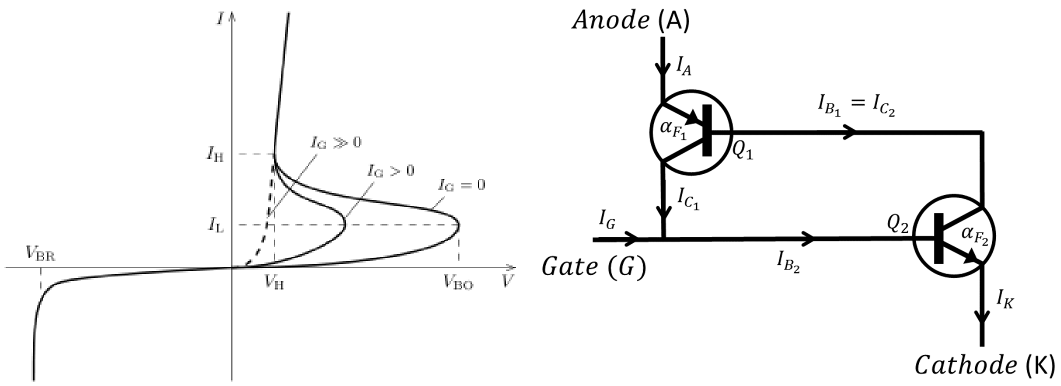

Figure 5.8: *V-I diagram of a thyristor.I_L is the latching current, the current necessary for the thyristor to start conducting (left). Scheme of the current flow in a thyristor using the two transistors model (right)*[53].

The collector current I_C can be related to the emitter current and the collector-base leakage current by

$$I_C = \alpha_F I_E + I_{CB}^L \tag{5.3}$$

For the PNP (Q_1) transistor, $I_E = I_A$, the current of the PNP collector can be written as

$$I_{C1} = \alpha_{F1} I_A + I_{CB_1}^L \tag{5.4}$$

The same applies for the NPN (Q_2) transistor but in this case, $I_E = I_K$

$$I_{C2} = \alpha_{F2} I_K + I_{CB_2}^L \tag{5.5}$$

Summing Eq. 5.4 and Eq. 5.5 we obtain the anode current.

$$I_A = \alpha_{F1} I_A + I_{CB_1}^L + \alpha_{F2} I_K + I_{CB_2}^L \tag{5.6}$$

When the current flows through the gate $I_K = I_A + I_G$. Introducing this in Eq.5.6 we obtain

$$I_A = \frac{\alpha_{F2} I_G + I_{CB_1}^L + I_{CB_2}^L}{1 - (\alpha_{F1} + \alpha_{F2})} \tag{5.7}$$

α_{F1} and α_{F2} depends on $I_{E1} = I_A$ and $I_{E2} = I_K$ respectively. When $I_G > 0$ then, according to Eq. 5.7, I_A will increase. This will make α_{F1} to grow and thus, α_{F2} for $I_{E2} = I_K$ and $I_K = I_A + I_G$. Increasing α_{F1} and α_{F2} causes an increment of I_A known as positive feedback effect. When $\alpha_{F1} + \alpha_{F2} \approx 1$ the denominator of Eq. 5.7 approaches zero and I_A becomes larger turning on the thyristor.

5.2 Light Emission Diode (LED)

A light emission diode is a piece of semiconductor material that has been doped in order to make PN-junction. It emits light when the proper voltage is applied to its leads. It happens thanks to an effect called electroluminescence. This effect can be described as the capacity of a semiconductor to emit photons when is under the influence of an electric field[54].

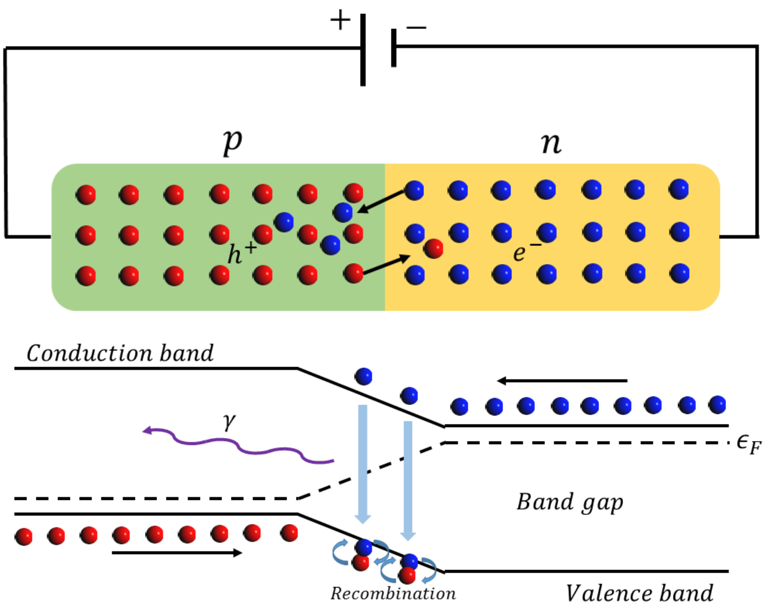

Figure 5.9: *Circuit scheme of a forward-biased LED (up). It is possible to see how electrons and holes move inside the PN-junction towards the opposite pole producing recombination between electrons and holes. Also, the band diagram of the LED shows how electrons recombine with holes passing from the conduction band to the valence band. This phenomenon produces the emission of* γ *whose energy is* $E_\gamma = E_{GAP}$.

After applying a potential difference between both leads, the current flows from the p-side (anode) to the n-side (cathode). Electrons can move through the junction, this way the emission of light begins. When an electron (e^-) and a hole (h^+) meet, they recombine creating an exciton that falls from the conduction band to the valence band (radiative recombination). As the potential difference increases, the luminous intensity rises. This rise is associated to an increase of the current. It can cause an efficiency drop through Auger recombination. This phenomenon is a three-particle interaction in which the energy is transferred to a third carrier. It gets excited to a higher energy level but it doesn't move to a different energy band. The excess of energy is lost to thermal vibrations.
The difference of energy between the conduction band and the valence band is emitted as photons whos energy coincides with the energy width of the GAP. The most typical materials used in the fabrication of LEDs are gallium arsenide ($AsGa$), gallium phosphide (PGa) or gallium phoshor-arsenide (PAsGa).
The colour of the emitted light depend on the band gap energy of the materials that conform the PN-junction. LEDs, in opposition to lasers, do not emit coherent or monochromatic light. They are normally characterised by a narrow spectrum and the angle of emission in which the 90% of the light is emitted.

5.3 Light detection devices

Two devices are installed in the analogue circuit board to measure the photons that the LEDs emit, a 9 mm^2 Silicon Photomultiplier (PM3325-EB) from KETEK[55] and a 33 mm^2 PIN-Photodiode (PS33-6b-TO) from First Light Sensor[56]. The main points in photodetection with semiconductors are:

1. Converting incoming photons into electron-hole pairs.
2. Transporting photocharges to the detection circuit.
3. How big is the influence of dark noise in the measurement of photocharges.

The energy states in a semiconductor are quantised and organised in energy bands. At $T = 0$, all the electrons are bound to their correspondent atomic cores. In this situation no electrons can move and thus, no current is possible (Fig. 5.10) (1). It would take an amount of energy of at least E_{GAP} to swipe an electron from the bound state in the valence band to the conduction band. There exists two different ways to supply this energy. The first is by thermal excitation and the second is by incident photons. When the material has a temperature $T > T_0$, there is always a concentration of charge carriers in the form of electron-hole pairs. The concentration can usually be expressed as proportional to $e^{-\frac{E_{GAP}}{2k_BT}}$. Thermal energy suffices to excite a bound electron making it jump from E_v to E_c. This contributes to the current as a mobile electron. At the same time, a mobile hole is created in the valence band. This situation is illustrated in Fig. 5.10 (2). It represents the main way of dark noise production. Actually, distinguishing between an electron that has been excited by an incident photon from one that has been excited thermally is not possible. If a photon with energy $E_\gamma > E_{GAP}$ hits the material, it is absorbed and an extra electron-hole pair is created as an electron from E_v jumps to E_c Fig. 5.10 (3).

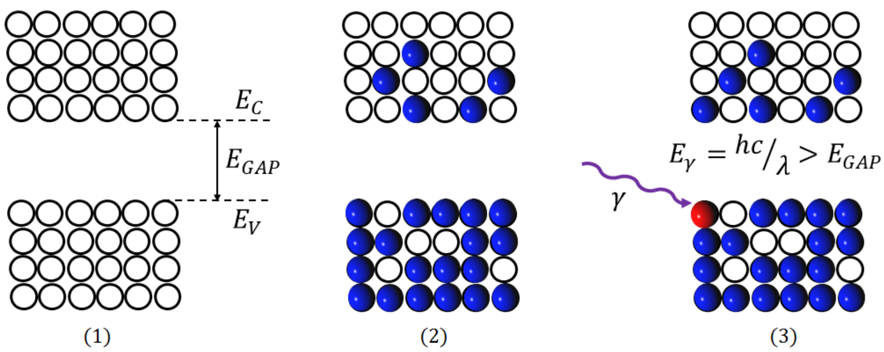

Figure 5.10: *Depiction of the energy band model in a semiconductor and electron-hole pair creation by a photon.*

The main working principles of SiPMs and PIN Photodiodes are sketched in this part.

- **Silicon Photomultiplier (SiPM)**

SiPMs are solid-state, light sensitive devices with the ability to detect single photons. They are composed by an array of silicon avalanche photo diodes operating in Geiger-mode. A Geiger-mode avalanche photo diode is a solid state photo detector. In these devices the material is ionised by a photocharge creating an avalanche current in a reversely biased PN-junction. The difference between the Geiger-mode and the linear mode in APD is that in the first type the device is designed to operate in reverse-bias mode above the breakdown voltage.

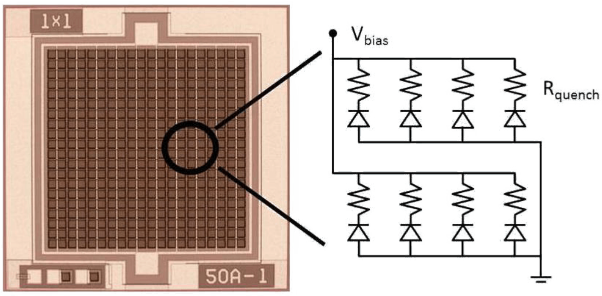

Figure 5.11: *Internal structure of a SiPM[57].*

As seen in Fig. 5.11, all the APDs are connected in parallel to common poles (cathode and anode). This causes the SiPM signal to be the superposition of all APDs signals. The diodes are decoupled from each other with polysilicon quenching resistors. It allows the SiPM microcells to operate above the breakdown voltage. The Geiger operation mode offers a very high signal-to-noise ratio and thus, a good way to detect single photons. The photon detection efficiency (PDE) can be defined as the number of photon-discharged microcells over the number of incident photons, for the SiPM this value depends on the wavelength of the photons and on the overvoltage applied (the dependence of the PDE with respect to the wavelength can be seen in Fig. 5.12). The relationship between gain and breakdown voltage is linear and the quantum efficiency is typically around 80%.

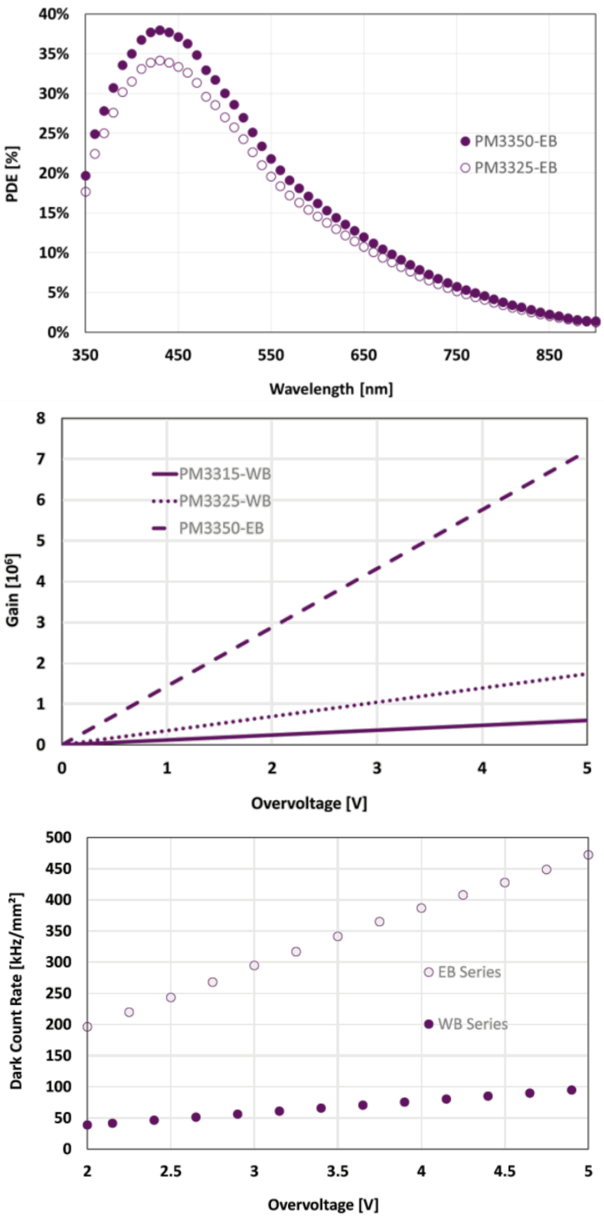

Figure 5.12: *To see in this picture: the absolute photo detection efficiency of the PM3325-EB / PM3350-EB at an overvoltage of 5V (Upper plot), the gain versus overvoltage for three different SiPM with different cell sizes (PM3315-WB (15 µm cells), PM3325-WB (25 µm cells) and PM3350-EB (50 µm cells)), and the dark count rate with respect to the overvoltage applied to the SiPM*[55].

The gain has nothing to envy to PMTs as it is within $10^5 - 10^7$. In Fig. 5.12, the gain for different microcell sizes is shown. The gain is linear with overvoltage and increases with the size of the cell due to the increase of the capacitance of the cells. The timing of Geiger discharge for a singel microcell allows a photon arrival time resolution of $\sim$ 100ps. An advantage in the face of PMTs is that they don't need high voltage but instead only 20-40 V.

A pulse generated without being produced by incoming photons is called dark pulse. These pulses are triggered due to the thermally generated electrons and their frequency is called dark count rate. They depend on the overvoltage (see Fig. 5.12) and on the carrier density in the silicon so, the dark count rate shows a strong temperature dependence.
SiPMs, as PMTs, have a low dependence on temperature though the dependence of the breakdown voltage versus temperature is a necessary study in order to calibrate them properly. Also, the decay time of the signal produce by the incoming photons is proportional to the square root of the excited electrons. Another advantage is the low production costs and the independence of the signal parameters from magnetic field.

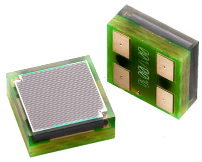

Figure 5.13: *Picture of the 9mm^2 SiPM PM3325-EB from KETEK[57].*

The PM33 Series from Ketek with its 25 μm of microcell size offers a very high photo detection efficiency as well as good timing properties. This together with low dark count rate made it the perfect candidate to accomplish the photo detection for the POCAM[55].

- **PIN Photodiode**

A Pin diode[58] is a three layers structure. As shown in Fig. 5.15, the external layers are p and n-doped materials and an intern layer is made out of an undoped intrinsic semiconductor. The doping of both p-type and n-type regions is very high for they are used as ohmic contacts[58].

Figure 5.14: *Picture of the PIN-Photodiode from First Light Sensor PS33-6b-TO[56].*

In this kind of diode, the depletion zone is practically contained within the i-region. It is way larger than in the typical PN-junction although its size varies very little and does not depend on the reverse bias applied. Due to its characteristics, the space in which electron-hole pairs can be created by an incident photon is bigger.

PIN photodetectors are reverse-biased. In this situation, when a photon with enough energy reaches the depletion zone, a pair electron-hole is created. The electrical field moves the charge carriers out of the i-region generating a current. The quantum efficiency of this devices is typically within 80-90%.

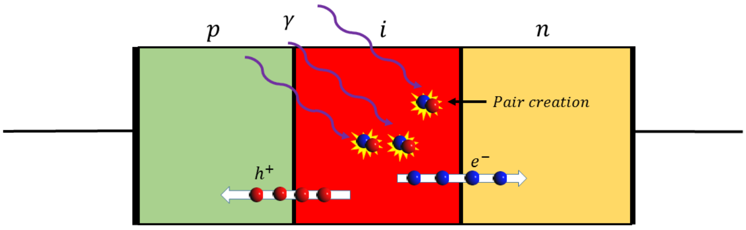

Figure 5.15: *Physical structure of a PIN photodiode and its working principle.*

The analogue circuit counts with the PIN diode PS33-6b TO from First Sensor (a picture of the PIN diode is found in Fig 5.14). Thanks to its 33 mm^2 and its high sensitivity it was the reference value when measuring the LED emission pattern[56]. The QE the dark current of the PS33-6b TO are shown in the following plots:

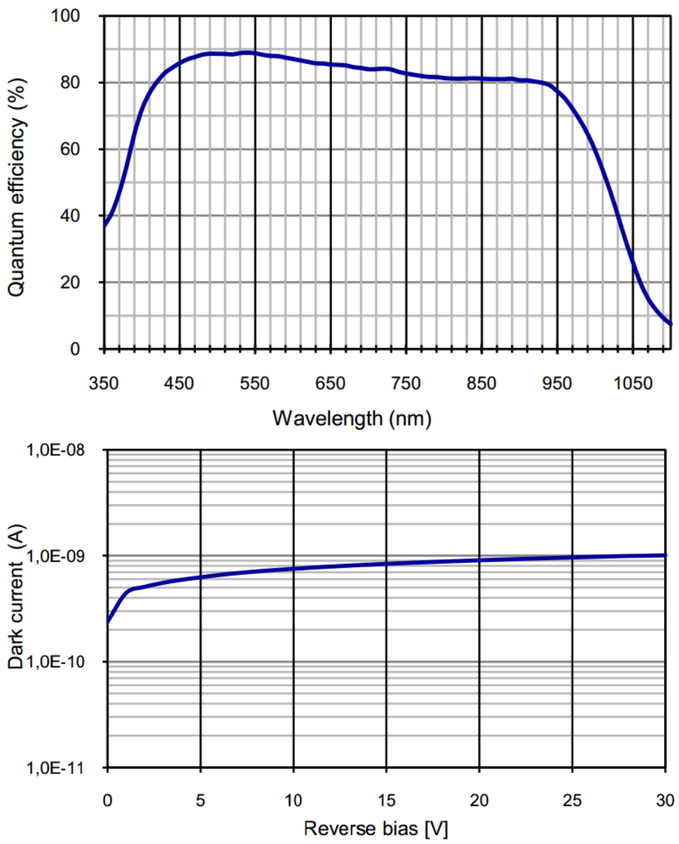

Figure 5.16: *Quantum efficiency of PS33-6b TO at T= 23° C (above). Dark current as fct of bias of PS33-6b TO at T= 23° C (below). As it is possible to see, the PIN-Diode is enhanced for the blue-green wavelength range*[56].

5.4 Preamplifiers

The task of a preamplifier is converting a weak electrical signal into an strong one. They are ideally linear so the gain is constant through the operating range. The high impedance input makes it easier to sense the input signal as a low current is needed. Also, the low output impedance helps boosting the signal strength without affecting the signal-to-noise ratio too much. In this section the charge-preamplifiers will be exposed.

5.4.1 Charge-sensitive preamplifiers

Charge sensitive preamplifiers are useful to detect the total amount of charge coming from a detector that accounts any kind of pulse event. This device integrates the current that flows from the detector over time producing an output proportional to the input charge. This happens thanks to a small capacitance in the feedback loop. A resistor in parallel with the capacitor discharges it slowly allowing the preamplifier output to come back to its original situation. It acts as a charge-to-voltage converter. They are normally made using operational amplifiers. By increasing the output voltage of the amplifier the input current is offset in virtue of the negative feedback current flowing in the capacitor. This way, the voltage that the preamplifier outputs depends on the amount of current in the input that it has to offset and it is inverse to the feedback capacitor value. As the value of the capacitor grows, the output voltage needed to produce the feedback current diminishes. The impedance of the input in this kind of preamplifiers is very close to zero[59].

This devices are more suitable for particle detection because of the nature of the methods used in particle detection. When a particle reaches a detector, the ionization of the detector materials generate an amount of charge that is proportional to the energy of the incoming particle. The preamplifier is required to have a configuration that produces an output proportional to the input charge and thus, to the energy of the incoming particle

.

Ideal circuit

To illustrate how a preamplifier ideally works, Fig. 5.17 is used: a current charges or discharges the feedback capacitor C_f by off-setting the effect of the input current in order to retain the virtual ground at the input. Assuming an ideal operational-amplifier, the v_1 and v_2 nodes are equal making v_2 a virtual ground[52]. The current passing through the resistor can be expressed as:

$$I_{input} = \frac{v_{input}}{R_1} \tag{5.8}$$

It produces a current that flows through the series capacitor in order to keep the virtual ground state. This originates the charging (or discharging) of the capacitor.

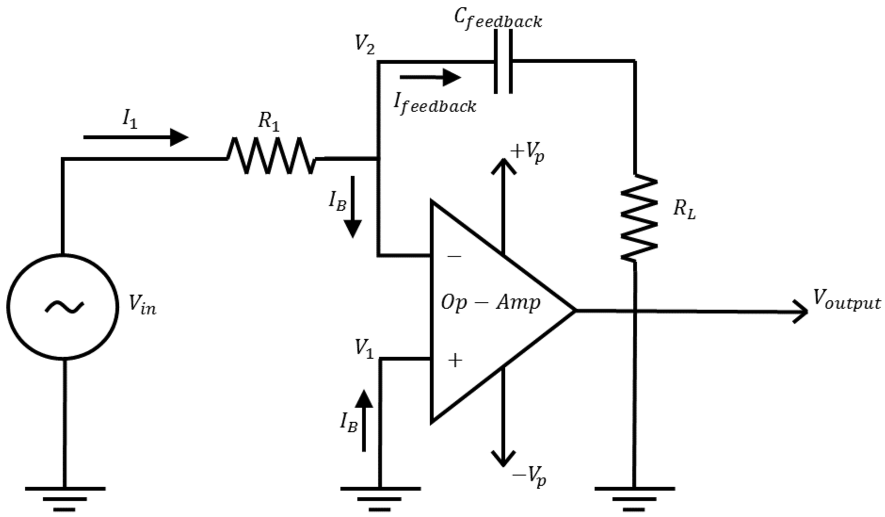

Figure 5.17: *Scheme of the current flow for the ideal circuit model of a charge-sensitive preamplifier.*

Applying Kirchoff's laws to the v_2 node we get:

$$I_1 = I_B + I_{feedback} \tag{5.9}$$

for an ideal operational amplifier $I_B = 0$ so we can write that $I_1 = I_{feedback}$. Moreover, the relationship between current and voltage for the feedback capacitor can be written as:

$$I_C = C_{feedback}\frac{dV_C}{dt} \tag{5.10}$$

Substituting terms and taking into account the ideal operational amplifier case,

$$\frac{v_{in} - v_2}{R_1} = C_{feedback}\frac{d(v_2 - v_0)}{dt} \Rightarrow \frac{v_{in}}{R_1} = -C_{feedback}\frac{dv_o}{dt} \tag{5.11}$$

integrating over time we get the relationship between the output voltage, the feedback capacitor and the input charge:

$$v_0 = -\frac{1}{C_{feedback}}Q \tag{5.12}$$

Assuming an ideal operational amplifier gives rise to some problems as real operational amplifiers have input bias currents, an input offset voltage and a finite gain when there is no feedback in the circuit (finite open-loop gain). In the ideal case, if $v_{in} = 0$ then I_B and the output offset voltage can make that a current pass through the feedback capacitor causing the operational amplifier saturation due to the drift of v_{output}. Given a DC steade state, the capacitor $C_{feedback}$ performs as an open circuit. The operational amplifier acts as a non-ideal op-amp with infinite open-loop gain. To limit the DC gain and bring it to a finite value, a big value resistor $R_{feedback}$ is set in parallel with the capacitor (see Fig. 5.18. It changes the drift from infinite to finite with a small DC error that can be expressed as:

$$V_E = \left(\frac{R_{feedback}}{R_1} + 1\right)\left(V_{IOS} + I_{BI}\left(R_{feedback}||R_1\right)\right) \tag{5.13}$$

$(R_{feedback}||R_1)$ is the sum of two resistances in parallel, the input bias current on the inverting terminal is represented by I_{BI} andV_{IOS} represents the input offset voltage.

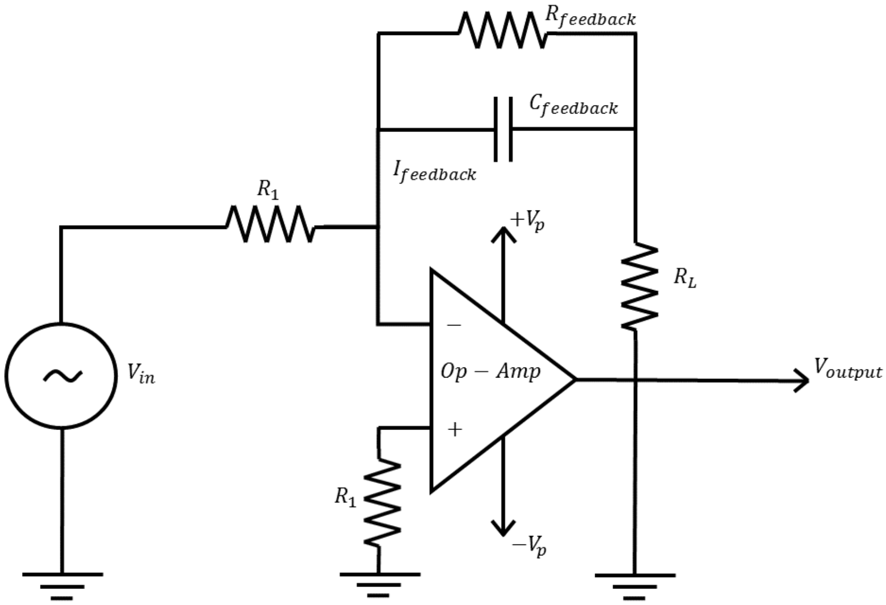

Figure 5.18: *Scheme of the practical circuit for a charge-sensitive preamplifier.*

5.4.2 CR-110 and CR-113 preamplifiers

- **CR-110**

This device is a low noise, single channel, charge-sensitive preamplifier from CREMAT that can be used in DC or AC mode. A representation of how to connect it to make it work in AC mode is found in the next figure:

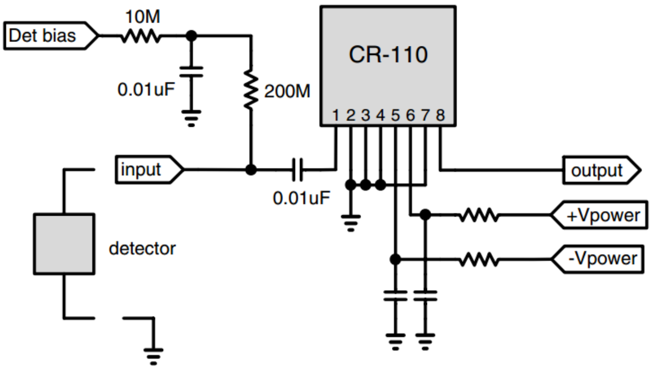

Figure 5.19: *Illustration of the AC mode operation mode used to avoid the DC level of the output signal from saturating. This is recommended if the current exceeds the limit ±10 nA* [60].

It is modelled as a two stage amplifier (see Fig. 5.21) where the first stage provides high gain and the second one low gain. The circuit emphasises the supply of enough current to the output in order to drive the signal properly to the connected measurement device.

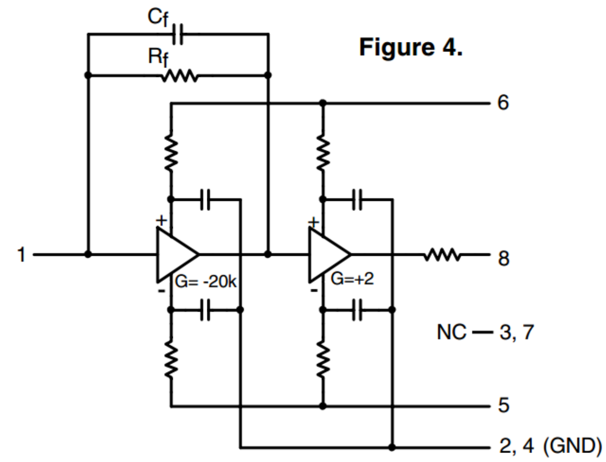

Figure 5.20: *Simplified equivalent circuit of the CR-110. The feedback resistor value is 100 MΩ and the feedback capacity is 1.4 pF* [60]

- **CR-113**

The CR-113 is also a single channel, charge-sensitive preamplifier that differs from CR-110 mainly in the gain. It can be also used in DC or AC mode depending if the detector current exceeds the limit of $\pm 10\ \mu A$. The function of each leg of the preamplifier is provided in the datasheet and can be seen in the following figure:

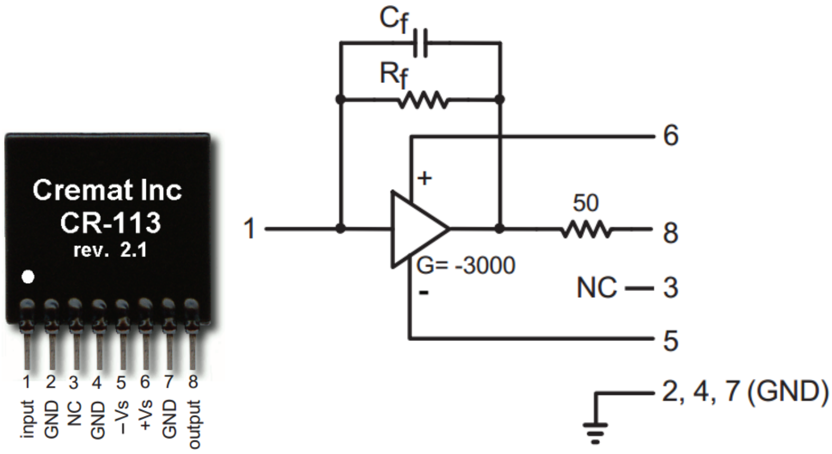

Figure 5.21: *Package and functionality of every leg of the CR-113 (left) and its equivalent circuit diagram (right)*[61]

This preaplifier acts as a single stage amplifier with $R_{feedback} = 68$ kΩ and $C_{feedback} = 750$ pF. When radiation is detected, the pulses produce short bursts of current that flow through the preamplifier creating a signal proportional to the charge.

Chapter 6

Study of the LED driver circuit

As already seen in the previous Chapter, the core of the analogue circuit board is a simple flasher circuit that Kapustinsky purposed in 1985. The evolution of its study as well as the characteristics and emission profile of the LEDs tested will be extended in this chapter. Thanks to simulations and laboratory work, how to modulate the light pulse and how to improve its measurement was learned giving rise to individual pulses of $\sim$ 10 ns and $\mathcal{O}(10^8) \sim \mathcal{O}(10^9)\gamma$. Different wavelength LEDs were tested in order to fulfil the optical characteristics of the first in-situ test of the POCAM at lake Baikal.

6.1 LED driver: Kapustinsky circuit

The pulser is based on the fast discharge that a small capacitor C_1 can make via a set of two RF transistors that form a thyristor-like element [51] (see scheme of Fig.6.1). The voltage variation produced by the rising edge of a positive square pulse charges a small capacitor C_2. This produces the fast voltage shock that turns the transistors "on" allowing the current to flow. When the breakdown voltage of the thyristor-like element is reached, the available charge for the LED increases very rapidly creating a pulse that flashes it. The LED has an inductor in parallel forming an LC-circuit, it develops charge opposing himself to the discharging capacitor and thus, reducing the decay constant of the light pulse. The thyristor keeps being "on" and therefore, building charge for the LED while the gate current I_G is big enough. The thyristor turns itself "off" when $I_G < I_{Latching}$ avoiding any charge to flow.

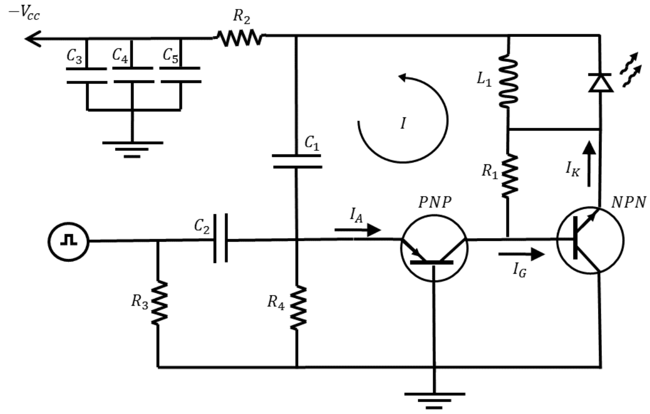

Figure 6.1: *Flasher circuit scheme. When $V_{AK} > V_{BO}$ the current starts flowing through the transistors fed by the main capacitor C_1. I_K grows rapidly powering the LED. The inductor in parallel shortens the tail of the light pulse by opposing himself to any change in the amount of charge that the LED can accumulate.*

A buffer to protect the circuit is formed by C_3,C_4 and C_5. Resistors R_{1-4} provide whether the proper impedance for the external incoming trigger pulse or help determine the path for the current to flow or not.

6.1.1 PSpice simulation

As a first approach to study how the flasher changes its response was carried out using the software OrCAD PSpice Designer. It was accomplished by changing the capacity of C_1, the inductance of L_1 or the negative bias voltage.

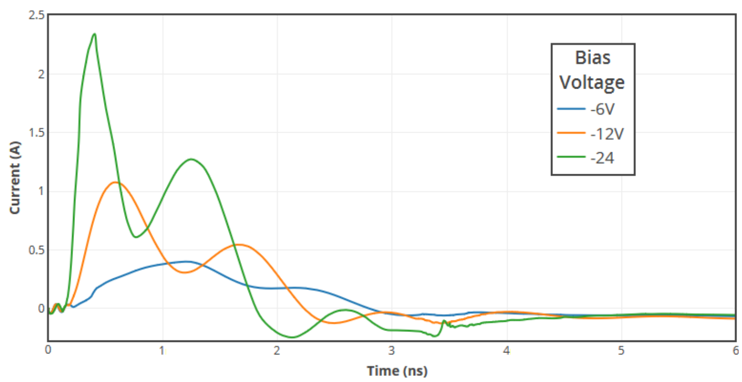

Figure 6.2: *Simulation of the circuit of Fig. 6.1. The depicted results are obtained by variating the negative bias voltage in three stages -6V, -12V and -24V while keeping all the other key values fixed ($C_1 = 100pF$, $L_1 = 100nH$).*

As it is possible to notice in Fig. 6.2, the pulse broadens and lowers as the bias voltage is reduced. The amount of charge available as well as the duration of the pulse can be modulated by changing the bias voltage.

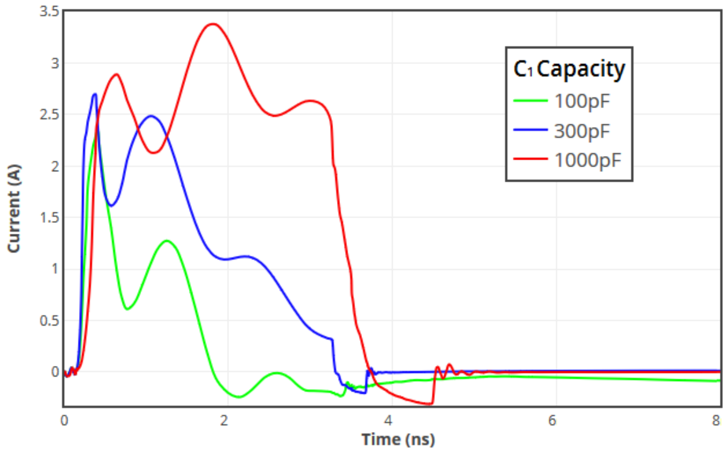

Figure 6.3: *Simulation of the circuit of Fig. 6.1. The depicted results are obtained by variating the capacity of C_1 in three stages 100 pF, 300 pF and 1000 pF while keeping the inductance ($L_1 = 100nH$) and the bias voltage ($V_{cc} = -24V$) fixed.*

Increasing the capacity of C_1 increases the amount of charge that can flow through the transistors building up a longer pulse. In Fig. 6.3 the pulses show different peaks that increase as the capacity raises. This can be the result of the feedback current of the thyristor that makes it easier for the charge to flow as the gate current increases.

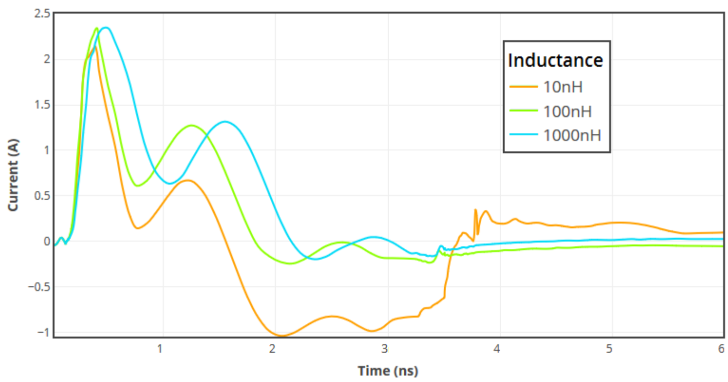

Figure 6.4: *Simulation of the circuit of Fig. 6.1. The depicted results are obtained by variating the inductance L_1 in three stages 10 nH, 100 nH and 1000 nH while keeping the capacity of C_1 ($C_1 = 100pF$) and the bias voltage ($V_{cc} = -24V$) fixed.*

The pulse is slightly lowered with decreasing values of L_1 but the most significant effect is the shortening of the pulse. An odd valley is to be noticed in Fig. 6.4 in the pulse generated for $L_1 = 10$ nH. It looks as if the circuit were drawing back charge after producing the pulse. After checking experimentally, it is possible to affirm that this effect is produced by the simulation.

6.1.2 Evolution

The circuit was at first tested on a protoboard to give way to the first PCB design, shown in Fig. 6.5. It was a 21,56 x 31,75 mm, 1 layer PCB with space for the trigger input, the V_{cc} input and leaded LEDs.

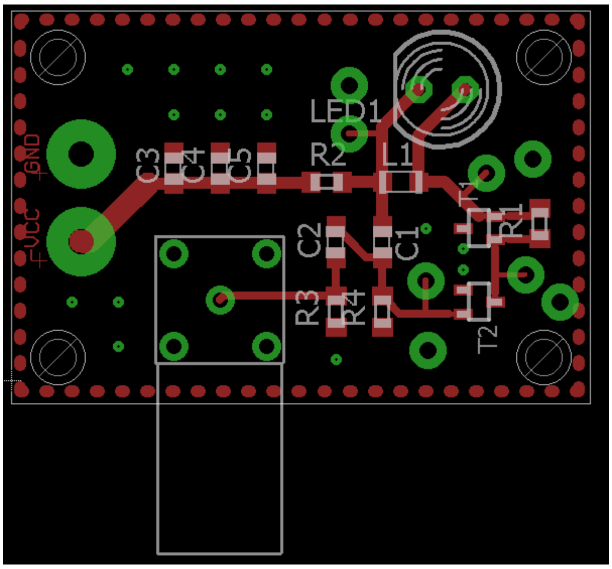

Figure 6.5: *Layout of the first PCB prototype used to measure the properties of the flasher with leaded LEDs. Most of the components package is 0603 with the exception of the PNP (BFT93W) and the NPN (BFR93AW) transistors which is SOT323*

After testing the first LEDs and starting to dig in the functioning of the flasher, the need to test new LEDs and to reduce the inductance of the circuit gave way to a second PCB prototype. This second version was a 22,60 x 21,70 mm 2 layers PCB with two input connectors (for the trigger and the V_{cc}) and had enough space for three different LEDs with different packaging. The LED driver circuit was in the centre of the PCB as it can be noticed in Fig. 6.6.

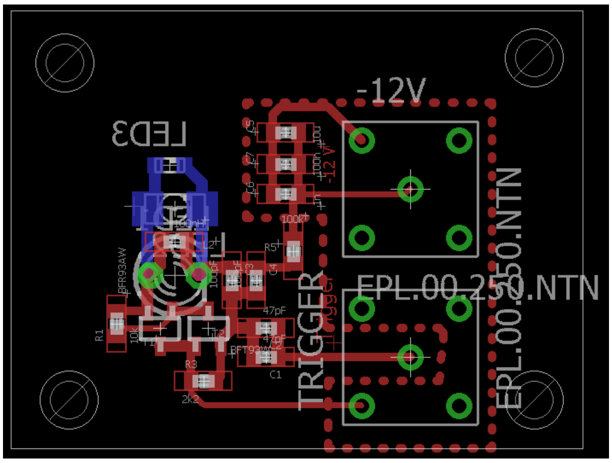

Figure 6.6: *Layout of the second PCB prototype used to test the emission profile of different SMD LEDs. Most of the components package is 0402 with the exception of the PNP (BFT93W) and the NPN (BFR93AW) transistors which is SOT323*

The second PCB included two sets of two capacitors in the place of C_1 and C_2. This made easier to manipulate the amount of charge available for the flasher. It also made it easier in order to understand how it would affect the light pulses. Three different Surface-Mount-Device (SMD) LEDs footprints are included to increase the possibility of testing several kinds of LEDs with the same PCB. The decision of shrinking the circuit and using SMD LEDs pursued the reduction of the inductance inherent to the circuit. This inductance is due to the length of the lines connecting the components so using SMD LEDs supposes a significant reduction.

A third PCB version was intended to include the triggering circuit from Fig.6.15 in section 6.2 . It would also include two connectors. One connector to provide the trigger circuit and a second one to provide the negative bias voltage that the flasher needs. As it was decided that the FPGA would trigger the LED driver, this PCB version wasn't developed. The POCAM is intended to provide multi wavelength light pulses with different duration and photon output. To accomplish this task, a flasher with the possibility of channel selection or a PCB with several flashers was needed (see Fig. 6.7).

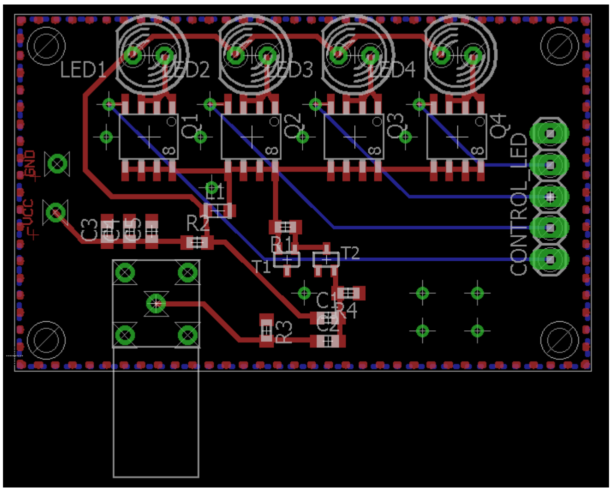

Figure 6.7: *Layout of the third PCB prototype used to test the possibility of emitting different pulses with different wavelengths.*

The above shown PCB is equipped with four junction field-effect transistors (JFET) that operate as switches in order to produce pulses with different wavelength. The JFET would be controlled by an Arduino board. The main problem from using JFETs and an Arduino to control the circuit output was the speed. The JFET slows down the fast rising pulse generated by the thyristor. Also the Arduino can't provide signals faster than 1 ms which is way too slow to control the pulsing of the flasher. Thus, this design was discarded and four independent flashers with four different $C_1 - L_1$ configurations like the one from Fig.6.6 were used in the analogue circuit board. The LED footprint included in the last version of the flasher is a self-designed footprint intended to be used with most of the SMD LED packaging.

6.2 Trigger circuit

The flasher needs to be triggered by a square pulse. Following the steps of Kapustinsky's paper[38], the prototypes were triggered using a frequency generator module in the laboratory. A 3.5 V positive square pulse of around 50 ns with a fast rising time was used for this purpose, as shown in Fig.6.8.

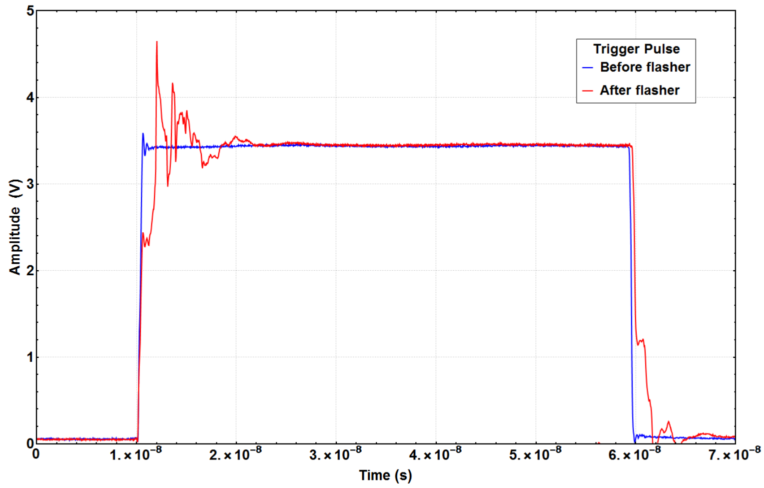

Figure 6.8: *Comparison of the trigger pulse after and before being plugged in the flasher circuit. To see is a little disturbance after rising in the trigger pulse when connected to the flasher circuit. This is due to the switching of the transistors.*

For practical reasons, a way to trigger the flasher needed to be included in the POCAM. Although finally the FPGA was chosen to trigger the flasher, different ways to include a trigger circuit able to produce a positive square pulse were studied.

6.2.1 The 555 timer

The first option taken into account was the 555 timer integrated circuit. The 555 timer IC is an 8-pins IC that can be used to generate tie delays or as a flip flop.

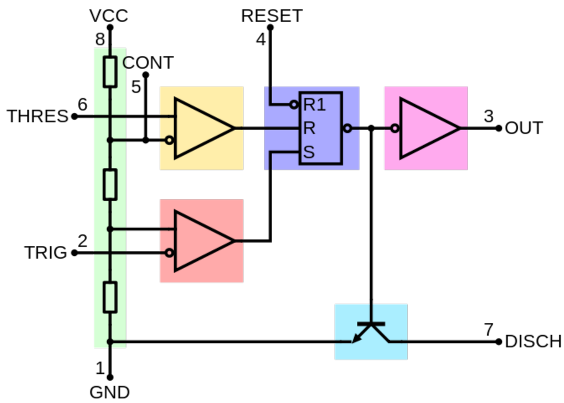

Figure 6.9: *Internal block diagram of the 555 timer IC*[62].

A voltage divider consisting in three 5 kΩ resistors creates two reference voltages between the positive supply voltage V_{cc} and ground. This references are set at $1/3V_{cc}$ and $2/3V_{cc}$. The last reference voltage is connected to the pin named "control voltage". A comparator is connected to the $2/3V_{cc}$ reference by the negative input leaving the positive input connected to the threshold pin. A second comparator has its positive input connected to the $1/3V_{cc}$ reference voltage with the negative one connected to the trigger pin. To store the state of the timer an SR flip-flop is included. The comparators are in charge of controlling it. The reset pin can override the inputs resetting the timer at will. The flip-flop is connected to an output stage with push-pull output drivers. It can provide the output pin with enough current (typically 200 mA although it varies with the model). The flip-flop is also connected to a transistor that allows the discharging of the whole circuit through the ground pin[63]. It can be configured in three different modes, astable, monostable or bistable. We are interested in the astable mode.

Astable configuration of the 555 timer IC

In this mode, the 555 generates a trail of positive rectangular pulses with a specific frequency depending on the values of the reference capacitor and a couple of resistors that act as a voltage divider (see Fig. 6.11).

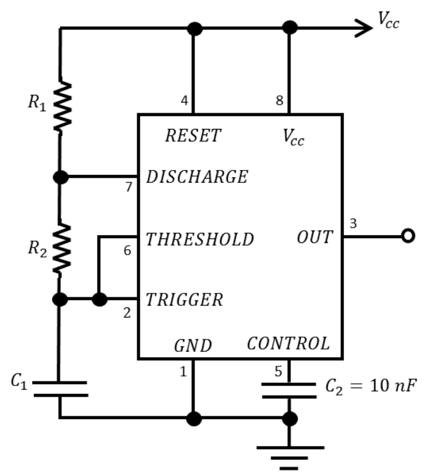

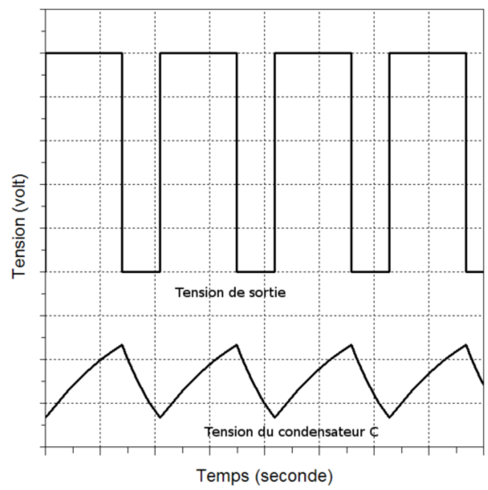

Figure 6.10: *Scheme of a 555 in astable mode (left). Waveform produced in astable mode (right)[62].*

In astable configuration, the time in which the output is high is determined by the total resistance and the value of the reference capacitor C_1, acording to the formula :

$$t_H = ln(2)\,(R_1 + R_2)\,C_1 \tag{6.1}$$

In turn, the duration of time in which the output is low can be written in terms of R_2 and C_1 :

$$t_L = ln(2)R_2C_1 \tag{6.2}$$

The period of the waveform is the sum of t_H and t_L, and the frequency is the inverse of the period:

$$T = t_H + t_L = ln(2)\,(R_1 + 2R_2)C_1(6.3)$$

$$f = \frac{1}{T} = \frac{1}{ln(2)\,(R_1 + 2R_2)C_1(6.4)}$$

The duty cycle (the ratio between pulse duration and period) has a minimum of $d = 0.5$. This means that the limit in the ratio $\frac{t_L}{t_H} = 1$ as $t_H \geq t_L$ for any value of R_1, R_2 and C_1. This limit can be modified by including a diode in parallel with R_2 between the discharge and the threshold pins. The scheme and the waveform produced can be seen in the following figure:

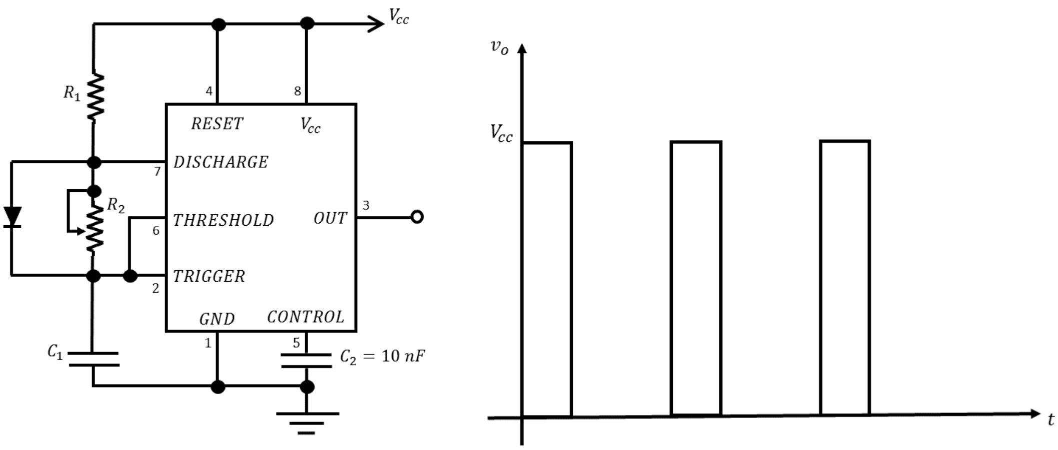

Figure 6.11: *Scheme of a 555 in astable mode with forward biased diode between pins 7 and 6 (left). Waveform produced (right)*[62].

When the output is in high state, the forward biased diode shorts out R_2. Thus, the time duration of the high state is:

$$t_H = ln(2)R_1C_1 \tag{6.5}$$

When the output is low state, the diode is unbiased. In this situation it behaves like an open circuit, hence:

$$t_L = ln(2)R_2C_1 \tag{6.6}$$

The period, frequency and duty cycle are:

$$T = ln(2)(R_1 + R_2)C_1 \tag{6.7}$$

$$f = \frac{1}{ln(2)(R_1 + R_2)C_1} \tag{6.8}$$

$$d = \frac{t_H}{T} = \frac{ln(2)R_1C_1}{ln(2)(R_1 + R_2)C_1} = \frac{R_1}{R_1 + R_2} \tag{6.9}$$

To achieve a duty cycle smaller than 50% R_2 has to be bigger than R_1. To variate the duty cycle a potentiometer can be set to replace the fix value of the resistor R_2.
The pulse produced with different 555 ICs in astable mode with a duty cycle lower than 50% was easy to set up at will. Nevertheless, as seen in Fig. 6.12, the rising time of the positive square pulse approached the 40 ns in the best case so, despite of its low power consumption this option had to be discarded.

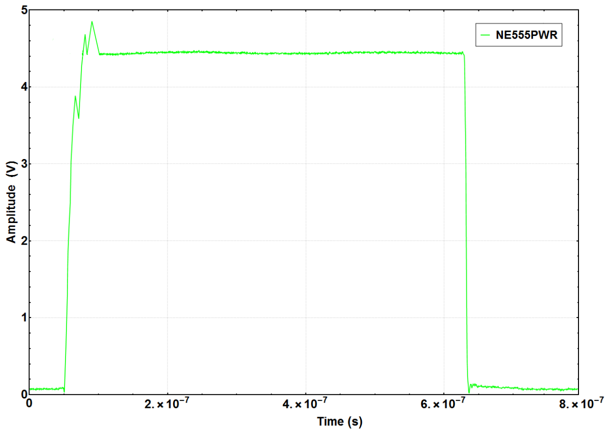

Figure 6.12: *Square pulse generated by the NE555PWR working in astable mode with a diode biasing the resistor between the discharge and the threshold pin.*

6.2.2 555 Timer plus Schmitt trigger

The Schmitt trigger is an electronic device that works as a comparator. It is usually used to reduce noise and disturbances or as a analogue-to-digital converter. It is called trigger due to the fact that the output keeps its value until the input is changed enough to produce a change. It has two thresholds at different voltage levels. The effect of the dual threshold is called hysteresis and means that this device acts as if it had memory. The idea behind the hysteresis is the application of positive feedback to the input. This is made by adding a part of the output signal to the input making it go through an attenuator and then by a summer [52]. In the diagram below the logic of the Schmitt trigger is depicted.

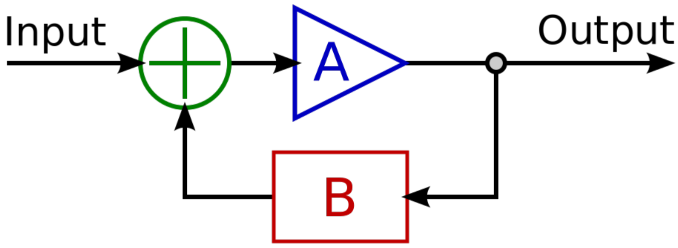

Figure 6.13: *Schmitt trigger's block diagram. To see is the attenuator (B) and the summer (+). A positive feedback is inserted from the output to the input. This causes the fast switching between saturated states of A as the input crosses a certain threshold provided by a comparator (A)*[64].

Thanks to this, it can act as a flip-flop. The Schmitt trigger can be used in non-inverting or inverting mode. We care about the inverting mode as it was used together with the 555 timer

Inverting Schmitt trigger

In this mode, the attenuator and the summer act separated.

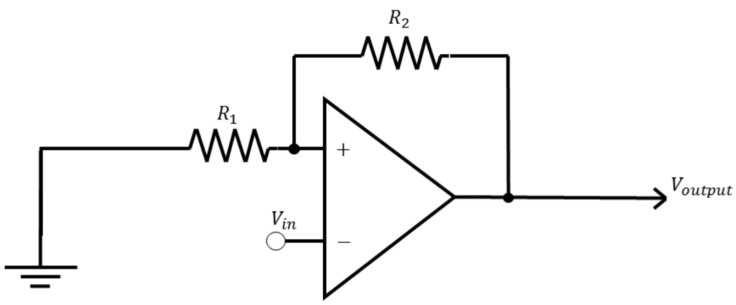

Figure 6.14: *Scheme of the inverting mode of the Schmitt trigger.*

As seen in Fig. 6.14, both resistors act as a voltage divider providing the attenuation. The input loop adds a portion of the output signal to the input. Thanks to this, hysteresis is achieved and is modulated by the ratio $\frac{R_1}{(R_1+R_2)}$. As the voltage applied to the operational amplifier is floating, it must have a differential input.
When the Schmitt trigger is in high state, the output will be at the plus power supply rail ($+V_s$) and the output voltage provided by the attenuator will be $V_+ = \frac{R_1}{(R_1+R_2)}V_s$.
In this situation the comparator switches if $V_{in} = V_+$. To reach it V_{in} has to be above the threshold. As a consequence it is able to change the output. When the comparator switches to $-V_s$, the threshold inverts its sign being then $V_- = -\frac{R_1}{(R_1+R_2)}V_s$ and switches back to high state. This means that the it acts as a double comparator centered in zero with triggering at $\pm\frac{R_1}{(R_1+R_2)}V_s$.

Trigger circuit

As previously seen in the subsection of the 555 astable mode, the simplest configuration of the 555 timer can offer a minimum duty cycle of 50%. By inverting the signal with a Schmitt trigger the t_L and t_H provided by the 555 timer invert their roles. This means that it is possible to control the separation between square pulses and it is easier to modulate how long the signal stays in high state. Another advantage is that it filters most of the jiggling that could be introduced in the circuit and has a faster rising time than the 555 timer. The schematic version of the trigger circuit designed for the LED flasher board is shown below:

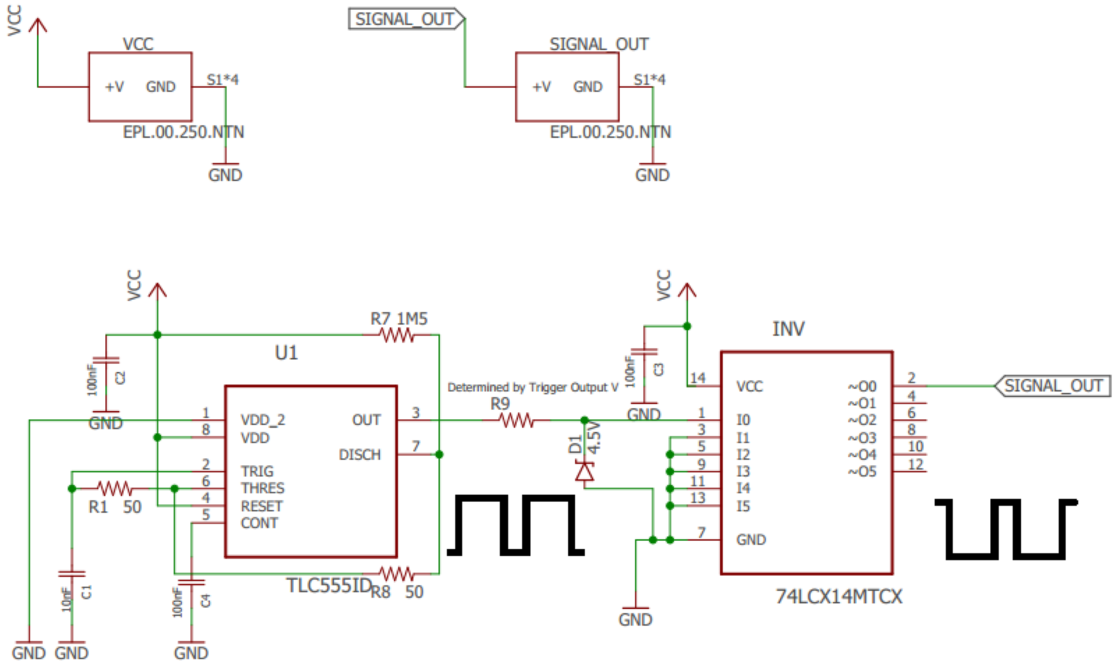

Figure 6.15: *Scheme of the circuit generator of positive square pulses used to trigger the LED flasher.*

The combination of both provides a fast rising, stable positive square pulse with low power consumption. The voltage and current output depend on the characteristics of the ICs used. A Zener diode and a resistor are set between the timer and the inverter to protect the inverter in case the signal generated by the 555 timer could damage it.

The performance and size of the circuit suited the requirements of the flasher and the POCAM. Nevertheless, it was finally decided, that the FPGA would trigger the flasher for the sake of simplicity.

6.3 Experimental set up

To perform the experimental study of the flasher board, as well as the LED light pulses profile, an isolating box was constructed. The manufacturing was carried out by the workshop of the physic's faculty in Garching Forschungszentrum. Its main function is to shield the photosensors from unwanted external photon sources that could affect the measurements and thus, the calibration of the whole system.

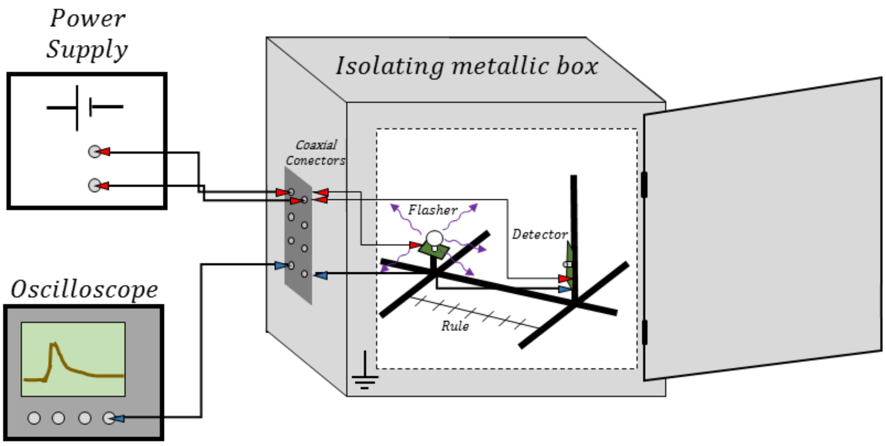

Figure 6.16: *Sketch of the experimental set up.*

The elements included in the above picture as well as the connection between them (see Fig.6.17) are described in the following paragraphs:

- **The isolating box** It is made of metal and its walls are cover on the inside with foam and black fabric. The lining helps avoiding reflections on the internal sides of the hexahedron. This reflections can interfere in the calculation of the emitted amount of photons. The reflected photons arrive with a certain delay to the detector causing the output signal to change by accounting the reflected photons as photons emitted originally in the direction of the photo sensor. Several coaxial connectors are mounted on one side of the metallic box to connect the inner circuits with the scope and the power supply. The fact that the box is made out of metal helps creating a common ground to the whole system.

- **Power supply** The variable DC power supply provides the necessary different of potential to power up every component: the trigger circuit, the negative bias voltage of the flasher board and the photo sensors.

- **Internal structure** A metallic black structure is assembled inside the box to provide physical support. A rule parallel to the long axis assist the measurement of the horizontal distance between the light source and the detector. Also the height of the detector and the center of the integrating sphere is taken with the help of a measuring tape.

- **Photo sensors** The S5972 photodiode from Hamamatsu with 0.5 mm^2 of detecting surface was used in first place. After computing the amount of detected photons per pulse, it was decided to use a PIN diode with a bigger sensitive surface. The PIN diode PS33-6b-TO from First Sensor was chosen due to its bigger detecting surface ($33mm^2$) and its price.
  The decision of using a second photo sensor, more sensitive than a PIN diode, was taken in order to improve the accuracy of the measurements and ensure the functioning of the POCAM in case one photo sensor cease working when deployed. The SiPM (PM66) and the PIN diode are used alternatively for every set of measurements. Every photo sensor feeds a signal to its own charge-sensitive preamplifier. The PIN Diode uses the CR-110 to amplify the signal produced by the flasher. The other preamplifier (CR-113) is associated to the SiPM. After amplifying the signal, this is driven to the oscilloscope to be stored and processed if necessary.

- **Flasher** PCBs with different inductances and capacitor values were used to produce different pulses.

- **Oscilloscope** The software of the oscilloscope helps saving the data in different formats for its future study. It also provides real time information about the rising time, amplitude and full width at half maximum (FWHM) of the displayed signal.

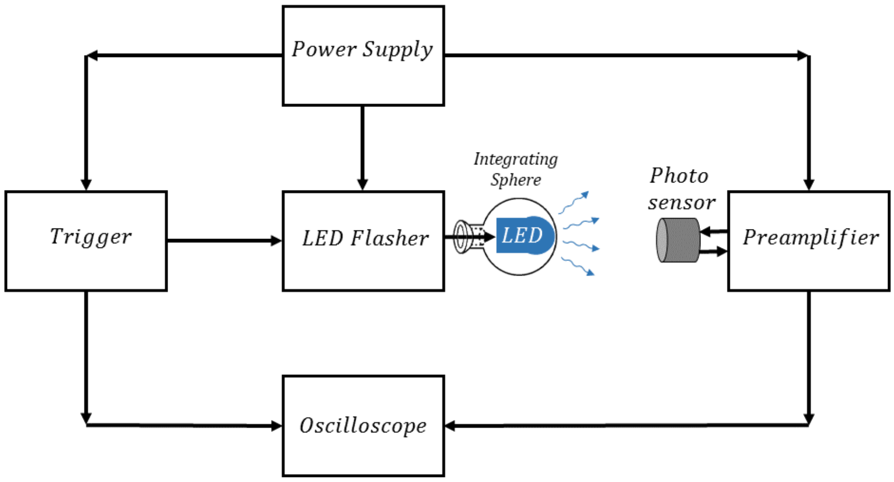

Figure 6.17: *Scheme of the connection between the elements of the experimental set up.*

6.3.1 Study about the pulse produced by the flasher.

The study of the characteristics of the pulse produced by the flasher circuit and how to modulate it was carried out using the experimental set up shown in Fig. 6.16. An integrating sphere made of PTFE and composed of two half spheres joined by the equator was used. The sphere has an outer diameter of 50 mm and the PTFE thickness is 1 mm. The photon detection device used was the S5972 photodiode from Hamamatsu with 0.5 mm^2 of detecting surface. Assuming perfect isotropy of the light emitted by the integrating sphere, the light source can be taken as coming from the centre of it. The photodiode was placed on the external surface of the PTFE sphere close to the equator. The difference of voltage provided by the photodiode goes through a non-integrating amplifier and then to the oscilloscope where the information is recorded and analysed. The behaviour of the flasher was studied varying the following elements.

- **Bias voltage** V_{cc} Three different voltages were applied, -6 V, -12 V, and -24V.
- **Charge available in the circuit** Three different values of the main capacitor C_1 were used: 100 pF, 200 pF, and 1 nF.
- **Effect of the inductance** Different inductances were used to account for the variation of the tale of the pulse: 11 nH, 22 nH, 50 nH, 100 nH, 319 nH, 470, nH, 1000 nH and no inductance at all, represented by inf nH).

LED	λ_{min} (nm)	λ_{typ}(nm)	λ_{max}(nm)	Viewing Angle (Â°)	Type
Bivar UV5TZ-405-15	402.5	405	407.5	30	Leaded
Nichia NCSU276AT-U385	380	385	390	60	Leaded
ProLight-PM2L-3LLE-SD	400	402.5	405	130	SMD
TSLC SLLP-F586-1520-UV	390	[1]	425	30	Leaded

Table 6.1: *LEDs used for the first tests with the PCB shown in Fig. 6.5.*

6.3.2 LED selection for the POCAM

Using the experimental set up depicted in Fig. 6.16 a set of 7 different SMD LEDs was measured. Two different PCBs were used to produce a long pulse and a short pulse:

- **Long pulse:** V_{cc}=-12 V, C_1 = 1 nF, C_2 = 470 pF, L_1 = 100 nH.
- **Short pulse:** V_{cc}=-12 V, C_1 = 1 nF, C_2 = 470 pF, L_1 = 22 nH.

A PTFE integrating sphere with an outer diameter of 50 mm and 1 mm thickness was used. Two different detection devices were utilised:

- PIN Diode (PS33-6b-TO) from First Sensor with 33 mm^2 of sensitive surface.
- SiPM (PM66) from Ketek with 36 mm^2 of sensitive surface.

The signal provided by the PIN diode was amplified with the charge sensitive preamplifier CR-110 from CREMAT. For its part, the SiPM was connected to a different model, the CR-113, also from CREMAT. The signals were acquired, stored and analysed with the help of the oscilloscope.
Due to the difference of sensitivity and quantum efficiency of the devices, different distances were chosen for each detector and configuration:

- **Long pulse:** d_{PD} = 52.3 mm, d_{SiPM} = 800 mm
- **Short pulse:** d_{PD} = 52.3 mm, d_{SiPM} = 80 mm

The distance is referenced to the centre of the integrating sphere to the sensitive surface of the detector. The current generated by both detectors was transformed into a difference of potential by the preamplifiers. The registered maximum voltage is the data used to compute the photon output. This is so because the registered voltage and the photon output are linearly related. The reference values used were those obtained with the PIN

[1]Not provided in the data sheet.

diode due to the lack of a better calibration of the SiPM. To measure the duration of the pulse, the decay time of the signal provided by the SiPM without preamplifier was used. The following LEDs were tested:

LED	λ_{min} (nm)	λ_{typ}(nm)	λ_{max}(nm)	Viewing Angle (Â°)	Type
LZ1-00B200	[2]	455	[2]	80	SMD
LZ1-00G102-0000	[2]	530	[2]	100	SMD
ALMD-CB3D-SU002	460	470	480	60	SMD
ALMD-CM3D-XZ002	519	525	539	60	SMD
XPEBRY-L1-0000-00S01	450	457.5	465	135	SMD
XPEBGR-L1-0000-00A01	520	527.5	535	135	SMD
XPEBGR-L1-0000-00F01	520	527.5	535	135	SMD

Table 6.2: *Final selection of LEDs tested to be included in the first prototype of the POCAM.*

6.4 Calibration of the PIN diode

A reverse-biased PIN diode produces a current when is illuminated. This current is proportional to the amount of photons hitting the intrinsic material. This current is then sent to a charge-sensitive preamplifier that transforms proportionally the current into a difference of potential. The result is a pulse whose amplitude (in volts) is linearly proportional to the amount of photons interacting with the photodiode. A scheme of system involved in the detection of the photons produced by the flasher can be seen below:

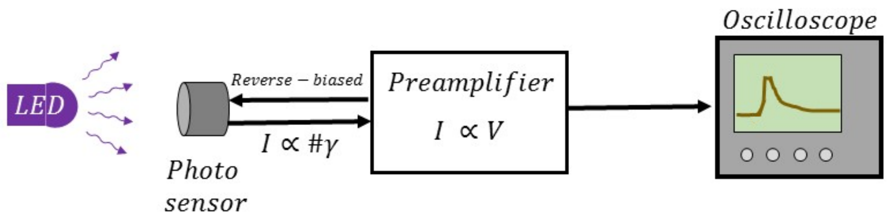

Figure 6.18: *Scheme of the flasher-detector system.*

To figure out the constant of proportionality it is necessary first to calibrate the system PIN diode-preamplifier. For this task, a signal is sent through a reference capacitor to the preamplifier and then acquired by the oscilloscope. A signal generator produces a variable difference of voltage in the form of a positive square pulse of 1V of amplitude and

[2]Not specified in the data sheet

100 ns wide. The pulse charges the capacitor pushing the electrons out of it and thus, generating a current proportional to incoming signal. The outcoming current interacts with the charge-sensitive preamplifier generating a variable difference of voltage. The amplitude of this final pulse is related to the amount of electrons produced by the original square pulse. The schematic setup can be seen in the following figure:

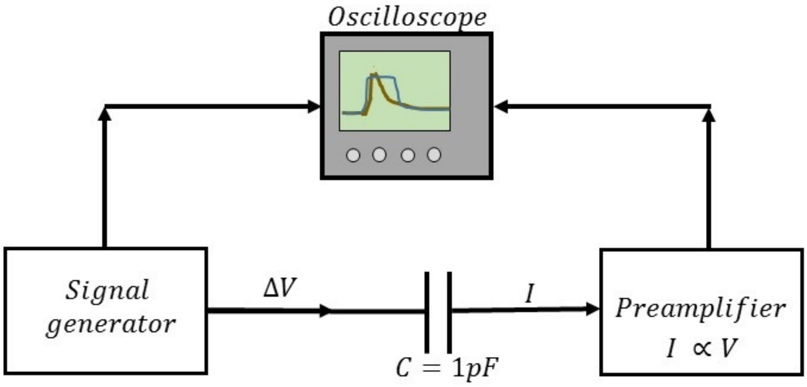

Figure 6.19: *Depiction of the system used to calibrate the PIN diode.*

This way, it is possible to relate the amount of electrons coming into the preamplifier and the amplitude of the outcoming variable difference of voltage:

$$\Delta V \cdot C = Q \tag{6.10}$$

$$Q \cdot 1.6 \times 10^{-19} \frac{Coulomb}{electron} = electrons \tag{6.11}$$

6.4.1 Computation of the amount of photons

Once the amount of electrons is figured out it is necessary to know the correspondence between generated electrons in the PIN diode and incoming photons. It is capital to know responsivity of the photosensor which represents the ratio electrical output/optical input [65].

$$R = \eta \frac{q}{h\nu} = \eta \frac{q\lambda}{hc} \tag{6.12}$$

The responsivity (R) depends on the temperature and is given in the data sheet of the device; η represents the quantum efficiency of the photosensor. It is the efficiency of the process of generation of photoelectrons and depends on the wavelength. It is also given by the manufacturer in the data sheet.

$$\eta PIN(T, \lambda) = \frac{R(T)hc}{q\lambda} \tag{6.13}$$

The last factor needed is the solid angle subtended by the PIN diode at a certain distance:

$$d\Omega_{PIN} = \frac{\vec{e_r} d\vec{S_{PIN}}}{d^2} = \frac{dS_{PIN} cos\theta}{d^2} \tag{6.14}$$

If the PIN diode is placed tangentially to the surface of the integrating sphere then $\theta = \frac{\pi}{2}$ and $cos\theta = 1$. This way the solid angle subtended by the PIN diode at a distance d in comparison to the solid angle of a sphere of $r = d$ is:

$$\frac{d\Omega_{PIN}}{\Omega} = \frac{S_{PIN}}{4\pi d^2} \tag{6.15}$$

Where 4π is the solid angle of a sphere measured from any point in its interior expressed in steradians. Once every factor is calculated, the total amount of photons emitted by the surface of the integrating sphere, assuming perfect isotropy, is:

$$\#\gamma = \frac{\#e^-}{\eta_{PIN} d\Omega_{PIN}} \tag{6.16}$$

6.5 Results

The resulting graphics are the product of the tests carried out in the laboratory. All the measurement effectuated to understand how to modulate the pulse produced by the flasher were made with a distance of 10 cm from the centre of the integrating sphere to the detector. The plots corresponding to the LEDs kinetics tests made by varying components of the flasher are expressed in arbitrary units for no previous calibration was executed.

6.5.1 Flash modulation

To study which factors exert more influence in the task of modulating the light output and how, the following test were made in consonance with the simulations carried out.

6.5.1.1 Pulse kinetic dependence on the bias voltage

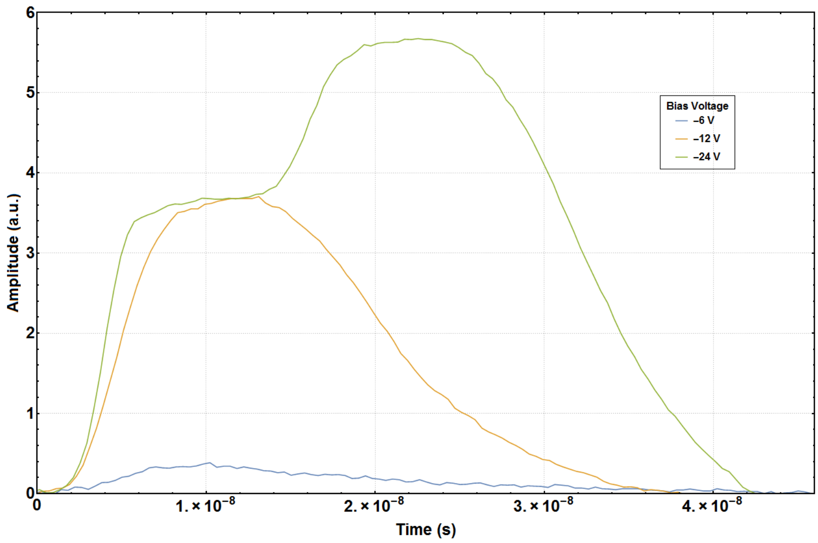

Figure 6.20: *Nichia NCSU276AT-U385,* $C_1 = 1\,nF, C_2 = 47\,pF.\ L_1 = \infty\,nH$ [66].

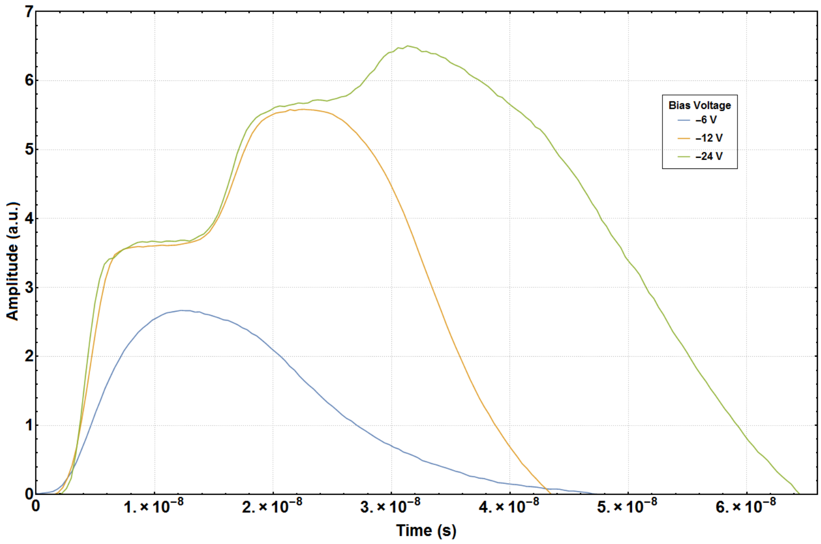

Figure 6.21: *TSLC SLLP-F586-1520-UV-405,* $C_1 = 1\,nF, C_2 = 47\,pF,\ L_1 = \infty\,nH$ [67].

The study of how the light pulse intensity changes by varying the negative bias voltage, shown in the plots above, confirms the simulations plotted in Fig. 6.2. It is shown how the width of the LED light pulse changes depending V_{cc}. Also the amplitude of the pulses is reduced as the diminution of V_{cc} makes it harder for the transistors to reach the the breakdown voltage. This causes the thyristor to shut off sooner and thus, the pulse does grow as big as when the different of potential is higher. The less charge is in play, the shorter the light pulse is. For this to be confirmed, long pulses needed to be produced so a 1 nF capacitor and no inductance was used. This results coincides with the results published by B.K. Lubsandorzhiev and Y.E. Vyatchin[47]. To measure the pulses the PIN diode PS33-6b-TO was used together with a non-integrating amplifier. The signal was stored and studied thanks to the software of the oscilloscope. For technical reasons, V_{cc} was decided to be set at -12 V during the construction of the first prototype of POCAM dropped in Lake Baikal, Siberia.

6.5.1.2 Pulse kinetic dependence on the charge provided by the main capacitor C_1

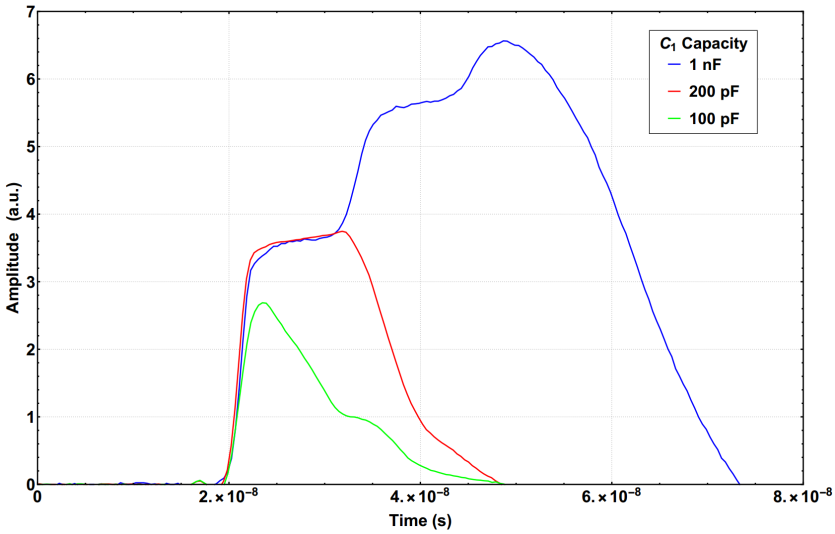

Figure 6.22: *Nichia NCSU276AT-U385,* $V_{cc} = -24\,V, C_2 = 47\,pF. L_1 = \infty\,nH.$

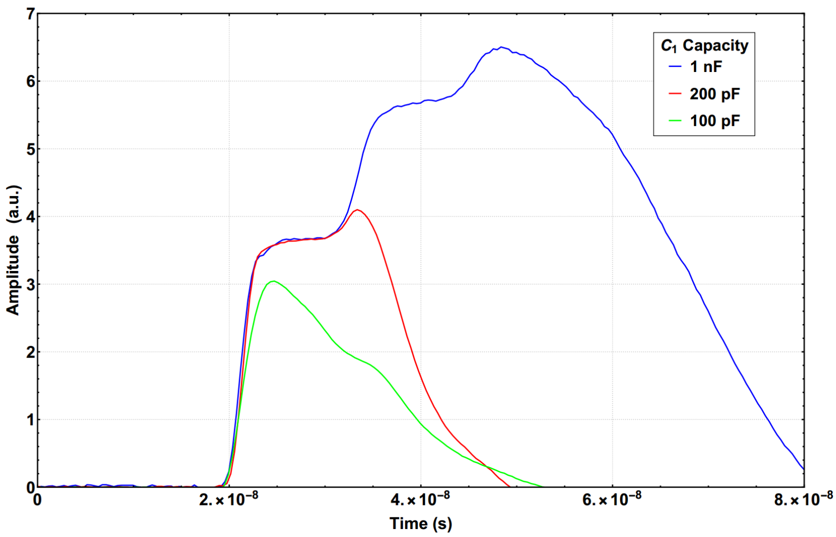

Figure 6.23: *TSLC SLLP-F586-1520-UV-405,* $V_{cc} = -24\,V, C_2 = 47\,pF. L_1 = \infty\,nH.$

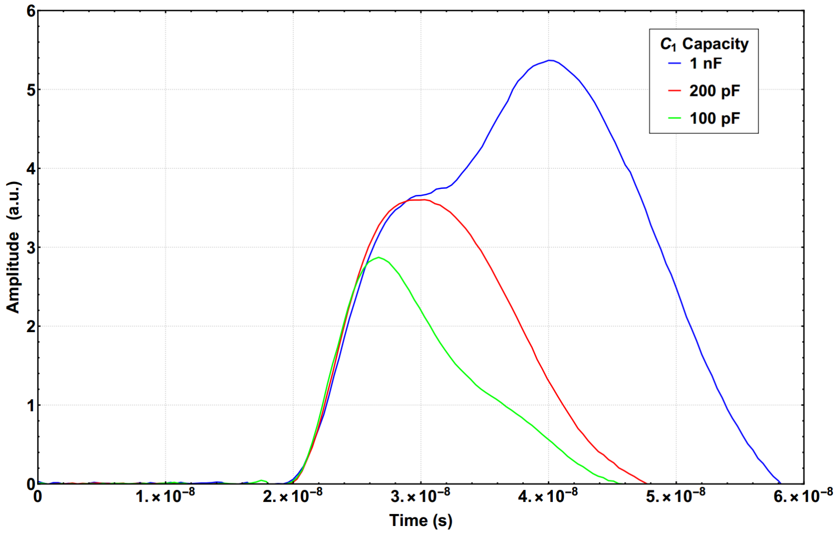

Figure 6.24: *Bivar UV5TZ-405,* $V_{cc} = -24\,V, C_2 = 47\,pF. L_1 = \infty\,nH$ [68].

As shown in previous sections and in the simulations, it can be seen in Fig. 6.22, Fig. 6.23, and Fig. 6.22, that the bigger the capacity of C_1 is, the more charge the LED can use and as a consequence, larger pulses are produced. To study the behaviour of the flasher as the capacity of C_1 is changed, long pulses are sought as it makes easier to spot variations in amplitude, rising time and duration. For this purpose no inductance was used as well as $V_{cc} = -24$ V. Increasing the charge available produces larger pulses. The larger the light pulse is, the higher the photon output. As a counterpart, a larger pulse also means a "slower" pulse as the FMHW and rising time increase faster than its amplitude.

6.5.1.3 Pulse kinetic dependence on the inductance L_1

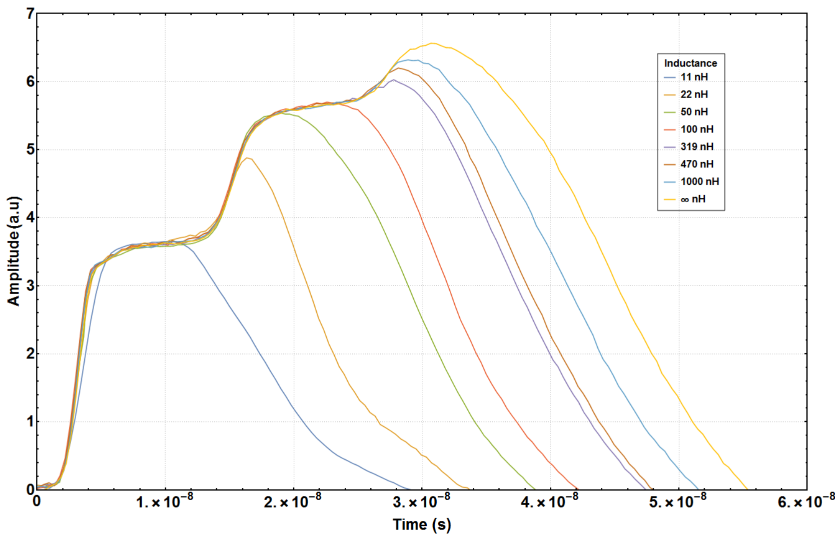

Figure 6.25: *Nichia NCSU276AT-U385,* $V_{cc} = -24\,V$, $C_1 = 1\,nF$, $C_2 = 47\,pF$..

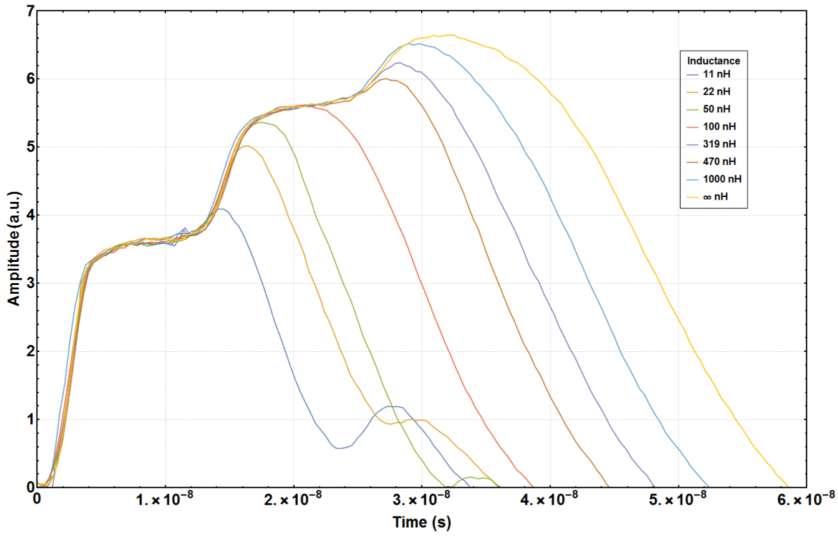

Figure 6.26: *TSLC SLLP-F586-1520-UV-405, $V_{cc} = -24\,V$, $C_1 = 1\,nF$, $C_2 = 47\,pF$..*

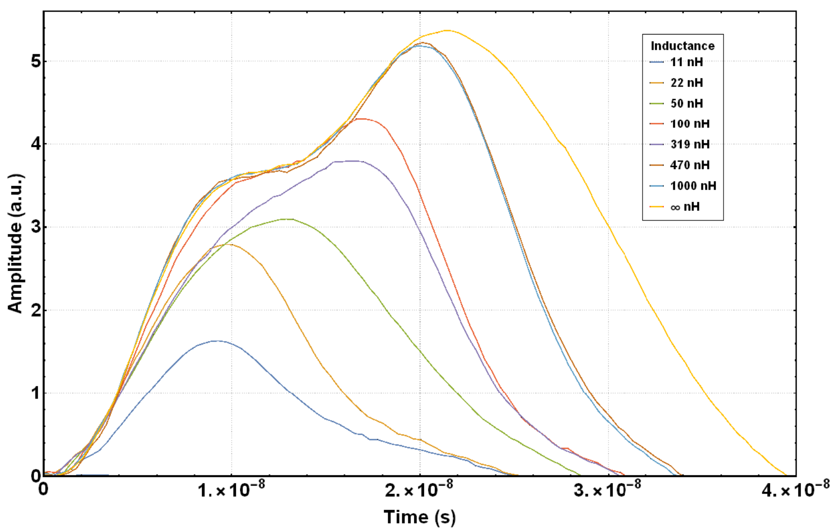

Figure 6.27: *Bivar UV5TZ-405, $V_{cc} = -24\,V$, $C_1 = 1\,nF$, $C_2 = 47\,pF$..*

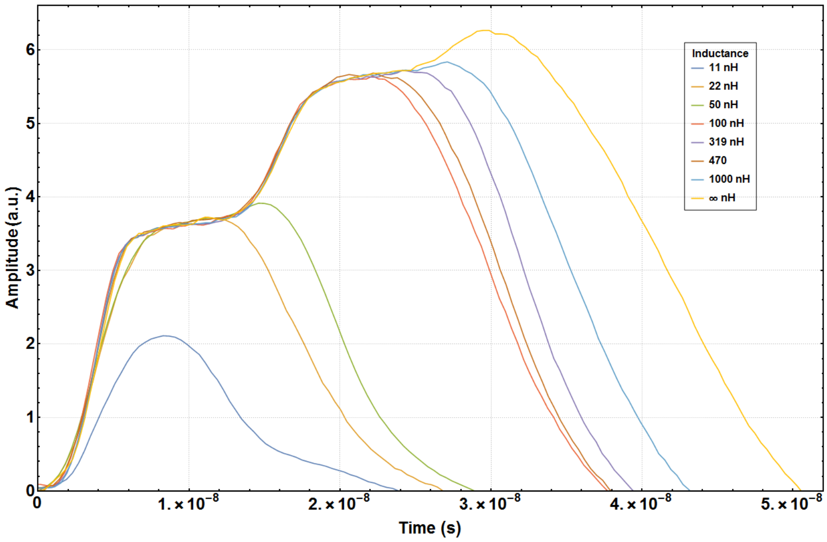

Figure 6.28: *ProLight-PM2I-400*, $V_{cc} = -24\,V$, $C_1 = 1\,nF$, $C_2 = 47\,pF$.[69].

As seen in the 3 plots from above, the inductance in parallel with the LED helps modulating the duration (FWHM) of the pulse. It opposes to the charge that C_1 provides shortening the tail of the light pulse. As it can be seen in the plots, the pulse grows proportionally with the value of the inductance until it reaches the maximum when no inductance is included in the tester PCB ($\infty\,nH$). The smaller the inductance is, the more charge opposes to the charge provided to the main capacitor C_1 and thus, the smaller the light pulse. The reference to compare pulses from the same LED was chosen to be PCB with C_1. This is so because for some LEDs (i.e. Prolight-PM2I-400), the tandem $C_1 - L_1$ couldn't generate enough charge to produce light pulses.

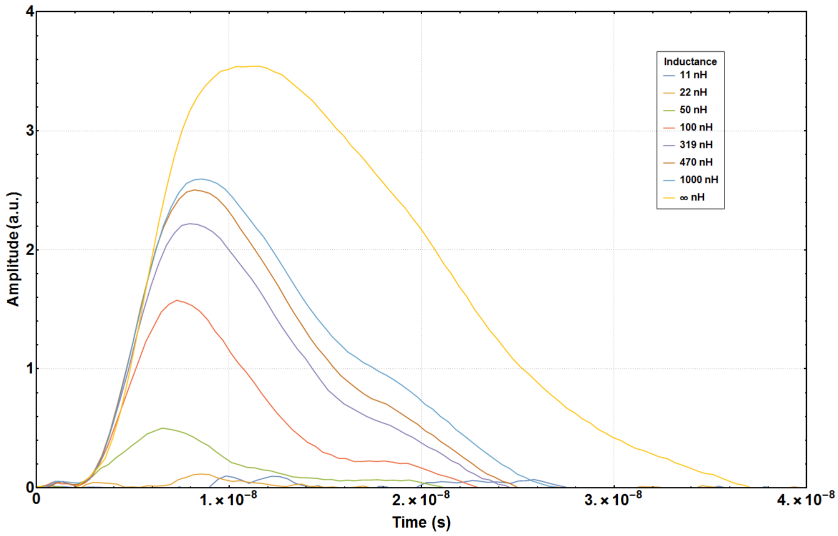

Figure 6.29: *ProLight-PM2I-400*, $V_{cc} = -24\,V$, $C_1 = 200\,pF$, $C_2 = 47\,pF$..

On the above plot the PCB with $C_1 = 200\,pF$ produces no flash for $L_1 = 22\,nH$ and

$L_1 = 11\,nH$. The opposition exerted by the inductance is way to high. This provokes the current through the thyristor to be insufficient and hence, the LED does not flash.

6.5.2 Flash modulation overview

The flasher PCB provides the possibility to change the duration of the light pulse in terms of rising time and FWHM and consequently, the photon output. Three factors are key for this task: the charge put in play by the main capacitor C_1, the opposition exerted by the inductance in parallel with the LED, L_1, and the negative bias voltage of the circuit V_{cc}. Independently of the LED (leaded or SMD), pulses become shorter for smaller values of V_{cc} and/or L_1.

- The variation of V_{cc} reduces significantly the amplitude and the FWHM. This supposes an important drop of the photon output. To understand why this happens it is important to have in mind the functioning of the thyristor part explained in Subsection 5.1.2. Lower values of $|V_{cc}|$ mean a smaller different of potential between the anode and the cathode of the thyristor. It makes it harder for the BJTs to reach the breakdown voltage and therefore, it is harder for the gate current to escalate over the latching current that triggers the fast growing of the charge through the two BJTs structure (thyristor).

- The inductance forms a parallel RLC circuit with the LED. In a real circuit, every element has a certain resistance, inductance and capacity. Due to the nature of the LED, it works as a small capacitor. The length of the paths connecting the elements of the PCB or if the components are leaded or SMD affect the impedance of the circuit and therefore, the pulse. As the value of L_1 grows, the oscillation frequency of the RLC resonating circuit decreases $\left(\omega = \frac{1}{\sqrt{LC}} \; or \; f = \frac{\omega}{2\pi} = \frac{1}{2\pi\sqrt{LC}}\right)$. This means that the charge transference between the inductance and the capacitor happens in a slower way allowing the pulse to grow bigger. For smaller values of L_1 the resonance frequency of the circuit is higher and thus, the transference of charge that ends up cutting off the conduction of current through the thyristor. This way shorter pulses are produced.

- The charge accumulated by C_1 flows through the thyristor building up the current that flashes the LED. If more charge is available, the gate current of the thyristor (I_G) will be larger and thus, the total current flowing through it Eq. 5.7. Also, if (I_G) grows, the difference of voltage between anode and cathode of the thyristor (V_{AK}) needs to be lower to allow the current to flow through it (see Fig. 5.3). A bigger growing electric pulse means more charge carriers in play to provoke the electrons to migrate from the conduction band to the valence band emitting photons in its way. In the case that there is sufficient charge flowing, the bottleneck factor could be the available surface of the PN-junction forming the LED that is capable of generating photons. A higher current means more charge per unit time so, with a "larger" LED, in terms of PN-junction effective surface, more photons can be emitted per unit time. This is the reason, together with the reduction of the impedance inherent to the elements of the PCB, why it was chosen to switch from leaded to some SMD LEDs.

6.5.3 LED selection for the first prototype of POCAM

Following the procedure explained in Sectionsec:PScalib, the photon output of several LEDs was measured. The first prototype of POCAM had to be dropped in lake Baikal to test its performance. For this reason, due to the optical characteristics of the mean in which the Gigatron Volume Detector finds itself, it was decided to use blue (~ 470 nm) and green (~ 530 nm) SMD LEDs. The reference values taken were those from the PIN Diode. The difference between the photon output provided by the PIN Diode and the SiPM are around a factor of 4. This is so due to the nature of the detectors, their sensibility and the calibration of the SiPM. A better calibration with a detailed dependence of the breakdown voltage with the temperature is carried out by Immacolata Carmen Rea and Felix Henningsen.
The resulting plots are the product of the study on seven different LEDs.

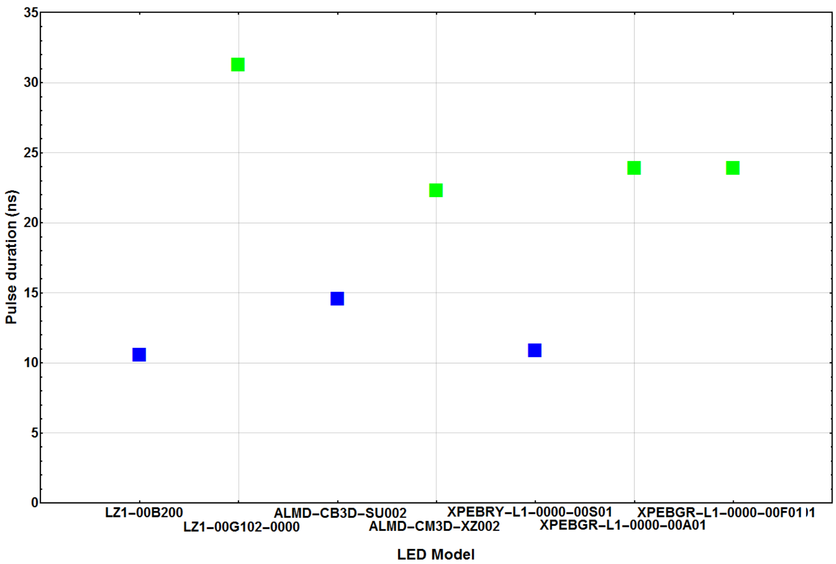

Figure 6.30: *Representation of the duration of long the pulses produced by the LEDs chosen for the first prototype of the POCAM (without error bars, measured with the SiPM).*

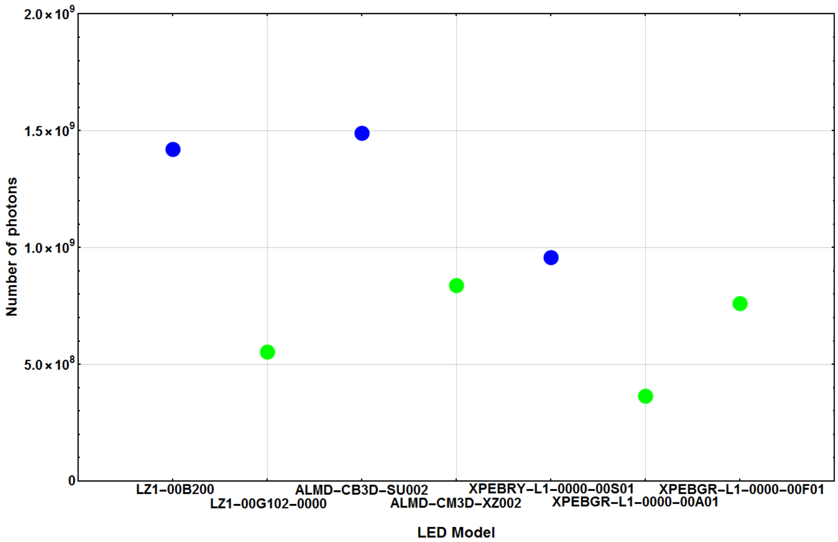

Figure 6.31: *Representation of the photon output produced by the LEDs chosen for the first prototype of the POCAM (without error bars, measured with the PIN diode).*

LED	Pulse duration (ns)	# Photons PIN Diode	# Photons Fluctuation
LZ1-00B200 [70]	10.5	$1.49 \cdot 10^9$	0.35 %
LZ1-00G102-0000 [71]	31.2	$5.53 \cdot 10^8$	0.31 %
ALMD-CB3D-SU002 [72]	14.5	$1.49 \cdot 10^9$	0.22 %
ALMD-CM3D-XZ002 [73]	22.2	$8.37 \cdot 10^8$	0.21 %
XPEBRY-L1-0000-00S01 [74]	10.8	$9.57 \cdot 10^8$	0.39 %
XPEBGR-L1-0000-00A01 [74]	23.8	$3.64 \cdot 10^8$	0.47 %
XPEBGR-L1-0000-00F01 [74]	23.8	$7.59 \cdot 10^8$	0.23 %

Table 6.3: *Duration of the long light pulses obtained with the SiPM and calculation of the correspondent photon output according to the data acquired with the PIN diode*

After considering the acquired data, the LEDs used for the first prototype of the POCAM in order to produce the long pulses were:

- **Blue LED:** LZ1-00B200 (λ_{typ} = 455 nm)
- **Green LED:** ALMD-CM3D-XZ002 (λ_{typ} = 525 nm)

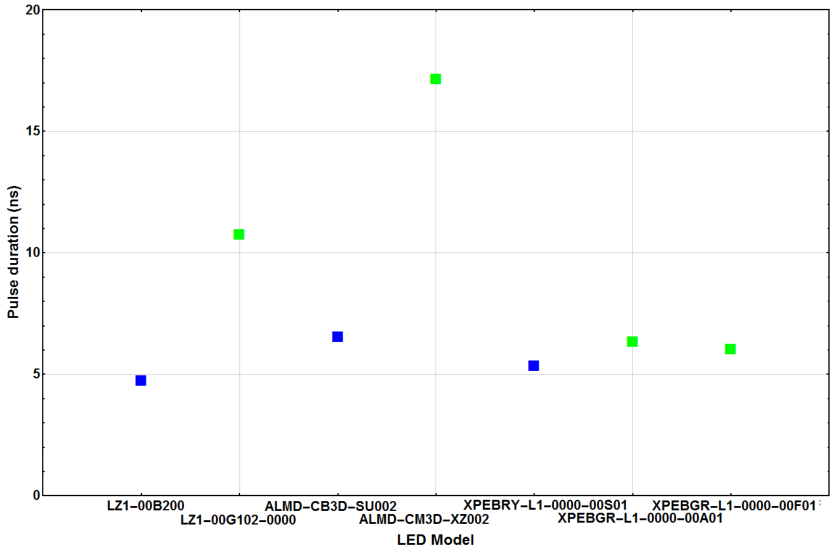

Figure 6.32: *Representation of the duration of the short pulses produced by the LEDs chosen for the first prototype of the POCAM (without error bars, measured with the SiPM).*

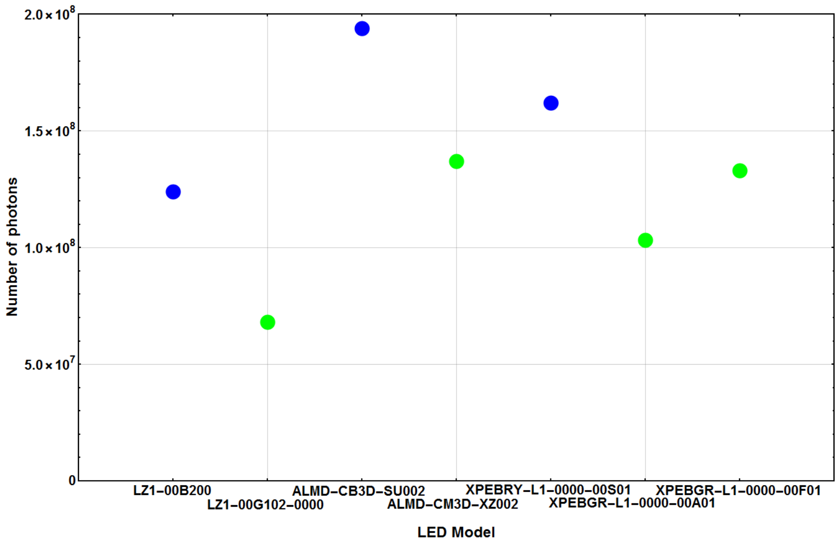

Figure 6.33: *Representation of the photon output produced by the LEDs chosen for the first prototype of the POCAM (without error bars, measured with the PD).*

LED	Pulse duration (ns)	# Photons PIN Diode	# Photons Fluctation
LZ1-00B200 (B) [70]	4.7	$1.24 \cdot 10^8$	2.00 %
LZ1-00G102-0000 (G) [71]	10.7	$6.81 \cdot 10^7$	3.80 %
ALMD-CB3D-SU002 (B) [72]	6.5	$1.94 \cdot 10^8$	1.69 %
ALMD-CM3D-XZ002 (B) [73]	17.1	$1.37 \cdot 10^8$	1.26 %
XPEBRY-L1-0000-00S01 (B) [74]	5.3	$1.62 \cdot 10^8$	2.31 %
XPEBGR-L1-0000-00A01 (G) [74]	6.3	$1.03 \cdot 10^8$	2.52 %
XPEBGR-L1-0000-00F01 (G) [74]	6.0	$1.33 \cdot 10^8$	1.95 %

Table 6.4: *Duration of the short light pulses obtained with the SiPM and calculation of the correspondent photon output according to the data acquired with the PIN diode*

After considering the acquired data, the LEDs used for the first prototype of the POCAM in order to produce the long pulses were:

- **Blue LED:** ALMD-CB3D-SU002 ($\lambda_{typ} = 470$ nm)
- **Green LED:** XPEBGR-L1-0000-00F01 ($\lambda_{typ} = 527$ nm)

Chapter 7

Conclusion

In this thesis the study of a flasher circuit for the POCAM is presented. The POCAM (Precision Optical CAlibration Module) is a part of the future low energy extension of the IceCube neutrino detector, IceCube-Gen2. The flasher is part of analogue PCB of the first prototype of the POCAM which has been deployed in lake Baikal in March 2017. It is a device able to emit light pulses of around 5 - 20 ns with a total output of $\mathcal{O}(10^8) - \mathcal{O}(10^9)\gamma$ per pulse covering a total surface of 4π sr in different wavelengths. The goal of the POCAM is to reduce the current systematic uncertainty of IceCube from 10% to a level of a few %.

When cosmic rays interact with our atmosphere they create particles that propagate through it. This is called Air Showers and among all the particles created, neutrinos are comprised. Neutrinos can travel through the earth almost without interacting due to their small cross-section. Nevertheless, the abundance of electrons in the Earth affects the neutrino oscillation. This neutrinos can interact via CC or NC with the ice of the South Pole generating the Cherenkov radiation that IceCube's DOMs detect. Based on the pattern recorded by the detectors, the flavour of the original neutrino as well as its track through the ice can be reconstructed. It is of capital importance to have a good calibration. In IceCube the calibration of the geometry of the detectors, the timing and energy scale is performed thanks to the LED included in the DOMs, the calibration lasers and the low energy muons tomography.
The energy threshold of IceCube is 100 GeV and the goal for PINGU is to lower it to a few GeV. The IceCube-Gen2 in which the PINGU extension is integrated aims to improve the study of the unitary matrix by performing more precise detections of ν_τ. For this task, a better reconstruction of the high energy shower events is necessary. The isotropic light emission pattern of POCAM will enhance the geometry calibration and will help verifying the energy scale and the energy resolution.

The POCAM can be divided in three sub-systems, a pressure housing, the digital and the analogue circuit boards and the light diffuser elements. The external part is composed by two glass hemispheres that are connected to a cylindrical housing made out of titanium in order to resist pressure and temperature changes. A Kapustinsky-like circuit drives a multi-wavelength array of LEDs that is able to generate light pulses of $\sim\ 10\,ns$ and $\mathcal{O}(10^8)\ -\ \mathcal{O}(10^9)\gamma$. A PTFE sphere in each hemisphere is responsible for the diffusion of the light pulses so as to produce isotropic, homogeneous illumination of the ice. It aims for the light every hemisphere to reach and isotropy of within 2% and the total light output to be determined within a 2% thanks to the built-in photosensors.
Although the POCAM was originally thought as a calibration instrument in the framework of IceCube-Gen2, its isotropic light emission pattern can help improving the measurements made with the LEDs that the DOMs are equipped with. It can be used to study the optical impact of refrozen drill holes on DOM sensitivity, the relative detection efficiency of each individual DOM, the reconstructed high energy cascade scale or the anisotropic scattering strength of the bulk ice.
This thesis contributes to the developing of the POCAM with the study of a simple flasher circuit that J.L.Kapustinsky purposed in 1985. The evolution of its study as well as the characteristics and emission profile of the LEDs through simulations with ORCAD PSpice and laboratory work. The pulser is based on the fast discharge that a capacitor can make via a set of two RF transistors forming a thyristor-like element. The voltage variation produced by the rising edge of a positive square pulse charges a small capacitor. This produces the fast voltage shock that turns the transistors “on” allowing the current to flow. When the breakdown voltage of the thyristor-like element is reached, the available charge for the LED increases very rapidly creating a pulse that flashes it. The LED has an inductor in parallel forming an LC-circuit, it develops charge opposing himself to the discharging capacitor and thus, reducing the decay constant of the light pulse.
The study of the modulation of the pulse generated by the flasher was performed by varying the bias voltage applied, the available charge provided by the main capacitor of the circuit and the value of the inductor in parallel with the LED. Due to the necessities and characteristics of the POCAM and its first prototype test in lake Baikal, the PIN diode S5972 photodiode from Hamamatsu was substituted for the PS33-6b-TO from First Sensor, which has a bigger sensitive surface. A second photosensor is also included, a SiPM (PM3325-EB) from KETEK, from which a better calibration is being carried out by the group. The response of a total of 11 LEDs was studied.
The simulations performed to learn about the behaviour of the flasher coincide with the experience extracted from the laboratory. The light output produced by the Kapustinsky shows the same response independently of the LED. The pulses grow in terms of rising

time, amplitude and duration as the absolute value of the negative bias voltage is increased. Furthermore, the bigger the main capacitor is, the more charge is available and bigger light pulses are produced. The effect on the tail (falling part) of the light pulses shows a proportional relation with the value of the inductance: higher inductance values allow the pulse to grow for a longer time and thus, the photon output is also higher. Thanks to this, it has been learnt that there are three easy ways to modulate the pulses produced by the Kapustinsky flasher: variate the negative bias voltage, the main capacitor or the inductance.

The light emitting component of the POCAM is composed by four independent, reduced-size Kapustinski drivers with two different pulse configuration ($\sim$5 ns - $\sim$20 ns) and two colors (blue 455-470 nm and green 527-527 nm). Two additional LEDs are also installed in the analogue PCB in which the flashers are included. This two additional LEDs are controlled by a FPGA and can produce longer pulses (20-80 ns) with higher photon output.

A collaboration with the Gigatron Volume Detector (GVD) in lake Baikal was established to verify the performance of the POCAM under real conditions. The materialization of this collaboration took place in March 2017 when the first prototype of the POCAM was shipped to Siberia for its integration on one of the outer rings at a depth of 1100 m. At the beginning of May, the GVD dedicated its time to measure the flashes produced by the POCAM. The analysis of the data gathered is on-going and will be reported.

Bibliography

[1] T. Abu-Zayyadaf R. Abbasiz, Y. Abdout. Calibration and characterization of the icecube photomultiplier tube. *Nucl.Instrum.Meth.A618:139-152,2010*, 11.Feb.2010. arXiv:1002.2442v1 [astro-ph.IM].

[2] C. L. Cowan, F. Reines, F. B. Harrison, H. W. Kruse, and A. D. McGuire. Detection of the Free Neutrino: a Confirmation. *Science*, 124(3212):103–104, jul 1956.

[3] Wikipedia Website: Standard Model. https://en.wikipedia.org/wiki/Standard_Model. Accessed: 2017-06-25.

[4] Ivan V. Anicin. The Neutrino - its Past, Present and Future.

[5] E. Peinado and A. Vicente. Neutrino masses fromR-parity violation with aZ3symmetry. *Physical Review D*, 86(9), nov 2012. arXiv:1207.6641v2 [hep-ph].

[6] L. Grodzins M. Goldhaber and A. W. Sunyar. Helicity of neutrinos. *Physical Review. 109, 1015*, 1958.

[7] C. Giunti and C. W. Kim. *Fundamentals of Neutrino Physics and Astrophysics*. OUP Oxford, 2007.

[8] et al. Q.R. Ahmad, R.C. Allen. Measurement of the rate of ν_e + d $\rightarrow$ p + p + e^- interactions produced by ^{8}B solar neutrinos at the Sudbury Neutrino Observatory. *Phys.Rev.Lett.87:071301*, 2001. arXiv:nucl-ex/0106015v2.

[9] M. De Serio. Observation of $\nu_\mu \rightarrow \nu_\tau$ oscillations in the CNGS beam with the OPERA experiment. *EPJ Web of Conferences*, 95:03005, 2015.

[10] Célio A. Moura and Marcelo M. Guzzo. New analyses of double-bang events in the atmosphere. *Braz. J. Phys. 38, 219-226 (2008)*, 10 Jun 2010. arXiv:hep-ph/0703145v3.

[11] P. Cherenkov. Visible Radiation Produced by Electrons Moving in a Medium with Velocities Exceeding that of Light. *Physical Review 52, 378*, 1973.

[12] F. Cappella-R. Cerulli. R. Bernabei, P. Belli. New results from dama/libra. *Eur. Phys. J. C*, (67):39–49, 2010. arXiv:1002.1028v1 [astro-ph.GA].

[13] Icecube Website: Beyond Icecube. http://icecube.wisc.edu/science/beyond. Accessed: 2017-07-15.

[14] T. Abu-Zayyad-M. Ackermann R.Abbasi, Y. Abdou. The Design and Performance of IceCube DeepCore. *Astroparticle Physics*, 35(10):615–624, May 2012. arXiv:1109.6096v1 [astro-ph.IM].

[15] The IceCube-PINGU Collaboration. Letter of intent: The precision icecube next generation upgrade (pingu). *Instrumentation and Detectors*, 9 Jan 2014. arXiv:1401.2046 [physics.ins-det].

[16] IceCube-Gen2 Collaboration: M. G. Aartsen and M. Ackermann et al. IceCube-Gen2: A Vision for the Future of Neutrino Astronomy in Antarctica.

[17] IceCube Webseite: In Science: Evidence for High-Energy Extraterrestrial Neutrinos at the iceCube Detector. https://icecube.wisc.edu/gallery/press/view/1505, 2013. Accessed: 2017-06-30.

[18] J. Adams M. G. Aartsen, M. Ackermann. The icecube neutrino observatory: Instrumentation and online systems. *JINST 12 P03012 (2017)*, 22. March.2017. arXiv:1612.05093v2 [astro-ph.IM].

[19] K.A. Olive. Review of Particle Physics. *Chinese Physics C*, 38(9):090001, aug 2014.

[20] T. Waldenmaier. Icetop - Cosmic Ray Physics with IceCube. *Nucl. Instrum. Meth. A588*, pages 130–134, 2008. arXiv:0802.2540v1 [astro-ph].

[21] Wikipedia Website: Ice Cube Neutrino Observator. https://en.wikipedia.org/wiki/IceCube_Neutrino_Observatory. Accessed: 2017-06-03.

[22] J. Adams . R. Abbasi, M. Ackermann. The IceCube Data Acquisition System: Signal Capture, Digitization, and Timestamping. *Nucl.Instrum.Meth.A601:294-316,2009*, 2009. arXiv:0810.4930v2 [physics.ins-det].

[23] Y. Abdou M. Ackermann. M. G. Aartsen, R. Abbasi. Measurement of south pole ice transparency with the IceCube LED calibration system. *Nuclear Instruments*

and Methods in Physics Research Section A: Accelerators, Spectrometers, Detectors and Associated Equipment, vol. 711, pp. 7389, May 2013. arXiv:1301.5361v1 [astro-ph.IM].

[24] P. Hallen. On the Measurement of High-Energy Tau Neutrinos with IceCube. Master's thesis, Rheinisch-Westfälischen Technischen Hochschule Aachen, 2013.

[25] M. Ackermann M. G. Aartsen, K. Abraham. Search for Astrophysical Tau Neutrinos in Three Years of IceCube Data. *Phys. Rev. D 93, 022001*, 2016. arXiv:1509.06212v2 [astro-ph.HE].

[26] M. Ackermann M. G. Aartsen, R. Abbasi. Energy reconstruction methods in the icecube neutrino telescope. *JINST 9 (2014), P03009*, 10 Feb 2014. arXiv:1311.4767v3 [physics.ins-det].

[27] Andreas Mackensen Werner U.Ehrmann. Sedimentological evidence for the formation of an East Antarctic ice sheet in Eocene-Oligocene time. *Palaeogeography, Palaeoclimatology, Palaeoecology*, 93(1-2):85–112, May 1992.

[28] X. Bai M. Bartelt. M. Ackermann, J. Ahrens. Optical properties of deep glacial ice at the south pole. *J. Geophys. Res., 111, D13203*, 2006. http://onlinelibrary.wiley.com/doi/10.1029/2005JD006687/abstract.

[29] SPICE3 ice model presentation. https://docushare.icecube.wisc.edu/dsweb/Get/Document-69693/ice.ppt. Accessed: 2017-08-10.

[30] Icecube Wiki: IceCube ice models. https://wiki.icecube.wisc.edu/index.php/Ice_models. Accessed: 2017-08-10.

[31] J. Adams A. Achterberg, M. Ackermann. First year performance of the icecube neutrino telescope. *Astropart.Phys.26:155-173,2006*, 25 Apr 2006. arXiv:astro-ph/0604450v2.

[32] Icecube wiki: Geometry calibration. https://wiki.icecube.wisc.edu/index.php/Geometry_calibration. Accessed: 2017-07-04.

[33] Icecube wiki: Ice shear measurement. https://wiki.icecube.wisc.edu/index.php/Ice_shear_measurement. Accessed: 2017-07-03.

[34] S. Coenders. Capability of Earth Tomography Using Oscillations of Atmospheric Neutrinos with PINGU. Master's thesis, Rheinisch-Westfälischen Technischen Hochschule Aachen, 2013.

[35] Kai Michael Krings. Studies on the Measurement of Atmospheric Neutrino Oscillations with the PINGU detector. Master's thesis, Rheinisch-Westfälischen Technischen Hochschule Aachen, September 2013.

[36] K. Krings. A precision optical calibration module for icecube-gen2. *PoS, vol. ICRC2015*, 2015. https://pos.sissa.it/236/1133.

[37] K. Holzapfel K. Krings E. Resconi M. Jurkovic, K. Abraham and J. Veenkamp. A Precision Optical Calibration Module (POCAM) for IceCube-Gen2. In *EPJ Web Conf., vol. 116, p. 06001*, 2016.

[38] N.J.DiGiacomo W.E.Sondheim J.W.Sunier H.Coombes J.S.Kapustinsky, R.M.DeVries. A fast timing light pulser for scintillation detectors. *Nuclear Instruments and Methods in Physics Research Section A: Accelerators, Spectrometers, Detectors and Associated Equipment, Volume 241, Issues 23, Pages 612-613*, 1 Dec 1985.
http://www.sciencedirect.com/science/article/pii/0168900285906229.

[39] et al J.Ahrens. *IceCube Preliminary Design Document*, October 2011.

[40] Nautilus Marine Service GmbH: Datasheet of the BK-7 glass and the Borosilicate glass.

[41] Thorlabs: UV Fused Silica (Quartz) High Precision Windows Datasheet. https://www.thorlabs.de/newgrouppage9.cfm?objectgroup_id=3983. Accessed: 2017-07-19.

[42] Felix Henningsen. Bachelor arbeit: Realisierung des precision optical calibration module-prototyps zur kalibrierung von icecube-gen2. Technische Universität München, 2016.

[43] Joost Veenkamp. A Precision Optical Calibration Module for IceCube-Gen2. Master's thesis, Technische Universität München, 2016.

[44] D. Chirkin. Evidence of optical anisotropy of the South Pole ice. In *Proceedings, 33rd International Cosmic Ray Conference (ICRC2013)*, 2013.

[45] Martin Rongen et al M. G. Aartsen. Measuring the optical properties of IceCube drill holes. In *EPJ Web of Conferences 116, 06011*, 2016.

[46] J. Adams M. G. Aartsen, M. Ackermann. Determining neutrino oscillation parameters from atmospheric muon neutrino disappearance with three years of IceCube DeepCore data. *Phys. Rev. D 91, 072004*, 13 Apr 2015. arXiv:1410.7227v2 [hep-ex].

[47] Y.E.Vyatchin B.K.Lubsandorzhiev. Studies of "Kapustinsky's" light pulser timing characteristics. *JINST 1 (2006) T06001*, 20 June, 2006. arXiv:physics/0410281v1 [physics.ins-det].

[48] B.A. Borisovetsa N.M. Budne. I.A. Belolaptikov, L.B. Bezrukova. The Baikal underwater neutrino telescope: Design, performance, and first results. *Astroparticle Physics*, 7(3):263–282, August 1997.

[49] B. A. J. Shaibonov Y. E. Vyatchin A. Z. Zablotsky B. K. Lubsandorzhiev, R. V. Poleshuk. A LED Flasher for TUNKA experiment. In *Proceedings of the 30th ICRC*, 2007.

[50] A. Albert M. Ageron, J.A. Aguilar. The ANTARES Optical Beacon System. *Nucl.Instrum.Meth.A578:498-509*, pages 498–509, 2007. arXiv:astro-ph/0703355v1.

[51] Thyristor Theory and Design Considerations; ON Semiconductor; 240 pages; 2006; hbd855d.
http://www.rsp-italy.it/Electronics/Databooks/Semicond/_contents/Motorola
Accesed: 2017-07-31.

[52] Paul Horowitz Thomas C. Hayes. *The art of electronics*. Cambridge University Press, 22nd printing 2010.

[53] Wikipedia Website: Thyristor. https://en.wikipedia.org/wiki/Thyristor. Accessed: 2017-08-01.

[54] Wikipedia Website: Light Emitting Diode.
https://en.wikipedia.org/wiki/Light-emitting_diode. Accessed: 2017-07-20.

[55] Datasheet of PM33 from KETEK.
https://4b0vz81vun5u2kaw7x3w6ptl-wpengine.netdna-ssl.com/wp-content/uploads/2017/01/KETEK-PM3325-EB-PM3350-EB-Datasheet.pdf.

[56] Datasheet of PIN diode PS33-6b-TO from First Sensor.
http://www.mouser.com/ds/2/313/PS33-6b_TO_501244-586514.pdf.

[57] Website: SiPM Technology Ketek. https://www.ketek.net/sipm/technology/. Accessed: 2017-08-16.

[58] Doherty, Bill, MicroNotes PIN Diode Fundamentals, Watertown, MA Microsemi Corp., MicroNote Series 701. https://www.microsemi.com/document-portal/doc_view/134814-micronote-701-pin-diode-fundamentals. Accesed: 2017-07-26.

[59] Wikipedia Website: Miller Effect. https://en.wikipedia.org/wiki/Miller_effect. Accessed: 2017-08-17.

[60] Datasheet of CR-110 from CREMAT. http://www.cremat.com/CR-113.pdf.

[61] Datasheet of CR-113 from CREMAT. http://www.cremat.com/CR-113.pdf.

[62] Wikipedia Website: 555 IC Timer. https://en.wikipedia.org/wiki/555_timer_IC. Accessed: 2017-08-01.

[63] Charles K. Christiansen, Donald; Alexander. *Standard Handbook of Electrical Engineering (5th ed.).* McGraw-Hill, ISBN 0-07-138421-9, 2005.

[64] Wikipedia Website: Schmitt Triger. https://en.wikipedia.org/wiki/Schmitt_trigger. Accessed: 2017-08-01.

[65] Wikipedia Website: Responsivity. https://en.wikipedia.org/wiki/Responsivity. Accessed: 2017-08-20.

[66] Datasheet of nichia NCSU276AT-U385. https://www.nichia.co.jp/specification/products/led/NCSU276A-E.pdf.

[67] Datasheet of TSLC SLLP-F586-1520-UV. http://docs-europe.electrocomponents.com/webdocs/145d/0900766b8145d12d.pdf.

[68] Datasheet of Bivar UV5TZ-405-15. https://www.bivar.com/portals/0/products/UV5TZ-XXX-XX.pdf.

[69] Datasheet of ProLight-PM2L-3LLE-SD. http://www.prolightopto.com/upload/DS-0035_3W_PM2L-3LLx-SD_v1.9.pdf.

[70] Datasheet of lz1-00b200. http://www.ledengin.com/files/products/LZ1/LZ1-00B200.pdf.

[71] Datasheet of LZ1-00G102-0000. http://www.ledengin.com/files/products/LZ1/LZ1-00G102.pdf.

[72] Datasheet of ALMD-CB3D-SU002. https://docs.broadcom.com/docs/AV02-2372EN.

[73] Datasheet of ALMD-CM3D-XZ002. http://www.mouser.com/ds/2/678/V02-2372EN_DS_ALMD-Ex3D_Cx3D_2016-04-15-909271.pdf.

[74] Datasheet of XPEBRY-L1-0000-00*01. http://www.mouser.com/ds/2/90/XLampXPE2-253473.pdf.

Acknowledgements

I would like to thank Elisa Resconi for giving me the opportunity to work in her group. It has been a really enjoyable experience to be part of such a well communicated, functioning and multicultural group. Moreover, I also want to thank the chance I had to visit different places of Germany in order to present our work and collaborate with other students like Martin Rongen from the University of Aachen.
I am obliged to Roman Gernhäuser, Michael Böhmer and Laszlo Papp for the help and supervision provided during the progress of my thesis.
I can't forget mentioning the members of the laboratory group, Immacolata Carmen Rea, Felix Henningsen, Andreas Gärtner, Kilian Holzapfel, Christian Spannfellner, Lukas Krempel and Irene Mayoral Soriano. Without the uncountable hours of work the common goal of the POCAM wouldnt have been reached.
Last but not least I would like to thank my father Antonio Becerra Guzmán, my mother María Francisca Esteban Pérez and my sister Inmaculada Becerra Esteban for supporting me in my wish to learn how everything works. I can not forget all the friends I made in Munich since my Erasmus started five years ago, for building up our abroad-family, providing coffee breaks and unending hours of political discussions from different points of view.